EXCURSION 7A:
From silicic calderas to mantle nodules: Cretaceous to Quaternary volcanism, southern Basin and Range province, Arizona and New Mexico

Compiled by John S. Pallister

U.S. Geological Survey, Denver, Colorado 80225

Geologic framework of the southern Basin and Range

David A. Sawyer and John S. Pallister

U.S. Geological Survey, Denver, Colorado 80225

Introduction

Mesozoic to Quaternary volcanism in southern Arizona and New Mexico is closely related to the structural and tectonic evolution of the Basin and Range province. Although the volcanic centers described in this guidebook are compositionally and temporally diverse, they share a common basement framework. This overview attempts to establish a broad tectonic perspective from which to consider volcanism in the southern Basin and Range, and to point out similarities in eruptive processes at several volcanic centers.

Arizona and western New Mexico are divided into two main physiographic and crustal-structure provinces, the Colorado Plateau and the Basin and Range (Fig. 1). The eastern boundary of these provinces is the Rio Grande rift, beyond which lies the North American craton, undeformed by late Cenozoic tectonism and largely unaffected since late Paleozoic/early Mesozoic orogeny. The Rio Grande rift merges

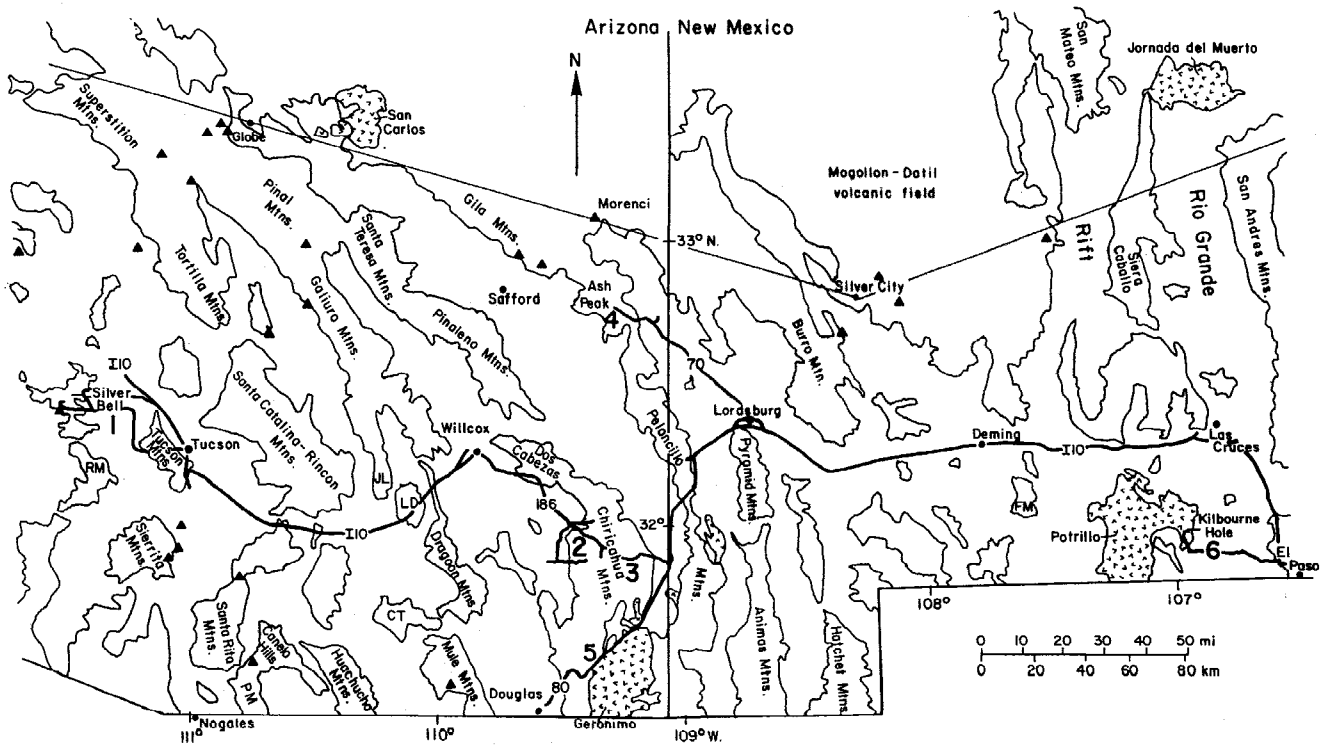

FIGURE 1—Sketch map showing field-trip localities and prominent geographic features in southern Arizona and New Mexico. Major Pliocene–Quaternary volcanic fields are shaded; triangles show the locations of major porphyry copper deposits in the southern Basin and Range. Approximate trace of crustal cross section of Fig. 2 is shown by line from Globe through Morenci to Silver City, then bending northeast through the San Andres Mountains. Actual line of cross section in Fig. 2 extends much farther west across Arizona to the Colorado River. Mountain-range abbreviations: RM = Roskruge Mountains, PM = Patagonia Mountains, JL = Johnny Lyons Hills, LD = Little Dragoon Mountains, CT = Charleston–Tombstone caldera area, FM = Florida Mountains.

with the Basin and Range in southern New Mexico and extends southeast into west Texas and Chihuahua, Mexico (Seager and Morgan, 1979; Olsen et al., 1987). The southern Basin and Range is characterized by rugged mountain ranges that rise abruptly from broad alluvial valleys. This topography is mainly the result of late Tertiary and Quaternary tectonics, and is simply the last layer of geologic complexity in a region that has experienced numerous episodes of magmatism and orogeny since the Proterozoic.

This field guide takes one through magmatic systems of progressively younger ages, which represent magmatic processes that took place at varying depths in the crust and mantle. The Silver Bell and Tucson Mountains expose eroded caldera-fill sequences and ring-dike intrusions of Late Cretaceous age. Mid-Tertiary calderas and rhyolite vent complexes of the Chiricahua and Peloncillo Mountains are exposed at levels that range from the juvenile volcanic surface to eroded surfaces within comagmatic shallow crustal magma reservoirs. Finally, the late Tertiary to Quaternary Geronimo and Potrillo basalt fields provide insight into both surficial volcanology and lower crustal and mantle magmatic and metamorphic events.

Plate-tectonic framework

The southern Basin and Range is composed primarily of rocks produced during multiple episodes of tectonism and magmatism related to plate-boundary interactions to the south and west (Dickinson, 1981; Engebretson et al., 1984, 1985). Middle Proterozoic rocks southwest of the Archean Wyoming craton are thought to represent intraoceanic island arcs and marginal basins accreted to the North American continental margin between about 1.8 and 1.6 Ga (Condie, 1982). A northeast-trending boundary, between compositionally distinct 1.8–1.7 Ga rocks to the northwest and 1.7–1.6 Ga rocks to the southeast, passes through central Arizona, roughly between Phoenix and Prescott. This boundary is a diffuse zone with significant overlap in age of post- and syn-orogenic plutonism (Karlstrom et al., 1987). A marked contrast between strongly deformed island-arc volcanic rocks and batholiths to the northwest (Anderson and Silver, 1976) and less deformed supracrustal silicic volcanics, sedimentary rocks, and coeval batholiths to the southeast (Conway and Wrucke, 1986) may require juxtaposition of these terranes by accretion after 1.69 Ga (Karlstrom et al., 1987). The oldest exposed crust in southeast Arizona is composed principally of quartz–muscovite schist, the Pinal Schist, that appears to have formed in deep-water turbidite basins (Silver, 1978). Recent work has suggested deposition of the Pinal protoliths either near a north-dipping subduction zone (Swift, 1987), or in an extensional (rift) setting (Condie et al., 1985).

These 1.8–1.6 Ga metamorphic and associated syn- and post-deformation plutonic rocks were regionally intruded by anorogenic granite plutons between 1.44 and 1.42 Ga (Anderson, 1983). These coarse, K-feldspar megacrystic biotite granites are the dominant Precambrian rocks in many ranges in the southern Basin and Range. Depositionally overlying these plutons are undeformed, weakly metamorphosed, sedimentary rocks of the Apache Group (Shride, 1967). These sedimentary rocks are cut by diabase intrusive sheets and dikes dated at 1.11–1.12 Ga (Silver, 1978); deposition of sediments and intrusion of diabase probably occurred during a rifting event (Davis et al., 1981). Proterozoic supracrustal rocks in the Franklin and Carrizo Mountains of west Texas were deposited(?) and intruded by alkalic granite at about the same time (Condie, 1981). Cambro-Ordovician alkalic magmatism has recently been documented by U–Pb ages on an alkali-granite pluton in the Florida Mountains, southwest New Mexico (Evans and Clemons, 1988); other undated alkali-granite plutons assumed to be 1.4 Ga may also be of this age.

Latest Precambrian–Paleozoic tectonics were initially typical of a stable craton, but middle Paleozoic tectonism along the transcontinental arch generated minor variation in sedimentary facies, and late Paleozoic basins were activated by the collisional effects of the Ouachita orogeny to the southeast (Kluth, 1986; Stewart, 1988; Armin, 1987). The Paleozoic history of southern Arizona is dominated by the accumulation of a 1–2 km thick section of platform sedimentary rocks (mostly carbonates). The southern passive margin of the Paleozoic North American continent was just south of the U.S.–Mexico border; off-shelf deep-water eugeoclinal sediments were deposited during early and middle Paleozoic time approximately 200 km to the southwest in Sonora (Stewart, 1988). No igneous activity is recorded in this fairly complete Paleozoic depositional record.

Phanerozoic continental-arc magmatism in the southern Basin and Range is first recorded by Jurassic volcanic rocks and caldera fragments. These, and subsequent periods of arc magmatism, can be related to subduction/accretion events in the Cordillera to the west. The earliest episode ranged from 210 to 185 Ma in western and southern Arizona. The latest Jurassic magmatic rocks (165–145 Ma) overlap in age with the Nevadan orogeny (150–160 Ma; Schweickert et al., 1984), a period when metamorphosed middle Paleozoic to Jurassic oceanic and island-arc assemblages were accreted to the continental margin in the western foothills belt of the Sierra Nevada.

Cordilleran thrust faulting affected much of the southern Basin and Range in Arizona and New Mexico from about 90 to 75 Ma, coincident with the Sevier orogeny in Utah, Wyoming, and Idaho. Calc-alkaline arc magmatism migrated eastward from the continental margin in California, in both the Sierra Nevada (Chen and Moore, 1982) and the Peninsular Ranges (Silver, unpubl. data; summarized in Keith and Wilt, 1986), and into Arizona by 75 Ma. From 75 Ma to approximately 60 Ma (actual crystallization ages are poorly known due to resetting of K–Ar ages), widespread calc-alkaline magmatism in southern Arizona and New Mexico constituted a major continental interior arc province (Lipman and Sawyer, 1985). Plutonism related to this volcanic episode is responsible for the majority of the porphyry copper deposits in southwestern North America (Titley, 1982), one of the two largest porphyry copper-producing provinces in the world. This outbreak of magmatism has been related primarily to a sharp increase in plate-convergence rates between 75 to 50 Ma (Engebretson et al., 1984). The eastward migration of magmatism has been linked to flattening of the subducted plate (Coney and Reynolds, 1977), although the origin of continental-interior magmas in the late Cretaceous and Tertiary remains controversial (Lipman, 1980; Wernicke et al., 1987; Larson et al., 1987).

Middle Tertiary volcanism in the Basin and Range took place during a period of transition from convergent margin continental-interior arc magmatism to extensional continental tectonics, the tectonic setting that dominated the remainder of the Tertiary. This change in tectonic regime is generally considered to have resulted from the collision of

the East Pacific Rise with the North American plate at about 28 Ma (Atwater, 1970). The collision resulted in a subsequent change from calc-alkaline andesite–rhyolite magmatism to bimodal basalt–rhyolite magmatism (Christiansen and Lipman, 1972). Subduction of the Mendocino fracture zone may have affected the migration of mid-Tertiary and younger magmatism (Glazner and Supplee, 1982). Extreme extension in the Basin and Range accompanied the early development of a transform boundary (the San Andreas fault) along the west margin of North America in the early Miocene. Peak mid-Tertiary magmatism may have accompanied this distension, as in eastern Nevada (Gans et al., 1987), but detailed temporal relations between extension and volcanism in the southern Basin and Range remain poorly known. Since the middle Miocene, high-angle faulting has accommodated a more limited extension of the crust, and has resulted in the present Basin and Range physiography. First transitional (calc-alkaline to alkaline) basalts and then alkali basalts and basanites were erupted in the Basin and Range during the prolonged late Tertiary–Quaternary period of extension.

Mesozoic history

Mesozoic history of the southern Basin and Range consisted of several episodes of magmatic activity, punctuated by deposition of continental sediments. The history has been reviewed by several authors (Hayes and Drewes, 1978; Dickinson, 1981), but details are obscured by limited exposures, large uncertainties in geochronology, and lack of focused study. At least two Jurassic magmatic episodes at 210–185 Ma and 165–145 Ma are indicated by U–Pb zircon dating (Haxel et al., 1984; Wright et al., 1981; Riggs, 1987; Reynolds et al., 1987; Asmerom et al., 1988) and paleomagnetic studies (Kluth et al., 1982; May and Butler, 1987).

This magmatism is probably related to the sweep of a Jurassic arc through southwestern North America (Anderson and Silver, 1978; Dickinson, 1981), and many of the volcanic rocks probably accumulated in calderas (Lipman and Sawyer, 1985). Recent work on the Jurassic and Lower Cretaceous parts of the Mesozoic in southern Arizona is summarized in Dickinson and Klute (1987). Lower Cretaceous Bisbee Group sedimentary rocks were deposited in a northwestern extension of the Chihuahua trough (Bilodeau, 1982). The lowest unit of the Bisbee, the Glance Conglomerate, is a syntectonic fan conglomerate (Bilodeau et al., 1987) derived from high-angle, fault-bounded block uplifts bordering graben or half-graben basins. The interfingering of Jurassic volcanic rocks with coarse clastic rocks suggests that Glance deposition extends back into the Jurassic (Vedder, 1984); alternatively, these clastic rocks could represent debris shed into local volcanic-subsidence basins and not be correlative with the type Glance. In southeast Arizona and New Mexico, the Glance was succeeded by shallow marine carbonate and clastic deposits. To the west, the thick Bisbee Group marine sedimentary rocks are correlated with continental sedimentary deposits, such as the Amole Arkose in the Tucson Mountains (Risley, 1987).

Late Cretaceous compressive deformation

After deposition of Bisbee Group sediments and before Late Cretaceous magmatic activity, a period of erosion and major compressive deformation affected southern Arizona. The style and extent of this compressional deformation remain controversial (Davis, 1979; Drewes, 1980, 1981). Drewes (1981) regards thrust faulting as being continuous in style with the thin-skinned thrust belt of the northern and central Cordillera and the Sierra Madre Oriental of Mexico. Rocks in southeast Arizona are interpreted as a belt of stacked, thin, thrust sheets with as much as hundreds of kilometers of horizontal translation. The inferred peak of this orogenic activity was about 75–80 Ma in the area around Tucson; welded tuff of the Salero Formation in the Santa Rita Mountains, dated at 72–73 Ma, postdates deformation. Compressive deformation in the Sierrita Mountains may involve some Late Cretaceous volcanic units (Fridrich, 1987).

In contrast, a basement-cored uplift model has been advocated by Davis (1979). Response to regional compression was interpreted as markedly inhomogeneous, causing homoclinal tilting, cylindrical folding, and high-angle reverse faulting in discrete structural domains during Late Cretaceous–early Tertiary deformation. Absence of regional thrust faulting was attributed by Davis (1979) and Haxel et al. (1984) to a rigid Precambrian basement covered by a thin, massive Paleozoic shelf sequence which resisted overthrusting. Dickinson (1984) has interpreted a major strand of the Hidalgo thrust of Drewes (1981) as a low-angle normal fault of mid-Tertiary age.

Late Cretaceous–early Tertiary magmatism

Late Cretaceous and early Tertiary volcanism and related plutonic activity in southern Arizona have been summarized by Lipman and Sawyer (1985). They identified 10 or more Late Cretaceous calderas in southeastern Arizona and southwestern New Mexico and recognized that Cenozoic faulting had disrupted these volcanic centers, resulting in preservation of caldera fragments in isolated ranges. Most exposed Late Cretaceous volcanic rocks appear to have accumulated in calderas, with the exception of mafic volcanic rocks in the Williamson Canyon volcanics (Koski and Cook, 1982) near Christmas, and the early Tertiary(?) andesitic volcanic rocks north of Safford, Arizona; both of these sequences probably formed as parts of andesitic stratovolcanoes. Similar mafic/intermediate-composition volcanic rocks are associated with the porphyry copper deposits in the vicinity of Santa Rita, New Mexico, and may also occur in the Pedregosa Mountains of southeast Arizona. Ash-flow tuff overlying andesitic volcanic rocks in the northern Santa Rita and Roskruge Mountains of Arizona may be the only remnants of the outflow facies of this extensive caldera field.

Porphyry copper mineralization related to Late Cretaceous–early Tertiary calc-alkaline plutons is extremely widespread in the southern Basin and Range province of Arizona and New Mexico (Fig. 1). At a number of localities, including Silver Bell (Sawyer, this volume), Sierrita, Copper Flat, Red Mountain, and possibly Ajo, porphyry copper ore deposits are associated with silicic caldera volcanism (Lipman and Sawyer, 1985). Strong porphyry copper alteration and mineralization at Charleston/Tombstone and Courtland/Gleason may also be related to Late Cretaceous calderas. Restoring extension across the San Pedro basin shows that the large porphyry copper deposit at San Manuel adjoins, and is the same age as, a caldera associated with the Copper Creek porphyry copper deposit east of the San Pedro. Intrusions below the level of any volcanic cover are associated with porphyry copper deposits in the Globe–Miami, Ray, Morenci, Lakeshore, and Sacaton–Casa Grande areas (Titley, 1982). The porphyry copper deposits of this

province have accounted for more than half of U.S. production in the last century.

Northwest-trending faults and their relation to Late Cretaceous porphyry copper mineralization have been discussed widely (Schmitt, 1966; Titley, 1976; Drewes, 1981; Keith and Wilt, 1986); west-northwest trends dominate in the Silver Bell Mountains, the southern Pinaleno Mountains, and the Dos Cabezas Mountains. Studies in southwest New Mexico (Seager, 1983) identified right-lateral strike slip motion of latest Cretaceous–early Tertiary age along west-northwest and northwest-trending faults that are related to basement-cored uplift. Stratigraphic offsets at Silver Bell indicate that oblique strike–slip faults were active concurrent with the final Late Cretaceous volcanism and intrusion; this style of faulting may have continued into middle Tertiary, but was complete by 25 Ma.

Cenozoic rocks and structure

The southern Basin and Range has experienced several episodes of deformation and magmatism in the Tertiary. There is little depositional record of the early Tertiary; it was probably a time of uplift and erosion. During the Oligocene and Miocene (36–15 Ma), there was widespread intermediate and silicic magmatism in southern Arizona (Shafiqullah et al., 1978; Drewes et al., 1986), perhaps beginning as early as late Eocene in New Mexico. In the Mogollon–Datil volcanic field (Excursion 6A), and the Chiricahua, Galiuro, Superstition, Peloncillo, Pyramid, and Animas Mountains, large silicic calderas erupted widespread ash-flow sheets and proximal lava flows; regional correlations between these centers have not yet been worked out. Middle Tertiary granite plutons occur in the Santa Teresa Mountains adjoining the Galiuro volcanics, in the Dos Cabezas Mountains and Peloncillo Mountains, and subvolcanic plutonic rocks are exposed in the Chiricahuas. The middle Tertiary granite plutons at Cochise Stronghold and in the Dos Cabezas Mountains may be analogues for deeper plutonic levels than hypabyssal rocks exposed in the mid-Tertiary Turkey Creek caldera of the Chiricahua Mountains. Pallister and du Bray (this volume) call on eruption of ash-flow tuff from ring and central vents, which were then intruded and clogged by less fractionated monzonitic magma from lower levels of a stratified chamber.

In addition, much of the middle Tertiary volcanic activity, especially in the Peloncillo, Whitlock, and Gila Mountains, resulted in development of extensive fields of basaltic andesite to andesite lava flows and numerous non-caldera silicic eruptive centers (Richter et al., 1981, 1983). These silicic eruptive centers range from relatively small dacite and rhyolite plugs and domes to large rhyolitic dome-flow complexes and associated pyroclastic deposits, such as the Rhyolite Peak–Ash Peak complex in the central Peloncillo Mountains (Walker and Richter, this volume). Many of the larger silicic eruptive centers are compositionally zoned; some have extremely evolved high-silica rhyolites.

Relation of the middle Tertiary calderas and other eruptive centers to regional tectonics is currently a matter of conjecture. Drewes (1981) projects regional thrust faults through basement rocks below the Turkey Creek caldera; his Apache Pass fault projects into a thick sequence of middle Tertiary rhyolite lavas, ash flows, and "intrusive" tuffs near Cochise Head, in the northern Chiricahua Mountains. It is intriguing to speculate about possible relationships between silicic magmatism and regional structures; were shallow magma chambers being tectonically unroofed by low-angle normal faults, or were magmas accumulating and venting along regional faults? Basin and Range extension clearly overlapped middle Tertiary silicic magmatism in the Mogollon–Datil volcanic field, and possibly in the Chiricahua, Superstition, and Galiuro Mountains; the degree to which range uplift and tectonic denudation are direct results of intrusion of silicic magma to shallow crustal levels remains an unanswered question.

Regional middle to late Tertiary extensional deformation dominates the structure and physiography of the southern Basin and Range. Two different generations and styles of extensional tectonism have been identified: an early period of extreme extension along low-angle normal or detachment faults (Anderson, 1971; Proffett, 1977; Davis and Hardy, 1981), and a later Miocene–Pliocene period of high-angle faulting that formed the current deep alluvial basins separated by bedrock horsts (Scarborough and Pierce, 1978; Eberly and Stanley, 1978). Some mountain-front contacts may follow the older extensional structures (Dickinson et al., 1987). The age of the older extensional faulting is probably between 25 and 13 Ma in southern Arizona (Coney, 1980). It is characterized by the development of low-angle detachment faults which separate ductilely deformed lower-plate mylonitic gneisses from brittlely deformed upper-plate middle Tertiary volcanic and sedimentary rocks; the latter are commonly rotated along listric normal faults that sole into the detachment (Davis, 1980, 1983). Middle Tertiary plutonism accompanied extensional deformation, and mylonitic fabrics were developed in some rocks as young as 21 Ma (Reynolds et al., 1986). Middle Tertiary mineralization is almost exclusively epithermal in character, in strong contrast to the dominant Late Cretaceous porphyry style of ore deposition.

South-central Arizona has little active seismicity; as a result, many of the basin boundary faults have been buried by late Tertiary and Quaternary sediments. Further east, in southeast Arizona and near the Rio Grande rift, late Quaternary faulting is more significant (Machette et al., 1986). Large volumes of late Pliocene and Quaternary basaltic rocks have been extruded concomitant with faulting in the Geronimo volcanic field, the Animas Valley, the Potrillo volcanic field, and the Rio Grande rift.

Geophysics

A crustal cross section for southern Arizona and New Mexico, based on seismic and gravity data (Sinno et al., 1981; Gish et al., 1981; Sinno et al., 1986) is shown in Fig. 2. Crust beneath the southern Basin and Range is about 25 km thick, and thickens east of the Rio Grande rift to about 50 km. The attenuation of crustal thickness in the southern Basin and Range may have occurred concurrent with Miocene and younger extension (Sinno et al., 1981; Perry et al., 1987). In these areas, the lithosphere has been greatly thinned, and asthenosphere is interpreted to be in contact with the base of the crust (Sinno et al., 1986; Olsen et al., 1987). The apparent thickening of crust from eastern Arizona into southwestern New Mexico (Fig. 2) may be only an artifact of the seismic transect, which cuts obliquely across the Basin and Range–southern Colorado Plateau boundary. Depth-to-basement, derived from gravity data (Oppenheimer and Sumner, 1980), reveals that elongate ranges of the southern Basin and Range are more continuous (as shallowly buried bedrock horsts) than is evident from

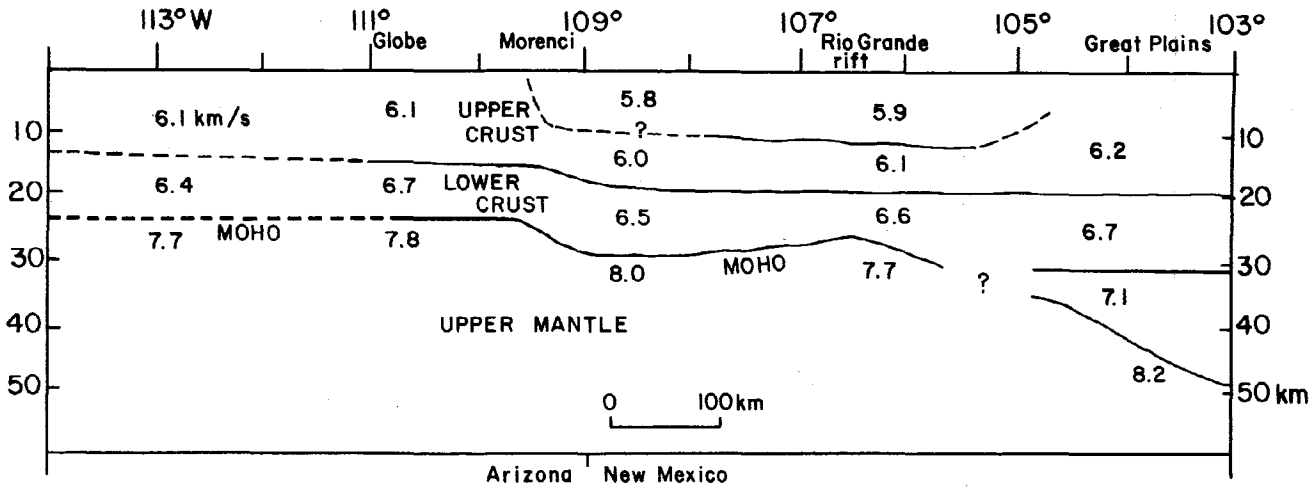

FIGURE 2—East–west cross section of southern Arizona and New Mexico showing crustal structure as inferred from seismic data (Sinno et al., 1981; Gish et al., 1981; Sinno et al., 1986). Approximate location of the cross-section line is shown in Fig. 1.

the distribution of mountainous areas at the surface. The basins are steep-sided and are filled with as much as 3–6 km of unconsolidated to partly consolidated sediments. Basin development is mainly post-Oligocene; more than 6 km of sediment has accumulated in the Tucson basin in the past 25 Ma (Anderson, 1987).

Xenolith studies

Mantle

The composition and geochemical characteristics of the mantle beneath southern Arizona are constrained by xenolith studies and by seismology. Upper mantle P_n seismic velocities range from 7.6 to 7.8 km/s (Sinno et al., 1981; Gish et al., 1981), corresponding to seismic velocities of pyroxene-rich, olivine-poor peridotites. Two major xenolith localities have been well studied within the Basin and Range of southern Arizona. These are the San Carlos locality at Peridot Mesa, north of Globe, and the Geronimo (San Bernadino) volcanic field in the southeasternmost corner of the state. Frey and Prinz (1978) described spinel lherzolites and spinel harzburgites (Cr-diopside group or Type I—Wilshire and Shervais, 1975; Frey and Prinz, 1978) as the dominant rock types in the San Carlos suite, along with pyroxene-rich xenoliths of alkaline igneous affinity (Al–Ti augite group or Type II). Type I spinel lherzolites and harzburgites are considered to be the residue from various degrees of partial melting and basaltic melt extraction and represent fragments of the upper mantle. Some harzburgitic lherzolites and harzburgites appear to have been metasomatically enriched in LIL-elements (K, U, LREE). The upper mantle harzburgites and lherzolites were invaded by veins of pyroxene-rich peridotite (± amphibole, phlogopite) and reflect the complexity and heterogeneity of mantle processes.

A generally similar distribution of ultramafic xenoliths has been described from the Geronimo volcanic field (Kempton et al., 1984; Kempton and Dungan, this volume). Clinopyroxene-depleted spinel lherzolites and harzburgites are the dominant rock types and attest to significant partial melting of the upper mantle on a regional scale. Clinopyroxenes in these rocks are Cr-diopsides that can be subdivided into two groups, one exhibiting LREE depletion (Type Ia), and the other having enriched LREE (Type Ib), attributed to metasomatic infiltration, possibly involving CO_2- and H_2O-rich fluids (Kempton et al., 1984).

The isotopic characteristics of these two suites show a broad range of variation. Initial Sr-isotope compositions of minerals and rocks range from 0.7017–0.7058 in the San Carlos olivine-rich rocks (Frey and Prinz, 1978) to 0.70197–0.70488 for the Geronimo xenoliths (Menzies et al., 1985) and 0.70177–0.70453 for Kilbourne Hole (Roden et al., 1988). Nd-isotope data for clinopyroxenes from the Geronimo Type I rocks have elevated values (0.513350–0.512584) typical of LREE-depleted sources that resemble oceanic mantle (Menzies et al., 1985); Kilbourne Hole Type I and II nodules range from 0.513326 to 0.512797. Alkali basalts also have depleted to moderately enriched mantle Nd- and Sr-isotopic signatures, similar to the ranges defined by mid-ocean-ridge basalt (MORB) and ocean-island basalt (OIB). Pb-isotopic data (Zartman and Tera, 1973) for xenoliths from San Carlos and Potrillo plot below the crustal-evolution curve of Stacey and Kramers (1975), but above MORB (Tatsumoto, 1978). The combined petrologic and geochemical data suggest a heterogeneous upper mantle dominated by long-term depletion of lithophile elements and subsequent metasomatic enrichment beneath the Basin and Range province of southern Arizona (Kempton et al., 1984).

Lower crust

Lower crustal rocks are not exposed in the Southwest, but characteristics of the lower crust can be inferred from xenoliths and geophysical measurements. However, caution should be exercised in such interpretations, as Padovani and Reid (this volume) note that seismic velocities and densities of metasedimentary xenoliths from Kilbourne Hole overlap with those of potentially underplated basaltic materials.

Lower crustal xenoliths from the western-interior craton of North America are dominantly granulitic rocks (Kay and Kay, 1981). Granulites from Kilbourne Hole in the Rio Grande rift (Padovani and Carter, 1977a) are both metaigneous (two-pyroxene granulites) and metasedimentary (sillimanite–garnet granulites) in origin. Charnockites (orthopyroxene-bearing granite) and minor anorthosite also occur. Metasedimentary garnet granulites are probably residues of pelitic sediments from which water-rich granitic melts were extracted. Nd- and Sr-isotopic studies of the Kilbourne

xenoliths by Richardson et al. (1980) showed that metamorphic recrystallization occurred within the last 10 Ma, but Pb systematics and a Rb/Sr isochron on one sample (Reid et al., 1982) indicate an original Proterozoic age. In contrast to inferences about the composition of the lower crust from other sources, Kilbourne Hole peletic granulites do not show evidence of long-term Rb, Th, and LREE depletion, nor do they show evidence of oxygen exchange (Padovani and Reid, this volume). La Olivina in Chihuahua (Cameron et al., 1983) has a similar assemblage of garnet granulitic metapelites to those from Kilbourne Hole. The many Colorado Plateau xenolith localities (McGetchin and Silver, 1972, and others summarized in Kay and Kay, 1981) also have similar lower crustal xenolith populations plus garnet–clinopyroxene and/or amphibole-bearing rocks such as Franciscan-type eclogite (Helmstaedt and Doig, 1975) and amphibolite.

Crustal xenoliths from the southern Basin and Range province may differ from those of the Colorado Plateau and Rio Grande rift. Recent work by Kempton (cited above) on mantle xenoliths from the Geronimo volcanic field in southeastern Arizona has been extended to crustal xenoliths (Kempton and Dungan, this volume). Lower crustal xenoliths are dominantly one- and two-pyroxene granulites that equilibrated at 840–960°C (Kempton and Dungan, this volume). These granulites are mafic to intermediate in composition and are divided into two groups based on their mineralogy and geochemistry: metagabbro with positive europium anomalies (cumulates), and metadiorites of calc-alkaline affinity. No mineral assemblages indicate a metasedimentary parentage. Absence of garnet indicates either that these granulites equilibrated at lower pressure than those from the Rio Grande rift or Colorado Plateau, or that appropriate aluminous protoliths were not present. Kempton (this volume) reports a 1.4 ± 0.4 Ga $^{207}Pb/^{206}Pb$ secondary isochron on the combined Geronimo granulite xenolith suite. She interprets the metacumulates as crystallization products of Cenozoic alkalic magmas that were contaminated with lower to middle crustal rocks similar to the Geronimo metadiorites. Padovani and Reid (this volume) obtained a 1.6 Ga Rb–Sr isochron by sampling individual layers in paragneiss xenoliths from Kilbourne Hole; however, they note that mineral isochrons (Rb–Sr and Sm–Nd) have been reset by heating related to Rio Grande rift formation.

Lower crustal nodules from San Carlos include garnet granulites and amphibolites, as well as two-pyroxene granulites (W. I. Ridley, oral comm. 1988). The crustal xenoliths provide lower crustal analogues that can be used in modeling crustal components in Mesozoic and Cenozoic silicic magmas in the southern Basin and Range. This approach has been applied at the Late Cretaceous Silver Bell caldera (Sawyer, 1987). It would clearly be appropriate to use the Geronimo suite for modeling a potential lower crustal component in the adjacent Chiricahua magmatic rocks. The distinctiveness of crustal xenoliths from the adjoining Potrillo and Kilbourne Hole localities (Padovani and Carter, 1977a) suggests caution in extrapolating lower crustal rock types from one area to another. However, it is probably reasonable to assume a dominantly granulitic (rather than eclogitic) lower crust beneath the Conrad discontinuity, based on seismic-refraction studies (Sinno et al., 1981).

Physical volcanology

The Ash Peak–Rhyolite Peak eruptive complex (Walker and Richter, this volume) provides a conceptual link between caldera-forming eruptive processes in the Chiricahua Mountains and basaltic volcanism in the Geronimo and Potrillo basalt fields. Pallister and du Bray (this volume) observed transitions between high-energy Plinian eruptions that produced ash-flow tuff deposits, and effusive eruptions that produced rhyolite lavas in eroded vents within the Turkey Creek caldera. At Ash Peak, transitions from Pelèean to Strombolian eruptions are inferred from rhyolite deposits that include pyroclastic flows, bedded-ash and base-surge deposits (some with bombs and impact structures), and rhyolite lava that appears to represent agglutinated rhyolitic spatter. Ash Peak is a pyroclastic breccia cone that is morphologically similar to the basaltic cinder and spatter cones of the Geronimo volcanic field.

Strombolian-style eruption of rhyolitic magma implies relatively low volatile contents or efficient pre-eruptive degassing (Eichelberger et al., 1986), a feature that characterized other mid-Tertiary rhyolite magma systems in the southern Basin and Range. Strombolian eruption, analogous to Hawaiian fire-fountaining, and low volatile contents are inferred for rhyolite lavas of the Black Range in southwestern New Mexico on the basis of field evidence and mineral chemistry (Duffield, this volume). Caldera formation in the Chiricahua Mountains was preceded by development of a high-silica rhyolite lava field; it would appear that volatile contents only episodically built up to the point necessary to drive large-scale Plinian eruptions and caldera collapse.

Although the Ash Peak rhyolite was probably relatively "dry," the ash and lapilli are largely converted to zeolites. The timing of zeolitization is unknown. It is possible that some Ash Peak eruptions may have been phreatomagmatic, offering an alternative driving mechanism for the ballistic and surge deposits. Phreatomagmatic explosions are commonly cited as an important mechanism for maar formation. Kilbourne Hole maar has a tuff ring composed mainly of comminuted sedimentary rocks, and was formed primarily by phreatomagmatic explosions that took place when alkali basalt, containing abundant lower crustal nodules, came into contact with ground-water-saturated sediments of the Santa Fe Group within the Rio Grande rift. In contrast, maars of the Geronimo volcanic field are dominated by juvenile basaltic cinder and spatter, favoring a magmatic volatile-driven eruptive (diatreme) mechanism.

Field guide to the Late Cretaceous Silver Bell caldera and porphyry copper deposits in the Silver Bell Mountains

David A. Sawyer

U.S. Geological Survey, Denver, Colorado 80225

Introduction

The field trip will examine evidence for a Late Cretaceous caldera at Silver Bell that is closely associated in time and space with the porphyry copper deposits of the district. The main emphasis will be on the volcanic sequence on the east side of the Silverbell Mountains and caldera-collapse megabreccia composed of Paleozoic sedimentary blocks on the southwest side of the mountains. These sedimentary rocks are host to major skarn deposits along strike with a caldera-collapse megabreccia horizon. There will be one hike of about 2 km and less than 300 m elevation gain. A more detailed road log (containing additional stops and intermediate mileage) is available in Sawyer (1986), and detailed petrology, geochemistry, and stratigraphic descriptions can be found in Sawyer (1987).

Starting from downtown Tucson, the mileage begins at the intersection of I-10 West and Speedway Boulevard. This is the same starting point as for the Tucson Mountains caldera field guide (Lipman, this volume), although, if both trips are planned for the same day, it is possible to go directly from Silver Bell to Gates Pass in the Tucson Mountains (instructions at the end of this log).

Road log

Mileage

0.0 **Head northwest** on I-10 West from Speedway Blvd. **3.0**

3.0 Overpass over Prince Road. To the west are the Tucson Mountains, site of this afternoon's field trip. The Tucson Mountains are also a Late Cretaceous caldera with related intrusive rocks (Lipman, this volume). **8.0**

11.0 Cortaro Road exit. To the west is Safford Peak, a mid-Tertiary dacitic intrusive plug (Brown, 1939). The northern Tucson Mountains are entirely mid-Tertiary volcanic rocks. View to the northeast at about 1:30–2:00 of the Tortolita Mountains, a metamorphic-core-complex range discussed by Davis (1980). **9.0**

20.0 **Turn right** off I-10 at the Marana exit. **Turn left** at the stop sign and continue underneath the freeway overpass; pass frontage road; **turn right** at the next intersection (a Chevron station is on the southeast corner of the intersection, and a Circle K convenience mart on the southwest). Proceed west on Trico–Marana Road. **1.5**

21.5 Heading west on Trico–Marana Road after passing the Post Office, a regional view of the mountain ranges around the Silver Bell Mountains (see Fig. 1 of Introduction for reference) is as follows: Tucson Mountains to the south (at 8:30); farther south (9:00) are the Sierrita Mountains. The largest Laramide batholith in southern Arizona, the Ruby Star Granodiorite, outcrops in this range. Upper Cretaceous volcanic rocks accumulated in a caldera associated with the large Pima district porphyry copper deposits in the Sierrita Mountains (Lipman and Sawyer, 1985; Fridrich, 1987).

Low mountains in the foreground (10:00) are the Roskruge Mountains, composed of Upper Cretaceous volcanic rocks, minor Upper Cretaceous intrusive rocks, and mid-Tertiary volcanic rocks. The Upper Cretaceous volcanic rocks are mainly rhyolite welded tuffs, the only remnant of a larger ash-flow plateau. In the foreground, north of the Roskruge Mountains (11:00), are the Waterman Mountains which are composed of complexly faulted Paleozoic sedimentary rocks and only a few Upper Cretaceous or middle Tertiary igneous rocks.

The central Silver Bell Mountains (11:00 to 12:00) are composed of Upper Cretaceous volcanic rocks and comprise most of the view to the west. The highest peak at the south end of the central Silver Bell Mountains is Silver Bell Peak. The very jagged high peak at the north end of the Silver Bell Mountains is Ragged Top, an Oligocene rhyolite dome that was emplaced along the Ragged Top fault. The geology of the east side of the Silver Bell Mountains will be described in more detail at Stop 1.

Low hills to the northeast (12:00 to 1:00) of the Silver Bell Mountains are the Samaniego Hills. Middle Tertiary volcanic rocks, mostly basalt to basaltic andesite in composition (R. Ashley, unpubl. mapping), unconformably overlie a basement of Precambrian granite north of the Ragged Top fault. Picacho Peak, at 3:00 to the north, is also middle Tertiary volcanic rocks, mostly andesitic lavas and breccias. The Picacho Mountains to the north of Picacho Peak are composed of core-complex mylonitic gneiss (Davis, 1980). **4.6**

26.1 Stop sign at junction of Trico–Marana Road with Trico Road; **continue straight** ahead. For approximately the next 15 mi the trip will be on unpaved roads. **0.5**

26.6 Second stop sign on Trico–Marana road; junction with Silver Bell Road. **Turn right** on Silver Bell Road and head north. **1.7**

28.3 Intersection with Cherokee Road; road forks. **Bear left** and continue west on Silver Bell Road toward the Silver Bell Mountains. **4.8**

33.1 To the left at 9:30 is Red Hill, a small knoll made up of Precambrian biotite granite containing K-feldspar megacrysts. It is lithologically similar to other members of the 1.40–1.45 Ga transcontinental anorogenic granite suite (Anderson, 1983). Leached K-feldspar from this locality gives a 1.4 Ga com-

mon-Pb model age using the Stacey/Kramers curve (1975). **1.6**

34.7 Fork in the road. **Bear left,** as Silver Bell Road bends sharply away to the north. Head west toward the Silver Bell Mountains. **1.0**

35.7 Junction with the El Paso Natural Gas pipeline road. **Turn left** (south). First stop is 1 mi south on gas pipeline road. **1.0**

36.7 **STOP 1. Overview of the east side of the Silver Bell Mountains.** All directions are given facing in the direction of the central Silver Bell Mountains (west) as 12:00. The peak at the south end of the range is Silver Bell Peak, the highest elevation in the range at 1299 m (4261 ft). Ragged Top, elevation 1191 m (3907 ft) is the prominent sharp peak at 2:00, northeast of the main range. The geology of the east side of the Silver Bell Mountains is illustrated on the geologic map of the Silver Bell Mountains (Fig. 1), which shows the general route of the field trip.

The Upper Cretaceous stratigraphic section is capped by the Cat Mountain Tuff, erupted from the Tucson Mountains caldera (P. W. Lipman, D. A. Sawyer, and J. Hagstrum, unpubl. data). This unit was previously called the tuff of the Mount Lord Volcanics (Sawyer, 1987). It is a eutaxitic rhyolite welded tuff about 200 m thick that makes up all the high peaks of the central Silver Bell Mountains. Because the Silver Bell Mountains have been tilted 30–35° east-northeast by post-Cretaceous faulting (probably during middle Tertiary extension), most of the east flank of the range is a dip-slope developed on this resistant rock. The southeast spur of Silver Bell Peak has been lifted up to the south by a northeast-trending normal fault. The stratigraphic succession below the lower contact of the Cat Mountain Tuff can be seen on this ridge.

Underlying the Cat Mountain Tuff are the Silver Bell Volcanics, a sequence of andesitic to dacitic extrusive rocks and related volcaniclastic rocks. On the ridge, these rocks are represented by a thin (less than 30 m) layer of debris-flow deposits containing dacitic clasts. The Silver Bell Volcanics are best exposed in the pedimented area on the east side of the Silver Bell Mountains in the immediate foreground. The Cat Mountain Tuff wedges out against a paleo-Silver Bell volcano at about the range front.

Beneath the Silver Bell Volcanics, on the southeast spur of Silver Bell Peak, is a thin sequence of Claflin Ranch Formation bedded pyroclastic deposits. Underlying these volcaniclastic rocks, the middle and lower reaches of the slope are made up of the tuff of Confidence Peak, which is the intracaldera tuff of the Silver Bell caldera. It is a low-silica rhyolite welded tuff that will be seen at Stops 2 and 3. It is also exposed in the pedimented area southeast of Ragged Top, over an area of several square kilometers, where it was uplifted as a fault block. Through the saddle south of Silver Bell Peak, a major swarm of quartz monzodiorite porphyry dikes extends east-northeast from the Oxide pit mineralized center. Most of the low hills east-southeast

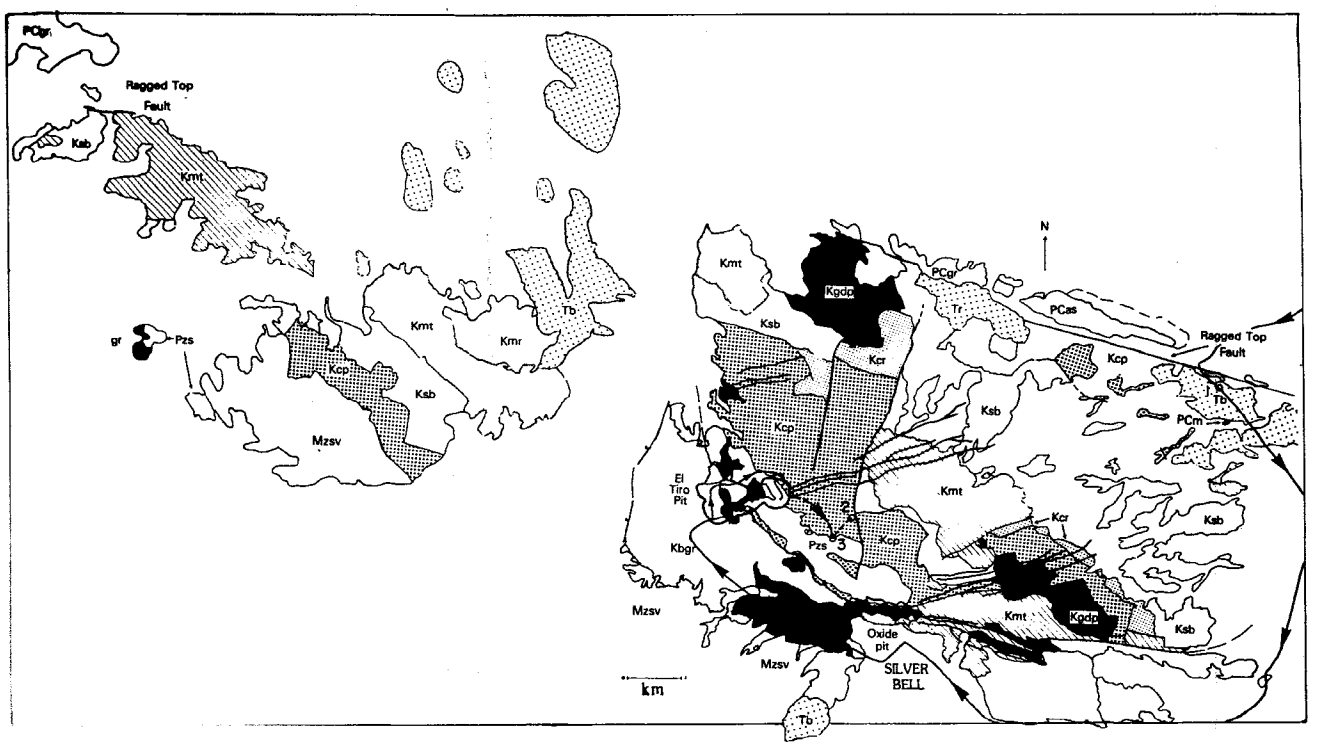

FIGURE 1. Geologic map of the Silver Bell and West Silver Bell Mountains, showing road route and stops on field trip. Field-trip route enters map area by road on the northeast side of map, north of the Ragged Top fault. Map symbols: PCgr = Precambrian 1.4 Ga granite; PCm = Precambrian metamorphic rocks; PCas = Precambrian Apache Group sedimentary rocks; Pzs = Paleozoic sedimentary rocks (entirely caldera-collapse megablocks in the central Silver Bell Mountains); Mzsv = Mesozoic sedimentary and volcanic rocks; Kbgr = El Tiro biotite granite; Kcp = Cretaceous tuff of Confidence Peak; Kcr = Cretaceous Claflin Ranch Formation; Ksb = Cretaceous Silver Bell Volcanics; Kgdp = Cretaceous granodiorite porphyry; Kmt = Cat Mountain Tuff; Kmr = Cretaceous Mount Lord Volcanics, flow-banded rhyolite member; black pattern-Kqmp = quartz monzodiorite porphyry suite and monzodiorite porphyry; Tb = Tertiary basaltic or mafic volcanic rocks; Tr = Ragged Top rhyolite; gr = granite, unknown age.

of Silver Bell Peak are composed of the tuff of Confidence Peak overlain by Claflin Ranch Formation sediments and Silver Bell Volcanics. These units are cut (in this area) by a granodiorite porphyry pluton that predates the Cat Mountain Tuff. The Upper Cretaceous volcanic stratigraphy and related plutons are shown in a schematic geologic column (Fig. 2). Detailed descriptions of the lithologic characteristics and petrology of the units are given by Sawyer (1987).

At Stop 1, subcrop exposures and float are of middle Tertiary volcanic rocks that unconformably overlie the Late Cretaceous sequence. These flows, domes, and low shields form a belt extending from the Samaniego Hills, to the north at 4:00, across the pedimented east slope of the central Silver Bell Mountains, down to the Pan Quemado Hills east of the Waterman Mountains at about 9:30. They range in composition from basalts to dacites; basaltic andesites and andesites occur most abundantly. The low hills due south of Stop 1 are erosional remnants of an andesite flow that has been dated at 28.6 Ma (Mauger et al., 1965, recalculated to new constants).

Beyond the low hills southeast of Silver Bell Peak are the sharp peaks of the Waterman Mountains.

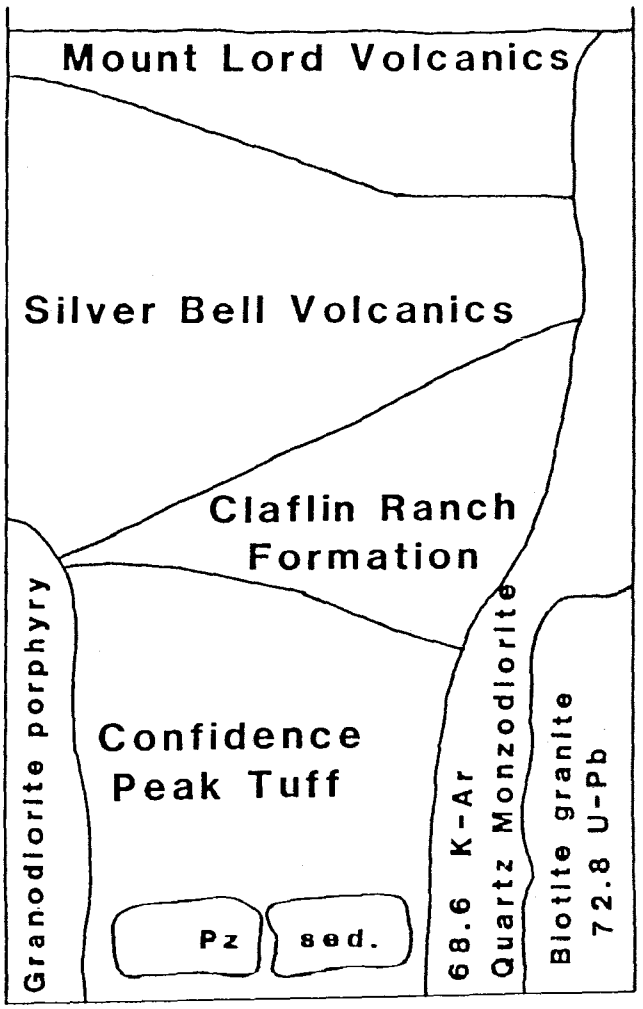

FIGURE 2—Schematic geologic column, central Silver Bell Mountains, showing the principal Upper Cretaceous igneous units and their stratigraphic relationships.

The Paleozoic section of the Waterman Mountains is complexly faulted and the rocks are lithologically and structurally distinct from Paleozoic rocks exposed in the Silver Bell Mountains. Mesozoic sediments that predate Late Cretaceous igneous activity occur in the low area between the Silver Bell and Waterman Mountains. A major west-northwest-trending fault zone separates the thick Upper Cretaceous section in the Silver Bell Mountains from Mesozoic and Paleozoic sedimentary rocks to the south.

A similar west-northwest-trending fault that had strike–slip movement bounds the Silver Bell block to the north. The Ragged Top fault is a N75–80W structure, where tightly constrained from south of Red Hill to Ragged Top, and extends for at least 5 km and probably 20 km farther west. Ragged Top is an Oligocene (25.7 Ma; Mauger et al., 1965) rhyolite dome erupted along the trace of the Ragged Top fault. It was extruded after fault movement. An Upper Cretaceous granodiorite porphyry pluton is truncated by the fault, constraining the age of the movement on the Ragged Top fault to between latest Cretaceous and Oligocene time.

North of the Ragged Top fault are rocks that have had a fundamentally different history than those in the Silver Bell block. Precambrian granite and Middle Proterozoic Apache Group sedimentary rocks (in low hills just east of Ragged Top) are unconformably overlain by middle Tertiary volcanic rocks in the Samaniego Hills. The Silver Bell block can thus be viewed as a relative down-dropped graben containing 2–3 km of Upper Cretaceous volcanic, plutonic, and sedimentary rocks. It is separated from areas with differing geologic histories by west-northwest-trending faults that had probable strike–slip movement. Precambrian rocks in the Silver Bell block are quartz–muscovite schist, different in age and lithology from those north of the Ragged Top fault.

Return to vhicles; **head south** on gas pipeline road. **1.2**

37.9 White gate: **open, bear left** through fence line and continue on main road after **closing gate.** **0.5**

38.4 **Turn right** on dirt road heading southwest, just ahead of white gas-line sign on right side of road. Continue southwest on principal dirt track, ignoring small roads splitting off to either side. **2.1**

40.5 Cocio Wash; **continue south across wash** on main route. On far side of wash **turn right** (west-southwest) at road junction. Continue on main track, avoiding fork to left and two forks to right along powerlines. **1.4**

41.9 Intersection with Avra Valley Road; **turn right** on paved road. **3.2**

45.1 American Smelting and Refining Company (ASARCO) office at Silver Bell. Gate at entrance to mine is locked most of the time. **Permission to enter must be obtained from ASARCO** Southwest Regional Office in Tucson and waivers signed before entering mine property. If mine is open, **check in at office. Proceed** onto ASARCO property for continuation of field trip.

Head north from the entrance of the mine. **Take**

left fork at the first junction, pass the pit office and maintenance buildings to the left and veer right up to the main haulage road. **Turn left** (west) on the main haulage road. Be sure to **drive on the left side** of the road. **0.9**

46.0 Precipitation plant to east. Striking east beneath the precipitation plant is the fault that separates Mesozoic sedimentary rocks south of Silver Bell from the Upper Cretaceous quartz monzodiorite porphyry and volcanic rocks to the north. The Oxide pit porphyry copper deposit of the Silver Bell mining district occurs behind the waste dumps to the east and north. **1.8**

47.8 Pass waste dumps of the El Tiro pit porphyry copper deposits as we enter it from the south. **0.5**

48.3 Enter the main El Tiro pit. **0.8**

49.1 Daisy pit on the left, main El Tiro pit on the right. Both pits are principally mined for supergene chalcocite mineralization. These secondary copper blankets are underlain by quartz monzodiorite porphyries having potassic alteration and stockwork chalcopyrite mineralization. **0.4**

49.5 Quartzite Hill on the left, probably Cambrian Bolsa Quartzite. It is a Paleozoic block in caldera-collapse megabreccia within the intracaldera tuff of Confidence Peak. **0.2**

49.7 Drop into the East Extension of El Tiro pit; Confidence Peak is straight ahead, with the microwave tower atop the peak. **0.2**

49.9 **Turn left** on the road going along the east side of the East Extension of El Tiro pit. Without 4WD vehicle this stretch of road will have to be hiked. Views to the west are of skarn mineralization in the East Extension. The relatively unmineralized Imperial pluton can be seen on the northwest shoulder of the pit. Road is closed after ~1 km at berm. **1.0**

50.9 **STOP 2. Confidence Peak Viewpoint.** Park and hike to the viewpoint. The easiest route is up the road that heads southwest along the edge of the waste dumps, and then south up a ridge composed of tuff of Confidence Peak containing caldera-collapse megabreccia of Paleozoic sedimentary rocks. Upon reaching the ridge crest, head east and intersect a road that runs along the crest of the ridge to the microwave tower.

Stop just east of the microwave tower at the top of the mountain. Confidence Peak is a central viewpoint that provides a panorama of the entire western side of the Silver Bell Range, and all the mountain ranges to the west and north. At this observation point we will discuss the geology of the west side of the Silver Bell Range.

Walk to the east end of the parking area at the top of Confidence Peak. Facing east, directly ahead in the central Silver Bell Mountains is Angel Peak. This will be our 12:00 reference point.

Starting to the south at 3:00 (right), is the Oxide pit of the Silver Bell mining district. Just beyond it are the Waterman Mountains which have been described previously. At 1:00, Silver Bell Peak can be seen. At 11:00 is an unnamed peak to the north of Angel Peak, and just beyond it Ragged Top, the Tertiary rhyolite dome. Looking back at about 7:00 to 8:00 is the El Tiro mineralized center of the Silver Bell mining district. Beyond the El Tiro mineralized center are mountain ranges rising to 2500–3000 ft that make up the West Silver Bell Mountains.

The geology of the central Silver Bell Mountains that can be seen from this point will be described starting with the youngest stratigraphic unit. Silver Bell Peak, Angel Peak, and all of the main ridge crest of the central Silver Bell Mountains are capped by Cat Mountain Tuff. The lower contact of the Cat Mountain Tuff can clearly be seen on the northwest side of Silver Bell Peak at 1:30. It dips to the east-northeast at 25–30°. Following the skyline ridge downslope from Silver Bell Peak, some yellowish-tan knobs can be seen. These are outcrops of the northwest-trending middle Tertiary rhyolite dikes that cut through the Silver Bell district. Stratigraphically beneath the Cat Mountain Tuff are the Silver Bell Volcanics which are between 100 and 350 m thick on the west side of the Silver Bell Range. Rocks in the Silver Bell Volcanics in this vicinity are mostly volcaniclastic, either clast-supported, texturally variable andesite breccias or andesitic mudflow material. Beneath the Silver Bell Volcanics occurs a very thin (less than 2 m) layer of Claflin Ranch Formation sediments, mostly pyroclastic material in this area. The Mount Mammoth fault drops the main Silver Bell Range down to the east against the tuff of Confidence Peak on Confidence Peak.

The tuff of Confidence Peak is at least 1.5 km thick west of Silver Bell Peak and Angel Peak in the Silver Bell caldera. This is a minimum thickness, because holes have been drilled through the tuff into Paleozoic sediments and back into tuff, where they bottomed. Looking to the south from Confidence Peak to the Oxide pit, bluffs of white Paleozoic limestones can be seen. These are made of Devonian Martin Formation and the Mississippian Escabrosa Limestone. They are caldera-collapse megabreccia contained within the Silver Bell caldera, and will be visited at Stop 3, which will be a hike on the west side of Confidence Peak. This zone of caldera-collapse megabreccia occurs low within the tuff of Confidence Peak, about 1 km beneath its top.

The Paleozoic sedimentary caldera-collapse megabreccia grossly comprises a horizon that extends from the Oxide pit through the El Tiro pit. The western contact of the Paleozoic sediments, out of view from this point, is the ring fault of the Silver Bell caldera. The ring fault of the Silver Bell caldera extends east-southeast of the Oxide pit on the south side of the Silver Bell Mountains (Richard and Courtright, 1966). From the Oxide pit to the El Tiro pit, it trends N45–50W. West of the ring fault is precaldera biotite granite that is cut by the fault. The tuff of Confidence Peak and caldera-collapse megabreccia included within it are dropped down to the east against the steeply dipping ring fault. North of El Tiro, the trend of the ring fault changes to N10W so that it makes an arcuate trend from west-northwest to north-northwest along the southwest side of the range. The ring fracture is mainly intruded by plutons of the quartz monzodiorite por-

phyry. Large intrusions occur at the main mineralized centers at Oxide, El Tiro, and North Silver Bell. Smaller dike-like intrusions occur between the El Tiro and the Oxide pits.

From the north side of the parking area we will examine the geology to the north. The El Tiro mineralized center and its three pits can be seen to the northwest. In the East Extension of El Tiro pit, Paleozoic sediments are mineralized to form significant skarn-ore reserves. Approximately 30 million tons of skarn ore was mined from the East Extension of El Tiro. In the main El Tiro pit, a chalcocite blanket overlies hypogene potassic alteration and porphyry copper ore in the quartz monzondiorite porphyry. The Daisy pit to the north of the main El Tiro pit is also chalcocite-blanket mineralization, and has hypogene potassic alteration and mineralization beneath it. Beyond the El Tiro pit, megabreccia of Paleozoic sedimentary rocks extends north to the BS & K mine.

The West Silver Bell Mountains can be seen extending to the west beyond the El Tiro pit. Paleozoic sedimentary rocks occur in the very southwest corner of the West Silver Bell Mountains and are overlain by Lower Cretaceous sedimentary rocks partly equivalent to the Amole Arkose (Banks and Dockter, 1976). These rocks were tilted by Late Cretaceous deformation and are unconformably overlain by the Upper Cretaceous volcanic rocks erupted from the Silver Bell caldera. The central northwest-trending ridge in the West Silver Bell Mountains is made up of a series of five small-volume pyroclastic flows that represent outflow of the tuff of Confidence Peak outside the Silver Bell caldera. The swale between the middle ridge and the northern northwest-trending ridge is made up of Silver Bell Volcanics overlying the tuff of Confidence Peak. The highest peaks on this northwest-trending ridge are made up of Cat Mountain Tuff. In the West Silver Bell Mountains, the Cat Mountain Tuff (equivalent to that seen in the central Silver Bell Mountains) is overlain by sediments and flow-banded rhyolites of the Mount Lord Volcanics (Banks and Dockter, 1976). Overlying the Upper Cretaceous volcanic rocks are middle Tertiary volcanic rocks extending to Malpais Hill, which is made up of basalt. The peak at the very northwest end of the West Silver Bells is composed of Precambrian granite north of the Ragged Top fault.

The area north and west of Silver Bell shows why southern Arizona is the leading copper producing state, with its many porphyry copper deposits. To the north-northwest is the Sacaton porphyry copper deposit and the Case Grande West mineralization hidden beneath the alluvium adjoining it. West of the West Silver Bells are the Slate Mountains and the Lakeshore porphyry copper deposit on the west side of the range. Beyond it is Vekol Mountain (the nipple-shaped peak) with another significant porphyry copper deposit not yet exploited.

STOP 3. Caldera-collapse megabreccia. Hike 150 m west of the microwave tower parking lot, to the switchback where the road curves back down the hill. Note the strong epidote-facies propylitic alteration of the tuff of Confidence Peak here, as well as the common lithic fragments. Large, relatively mafic pumice can be seen in some blocks of tuff. Drop approximately 100 m and walk 0.75 km west from here. The purpose of this stop is to examine relationships between the intracaldera tuff of Confidence Peak and the caldera-collapse megablocks of Paleozoic sedimentary rocks. Our route will include stops at five areas to look at particular exposures (3A–3E; Fig. 3). Textures of remobilized limestone and tuff at the contact between these two units are seen at Stop 3A. Different Paleozoic rock types will be identified through varying degrees of thermal alteration (Stop 3B–3D). Criteria for distinguishing caldera-collapse megabreccia from caldera floor will be discussed. At the contacts of many discrete megabreccia blocks, tuff can be observed to penetrate the contacts and blocks. At the southern limit of the hike (Stop 3E), a quartz monzonite dike that contains large orthoclase phenocrysts and has an intrusive breccia sleeve will be seen. The intrusive breccia sleeve has a variety of clast types, including Paleozoic limestones and biotite granite clasts.

From Confidence Peak return to the parking area at the waste dump east of El Tiro, and then back to the road where it enters the East Extension of El Tiro pit. **1.0**

51.9 **Optional STOP 4. Skarn mineralization in East El Tiro.** When the haulage road is intersected at the East Extension of El Tiro, **park and hike** southwest down into pit. Geology and mineralization are described in Graybeal (1982) and Einaudi (1982). A geologic cross section showing relationships between tuff of Confidence Peak, biotite granite, and quartz monzodiorite porphyry intrusions, and the different styles of mineralization in the El Tiro mineralized center, is shown as Fig. 4, modified from Graybeal (1982).

After visiting the East Extension of El Tiro, **double back** to main El Tiro pit. **Turn left** into main pit of El Tiro. **2.3**

54.2 **Optional STOP 5. Bottom of El Tiro pit** (2550 level). Examine hypogene potassic alteration and mineralization in the quartz monzodiorite porphyry suite. Features of the mineralization and alteration in the main El Tiro pit are described by Richard and Courtright (1966) and Graybeal (1982).

From here **return to ASARCO Silver Bell Mine Office** and then to Tucson (41.1 mi) via Avra Valley Road. To join with the Tucson Mountains half-day trip (Lipman, this guide) without returning to Tucson: (1) Turn south at Sandario Road; the turn-off is 17.9 mi east of the Silver Bell Mine Office on Avra Valley Road (across from the Avra Valley Airport); (2) Head south on Sandario Road, turn left onto Mile-Wide Road and follow signs first to Sonora Desert Museum and then to Gates Pass; (3) Pull off at parking area south of the major bend in the road immediately before climbing final stretch to Gates Pass—this is the second parking area (Point B) of Lipman (this guide), where his Stop 1 hike begins.

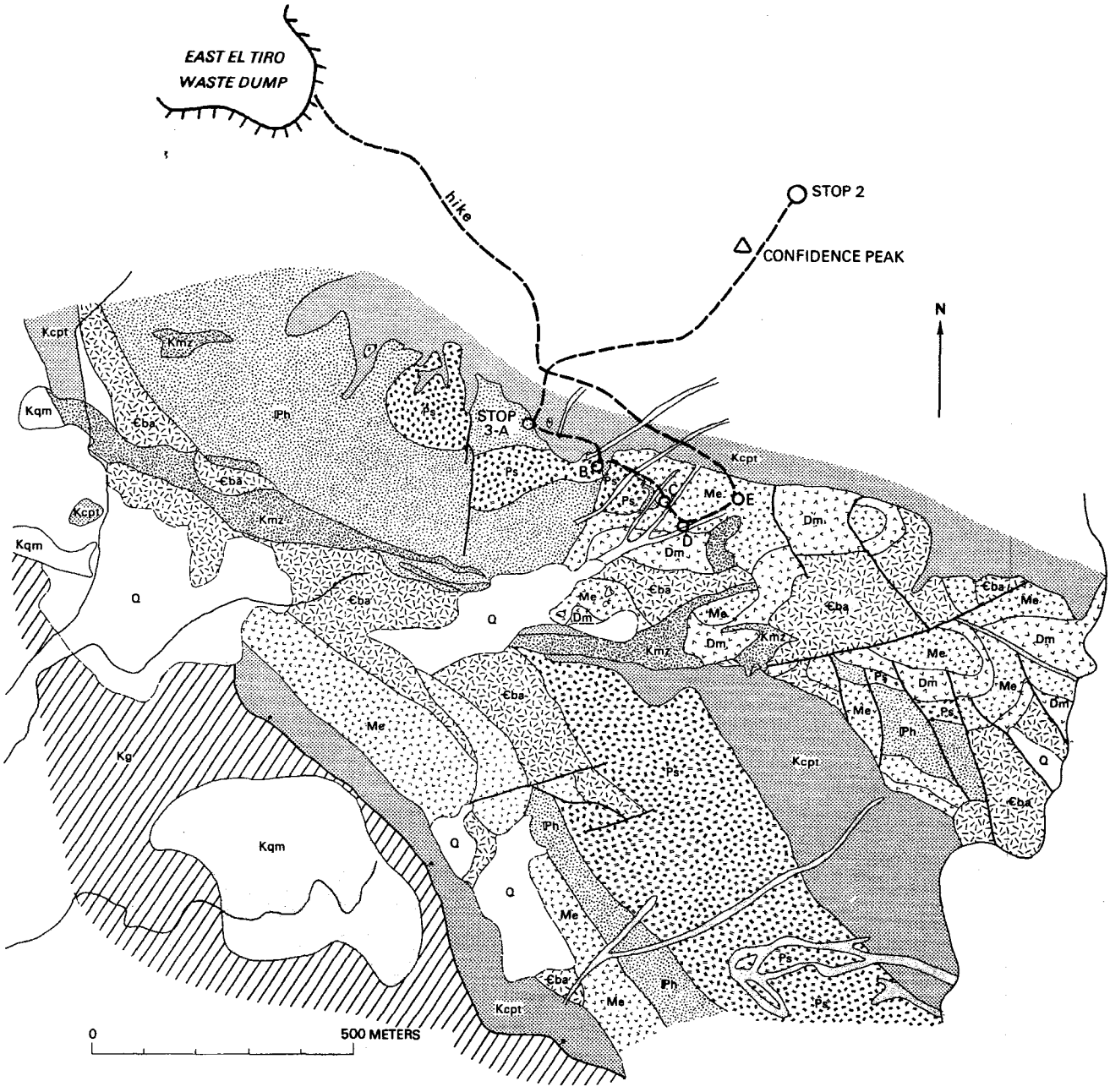

FIGURE 3—Geologic map of caldera-collapse megabreccia in the area between El Tiro and Oxide pits. Hiking route depicted from East El Tiro waste-dump parking area to Confidence Peak. Stop 2 is an observation point on the east side of Confidence Peak. Stop 3, and its five substops, A–E, show relationships between the intracaldera Confidence Peak Tuff and caldera-collapse megabreccia composed of Paleozoic sedimentary blocks. Map symbols: Kg = Cretaceous El Tiro biotite granite; Kcpt = tuff of Confidence Peak; Kqm = Cretaceous orthoclase quartz monzonite porphyry; and Kmz = Cretaceous monzodiorite porphyry. Different slabs of caldera-collapse megabreccia are represented by their protolith Paleozoic sedimentary composition: Cba = Cambrian Bolsa Quartzite and Abrigo Formation; Dm = Devonian Martin Formation; Me = Mississippian Escabrosa Limestone; IPh = Pennsylvanian Horquilla Limestone; Ps = Pennsylvanian–Permian sedimentary rocks, especially Earp Formation. Elongate gray bands and irregular bodies are Cretaceous quartz monzodiorite porphyry or orthoclase–quartz monzonite dikes.

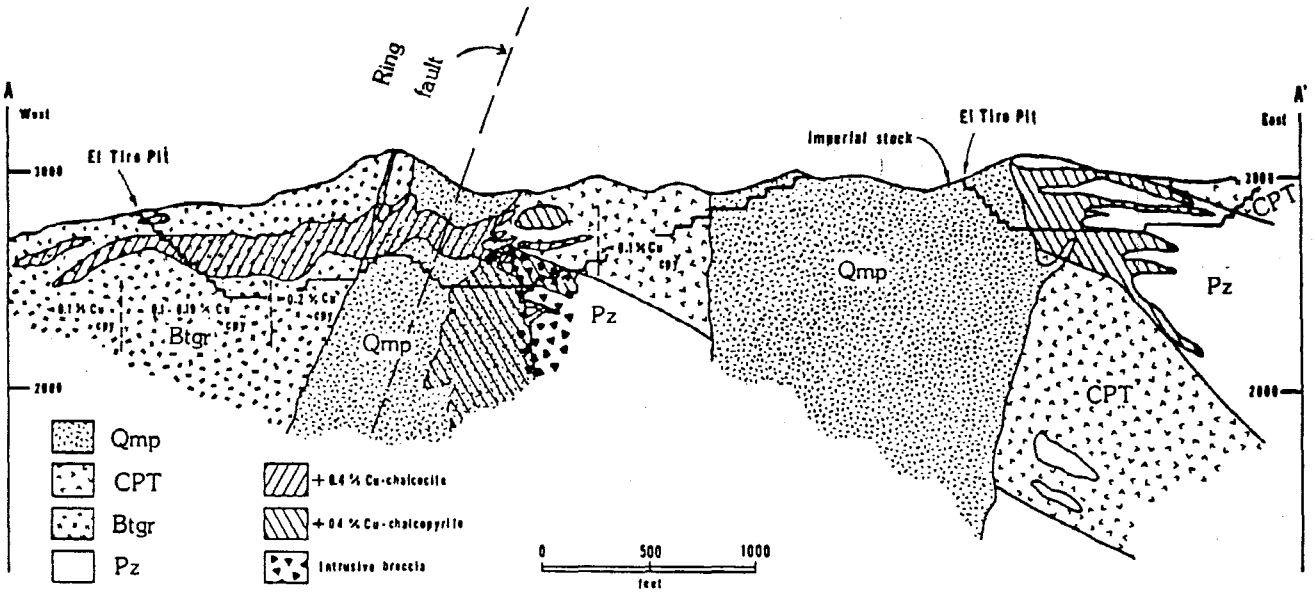

FIGURE 4—Cross section of El Tiro pit area, slightly modified from Graybeal (1982: 490, fig. 24.3) to reflect present stratigraphic nomenclature. QMP = quartz monzodiorite porphyry suite intrusions including quartz monzodiorite, and biotite–quartz-monzonite porphyries, intruded along the ring-fracture zone; CPT = the intracaldera tuff of Confidence Peak, within the Silver Bell caldera; Btgr = precaldera biotite-granite intrusion that is cut by the ring fault; Pz = Paleozoic sedimentary rocks included as caldera-collapse megabreccia within the intracaldera tuff of Confidence Peak. Vertical scale along side axes is in feet above sea level.

Field guide to the Tucson Mountains caldera

Peter W. Lipman

U.S. Geological Survey, Denver, Colorado 80225

Introduction

The Tucson Mountains, a low desert range just west of Tucson (Fig. 1), are underlain largely by Upper Cretaceous volcanic rocks interpreted as parts of the fill of a large ash-flow caldera (Lipman and Sawyer, 1985).

The origin of these rocks has been much discussed. The range was mapped in its entirety by Brown (1939), and several small areas were restudied by University of Arizona graduate students in the 1960's, working largely under the direction of Evans Mayo (Mayo, 1963, 1971a, 1971b; Assadi, 1964; Bikerman, 1963; Kinnison, 1958; Knight, 1967). Brown (1939) mapped an upper unit, the Cat Mountain Rhyolite (Tuff, of general present usage), overlying a breccia unit which he called the Tucson Mountain Chaos and interpreted it as related to regional thrusting. Mayo (1963, 1971a) interpreted the breccia as volcanically erupted intrusive breccia related to a regional "volcanic orogeny." Bikerman (1963) recognized the ash-flow origin of the Cat Mountain Tuff, but inferred that the chaos breccia represented stoped fragments, rafted from deeper levels by the rising pyroclastic magma that later erupted the Cat Mountain Tuff. A similar interpretation was developed in more detail by Mayo (1971b). Brown, Mayo, and Bikerman all considered the chaos to be a basal layer beneath the Cat Mountain Tuff. Drewes (1981, pl. 9) remapped the central Tucson Mountains, also showing the breccia blocks to underlie the Cat Mountain Tuff in a matrix that he assigned to the Silver Bell Formation—mapped by him as a regional Upper Cretaceous andesitic unit extending at least from the Silver Bell Mountains on the north to the Santa Rita and Sierrita Mountains on the south.

Lipman (1976) inferred, largely from published descriptions, that the Tucson Mountain Chaos was landslide breccia associated with collapse of an Upper Cretaceous ash-flow caldera within which the Cat Mountain Tuff had ponded. In-progress fieldwork confirms such an interpretation and also shows that the slide breccias, rather than underlying the Cat Mountain Tuff, have a matrix of nonwelded tuff and interfinger with welded tuff at multiple horizons (Figs. 2, 3). A major implication of this interfingering is that the exposed thickness of the caldera-filling Cat Mountain Tuff is at least 3–4 km, many times that previously reported. Megablocks are up to 0.5 km across and include Paleozoic sediments, Jurassic silicic volcanic rocks, Cretaceous andesitic lavas, and tuff of Confidence Peak erupted from the Silver Bell caldera. Dominant breccia types vary greatly

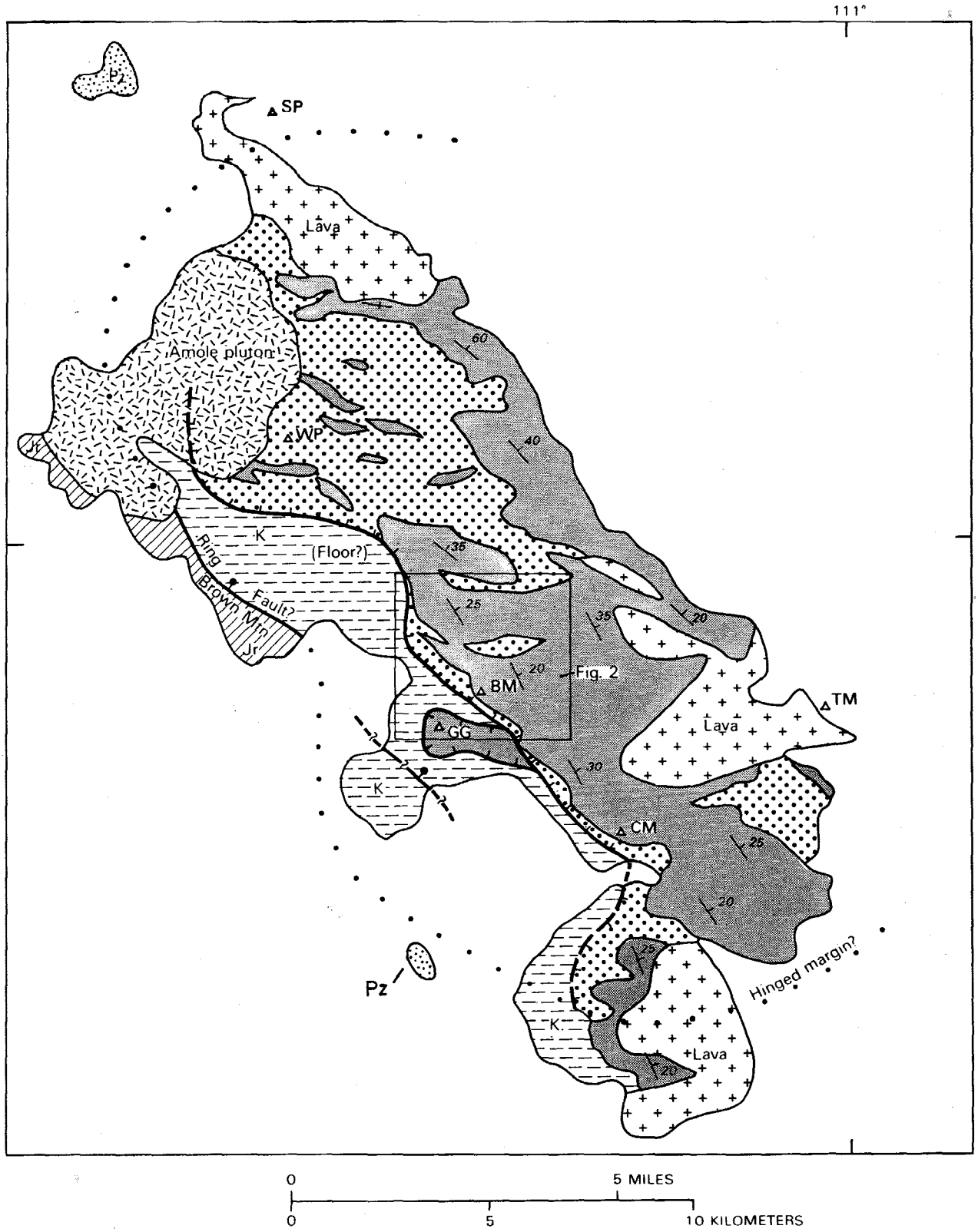

FIGURE 1—Generalized geologic map of early Tertiary and older rocks, showing structural interpretation of the Tucson Mountains caldera (based on mapping by Lipman, 1986–87; in part modified from Brown, 1939). Many small Tertiary normal faults omitted. Extracaldera units: Pz, Paleozoic sedimentary rocks; Jr, Jurassic(?) sedimentary and volcanic rocks. Caldera-floor rocks: K, Cretaceous Amole Arkose of the Bisbee Group. Caldera-related igneous rocks of Laramide age: shaded unit, intracaldera Cat Mountain Tuff; dotted unit, intracaldera landslide-breccia deposits ("Tucson Mountain Chaos"), containing megablocks up to 0.5 km across; crosses, caldera-filling lava flows ranging in composition from andesite to rhyolite. Amole pluton is interpreted as ring intrusion. Hachured contact indicates base of caldera-filling tuffs and breccias. Geographic localities: BM, Bren Mountain; CM, Cat Mountain; GG, Golden Gate Mountain; SP, Safford Peak; TM, Tumamoc Hill; WP, Wasson Peak.

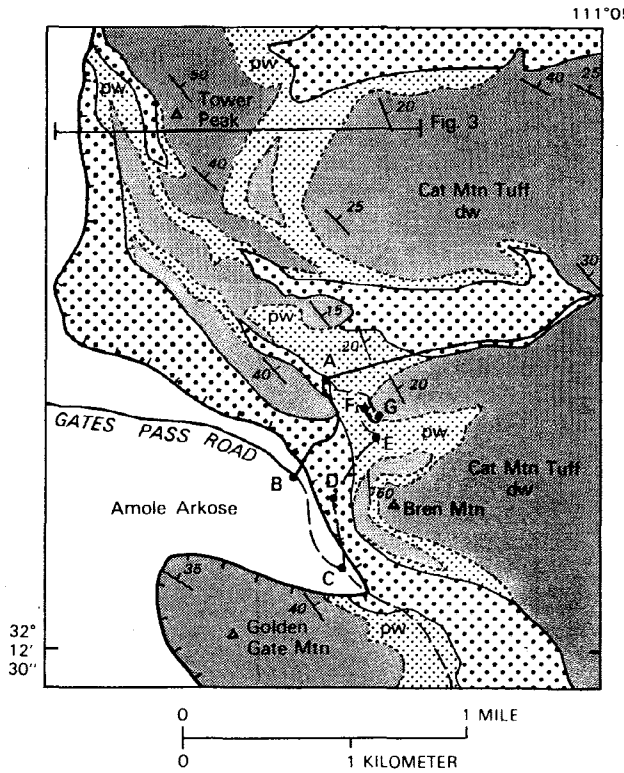

FIGURE 2—Preliminary geologic map of Tucson Mountains caldera fill in the Gates Pass area (mapping by Lipman, 1987–88). Units: Cat Mountain Tuff, nonwelded to partly welded (pw, light stipple) and densely welded (dw, shaded unit); intracaldera slide breccias (dotted). Hachured line indicates base of caldera-fill deposits, against autochthonous Cretaceous sedimentary rocks (Amole Arkose). Dashed line, trail followed by field-trip route; reference points indicated by letters (A to G).

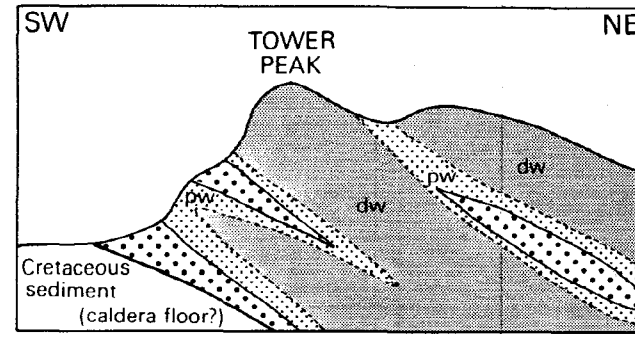

FIGURE 3—Diagrammatic cross section through the west margin of the Tucson Mountains caldera north of Gates Pass, illustrating interfingering relations between Cat Mountain Tuff (pw, nonwelded to partly welded; dw, densely welded) and intracaldera slide breccias (dotted pattern).

between various caldera sectors. Small bodies of rhyolitic rock in the northern Tucson Mountains, previously mapped as irregular intrusions by Brown and Drewes (Amole Latite, Latite Porphyry), are reinterpreted as discontinuous lenses of Cat Mountain Tuff that fill interstices between large disrupted masses of Mesozoic sedimentary rock. The result of this interpretation is to include a sizeable additional area as caldera-fill breccia.

A small segment of the structural boundary of the caldera may be represented by an arcuate fault along the northwest flank of the range that drops Cretaceous sedimentary rocks against Jurassic rocks on Brown Mountain (Fig. 1). Cretaceous sedimentary rocks, exposed low along the west flank of the mountain range, may represent part of the caldera floor, or they may be low on the western caldera wall between the exposed outer ring fault and concealed inner structures to the east. An unresolved problem, if the sediments are part of the caldera floor, is the apparent absence of in-place precaldera andesitic lavas above the sediments, even though such lavas occur widely as slide blocks within the caldera fill.

Along the northeast and southeast flanks of the Tucson Mountains, the Cat Mountain Tuff is conformably overlain by andesitic to rhyolitic lavas that are interpreted as erosional remnants of a thick caldera-fill sequence emplaced soon after collapse and involved in caldera resurgence. These lavas obscure the northern and southern caldera margins. The large, zoned, granodioritic to granitic Amole pluton exposed along the northwest flank of the Tucson Mountains appears to be a resurgent ring intrusion that arches the caldera fill, including postcaldera lavas, upward to the east and north. In addition, the entire range, including flanking middle Tertiary lavas, is variably tilted eastward, probably due to rotation along largely concealed listric normal faults associated with middle Tertiary uplift of the Catalina–Rincon core complex east of Tucson. The ages of the caldera-related volcanic rocks are well constrained as Late Cretaceous by published conventional K–Ar ages (Bikerman and Damon, 1966), but further work would be desirable to evaluate more precisely the time span between eruption of the Cat Mountain Tuff and emplacement of the apparently resurgent Amole pluton.

Within northern parts of the caldera fill, slide breccias dominate over ash-flow tuff (Fig. 1), documenting catastrophic subsidence in this sector. In contrast, along the inferred southern caldera margin, the thickness of tuff decreases to only about 100 m, and megabreccia is virtually absent; these relations suggest a hinged southern caldera margin and overall trap-door geometry. Thus, virtually the entire mountain range is interpreted as an oblique section through the structurally disrupted interior of a caldera; the caldera margins are largely concealed by Tertiary basin fill. Although poorly constrained, especially to the east, the overall dimensions of the Tucson Mountains caldera are about 20 × 25 km, slightly smaller than the Pleistocene Long Valley caldera, and well within the spectrum of late Cenozoic calderas in the western United States (Fig. 4).

The single field-trip stop, at Gates Pass, permits a 2–3 hour loop hike that provides a partial section from caldera floor up through lower parts of the caldera fill, leading to a panoramic view of the northern Tucson Mountains from a scenic highpoint.

Field mapping and petrologic studies of the igneous rocks of the Tucson Mountains are currently in progress (1988), and interpretations presented here are preliminary.

Road log

Mileage

0.0 Central Tucson: intersection of I-10 and Speedway Blvd.; **proceed west on Speedway.** Ragged ridge crest of Tucson Mountains to west is capped entirely by Upper Cretaceous Cat Mountain Tuff. The general structure is a homoclinal sequence dipping 15–35° eastward. **3.1**

3.1 Passing Painted Hills Road. Hills to south are Upper Cretaceous(?) dacite lava dome of Twin Hills, con-

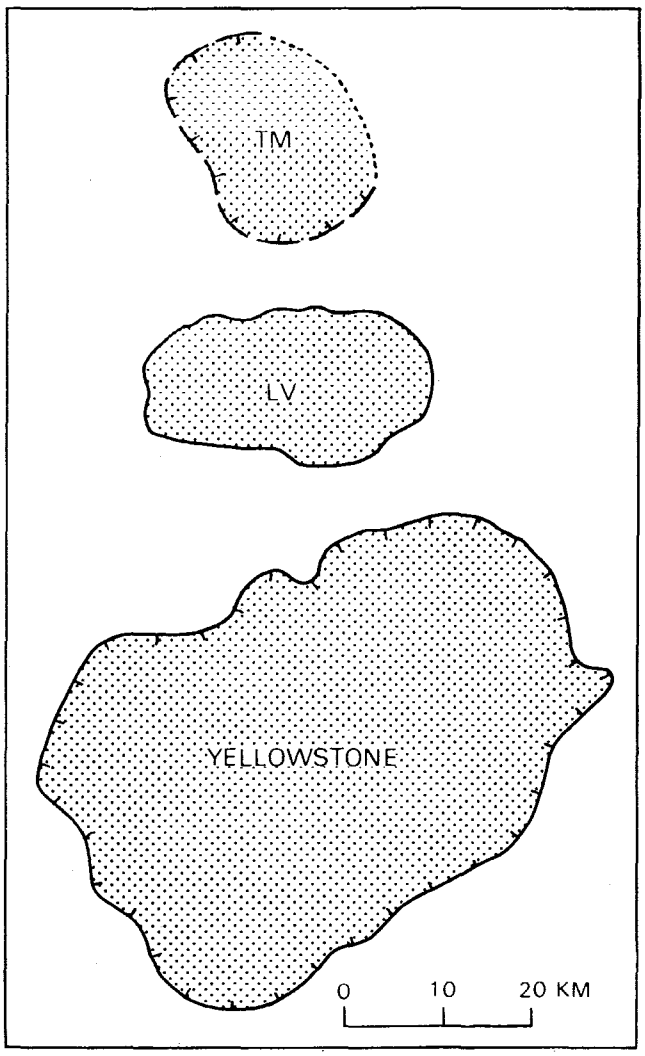

FIGURE 4—Inferred map outline of the Tucson Mountains caldera (TM), in comparison with large young calderas of the western United States (LV, 0.7 Ma Long Valley; 0.6 Ma Yellowstone).

formably overlying the ash-flow fill of the Tucson Mountains caldera. **0.9**

4.0 Contact in a small gully between dacite lava and underlying east-dipping Cat Mountain Tuff to west, dropped along small northwest-trending fault against more Cat Mountain Tuff to east. **0.6**

4.6 **Bear left,** following Gates Pass Road (to Old Tucson). **1.6**

6.2 Entering Tucson Mountains Park. As we proceed up toward pass, variably colored rocks in gully to right are megablocks of diverse lithologies along welding break within Cat Mountain Tuff. The largest and most conspicuous blocks in this area consist of flow-layered and locally spherulitic rhyolitic lava of probable Jurassic age. These were considered to be intrusions by Brown (1939), Bikerman and Damon (1966), and other earlier workers. **1.0**

7.2 **STOP 1. Gates Pass loop** (Fig. 2). Pull off into parking lot on right, about 25 m before crest of pass. **Proceed on foot** from Point A 0.45 mi (750 m) across pass (3172 ft elevation) and down-section along paved road to second parking area (Point B) at major bend in road **(ROAD TRAFFIC IS HEAVY AND VISIBILITY IS POOR; EXTREME CAUTION NEEDED).**

At this point we will be in Cretaceous sedimentary rocks, seemingly part of the caldera floor. The trip route will **follow a foot trail** to a saddle between Bren Mountain (3988 ft) and Golden Gate Mountain (4288 ft), remaining within the Cretaceous sedimentary rocks. Then, we will angle back toward Gates Pass on a higher foot trail to the east, which provides excellent exposures of diverse block lithologies within the Cat Mountain Tuff. Eventually, we will climb to top of the 3530 ft point, providing a panoramic view of the northern Tucson Mountains and adjacent ranges. Finally, continuing along the foot trail, we will return to Gates Pass.

Leaving the Gates Pass parking area, we cross the pass, carved in a large steeply dipping megablock of Cretaceous sandstone. These sedimentary rocks are locally called the Amole Arkose (Brown, 1939), though they include interbedded sandstone, siltstone, and finely bedded local limestone; they are part of the Bisbee Group. Most contacts between the block and adjacent tuff are poorly exposed, but along the road about 50 m west of the pass, the block of Amole Arkose is in contact with lithic-rich, weakly welded Cat Mountain Tuff. The Cat Mountain Tuff is a compositionally uniform, low-silica rhyolite (70–72% SiO_2) that contains phenocrysts of quartz, feldspar, and sparse biotite (where not obscured by alteration).

The Cat Mountain Tuff here also contains blocks of andesitic lava at least several meters across. Note that as the tuff becomes less lithic-rich upward from road level, it also becomes more welded as indicated by collapsed-pumice foliation. Such features are typical of caldera-filling tuff, in which large lithic fragments act as heat sinks and inhibit welding (Fig. 3).

About 0.15 mi (250 m) west of pass along road, prominent rugged outcrops at road level are a densely welded zone of Cat Mountain Tuff containing relatively sparse lithic fragments. This welded zone is both overlain and underlain by less welded tuff containing abundant large blocks of andesite and other rock types. Note the irregular foliation and decrease in welding adjacent to blocks beneath the most densely welded tuff, in contrast to sparsity of blocks within the most welded tuff. The disaggregated mass of reddish sandstone here was probably derived from the Jurassic Recreation Redbeds, which are exposed in place on Brown Mountain near the Tucson Desert Museum about 5 km to the northwest.

Looking back across road to the north, note similar densely welded tuff dipping southeastward beneath the megablock zone just examined in the roadcuts. Some faulting may be present in this area, but no major faults can thus far be mapped for any distance.

At 0.35 mi (550 m) west of pass, where road bends to the left, is exposed a block of Paleozoic limestone several meters across, along with other brecciated sedimentary lithologies in obscure contact with weakly welded quartz-bearing tuff.

Just before road curve to the northwest, with large

parking area on south side (Point B), are exposures of gently dipping Amole Arkose that are apparently in place on the caldera floor, or possibly low on the wall.

From this parking area, **walk south up the trail to the saddle** that separates Bren Mountain (on the northeast) from Golden Gate Mountain (on the southwest). The trail is entirely within Amole sedimentary rocks of the caldera floor that are discontinuously exposed beneath the colluvial debris.

At trail crossing the main gully, the many boulders of densely welded Cat Mountain Tuff are typical of the cliffs above and similar to the late welded tuffs (Mount Lord Volcanics) that cap the crest of the Silver Bell Mountains 50 km to the northwest. The good exposures ahead along the east side of the gully are Amole Arkose. Detailed mapping of these sedimentary rocks by Assadi (1964) for a M.S. thesis at the University of Arizona, and also by Harald Drewes of the U.S. Geological Survey (1981, pl. 9), show that they are broadly folded around north-northwest-trending axes.

About 100 m up-valley along the trail, exposed in a side gully to the east between exposures of Amole Arkose, is a large dark-gray block of limestone (Permian?). The block is enclosed within the nonwelded lower part of the Cat Mountain Tuff, beneath large massive cliffs of lithic-poor welded tuff. Linear yellowish-brown outcrops, trending along the slope just above the limestone megablock, are exposures of a dike of Cretaceous dacite, part of a regional swarm (Silver Lily Quartz Latite) in this sector of the Tucson Mountains. This area was mapped in great detail by Mayo (1971a, 1971b, fig. 2).

At the saddle (Point C), **bear left** (east) on a more obscure trail that leads toward the limestone megablock and back towards Gates Pass. Note the eastward and southeastward dips indicated by slabby jointing of the tuff on Golden Gate Mountain to the west. The section to the east is probably raised by a small fault through the saddle. The high point visible through the pass to the south, just east of the large trailer-park development, is geographic Cat Mountain; it consists entirely of densely welded Cat Mountain Tuff overlying megablocks and in-place Amole sedimentary rocks at the base of the slope adjacent to the trailer park. In the far distance are the Santa Rita Mountains, site of another Cretaceous caldera fragment (Lipman and Sawyer, 1985); a high point in the range (Mount Hopkins, elevation 8550 ft), barely visible to the right, consists mostly of granitic rocks along the east margin of this caldera.

Heading back along the upper trail toward the conspicuous block of Paleozoic limestone, the trail crosses Cretaceous sandstone near the contact between in-place Amole Arkose (caldera floor?) and overlying megablock debris in a tuffaceous matrix at the base of the Cat Mountain Tuff. Large dark-brown outcrops, just to the right (south) of the Paleozoic limestone, are blocks of Cretaceous andesitic lava, again as megablocks enclosed in a tuff matrix.

About 75 m along the trial, in a small gully just before the limestone block, are reddish sediments of Jurassic Recreation Redbed type, juxtaposed with fragments of laminated limestone of a type locally characteristic of the Amole Arkose.

Beyond the Paleozoic block is voluminous float of porphyritic andesite, derived from blocks of such Cretaceous volcanic rocks upslope. **Be alert for a fork in the trail (Point D); stay high.** At this point the trail is obliquely traversing the contact zone between in-place Cretaceous sedimentary rocks and overlying megablock-rich Cat Mountain Tuff. Below the trail, the sedimentary rocks are stratigraphically and structurally coherent; at trail level and above, blocks of Amole Arkose are incorporated as fragments, along with the other rock types just noted, in a tuff matrix.

The trail then crosses below and around a large mass of brecciated and mostly structureless (but locally flow-laminated) rhyolitic lava of probable Jurassic age. This block is at least 15 m across.

The trail continues northward, mainly through talus of welded Cat Mountain Tuff from cliffs above, to a spur ridge that descends directly toward the parking area below. Above the trail on this spur is another large mass of light-colored rhyolitic lava. The trail then climbs obliquely upward, around and through the margins of this rhyolite mass, where contacts are locally exposed between the rhyolite and partly welded Cat Mountain Tuff containing small angular fragments of andesite. Here, the Cat Mountain has compaction foliations that dip anomalously steeply to the north, reflecting draping around the rhyolite block.

The trail continues ahead toward a prominent spur, where it crosses about 25 m above the upper contact of another large mass of light-colored brecciated rhyolite. On the way, the trail crosses several smaller masses of Cretaceous andesitic lava and Amole sandstone enclosed by somewhat altered, partly welded Cat Mountain Tuff.

From the rhyolite block, the **trail continues obliquely upward** through partly welded, light-colored tuff, toward more welded, brown, cliff-forming outcrops, **then descends below the cliffs.** Dips in these welded tuffs are variable, from 30° to 50° east; some variation may be due to slumping on the steep slopes, but much is interpreted as due to variable draping arund and over the large megablocks below trail level.

Looking north across the main road, we can see several prominent cliff-forming welded horizons in the Cat Mountain Tuff, separated by benches or gentler slopes, along which large megablocks are also present (Fig. 2). Thus, the megablocks occur at multiple horizons within the Cat Mountain Tuff, not just beneath it as previously thought. This relation becomes increasingly pronounced northward along the range front and to the northeast. Also, looking northward, try to distinguish where we saw densely welded tuff and megablocks at road level.

Continue eastward to the conspicuous saddle (Point E), then descend northward following an obscure and rather eroded trail. Descending and

contouring northward, we pass another large block of Cretaceous sandstone that is mostly above the trail. Consider how irregular the contact is between the densely welded tuff above us and the zone of megablocks below. How much is due to depositional irregularities, versus possible faults in the saddle?

The **trail then switchbacks up** through variably welded and altered Cat Mountain Tuff, to a prominent shoulder southeast of Gates Pass parking area (Point F).

Across Gates Pass to the northeast, the ridge crest is capped by densely welded Cat Mountain Tuff. The dip is steeper than it appears, 20–30° or greater, because this ridge is nearly parallel to the strike of the tuff. Below the cliffs of welded tuff, several large light-colored knobs and more obscure darker ones are masses of volcanic rock enclosed in tuff; the light knobs are Jurassic rhyolite like that just crossed along the trail, and the dark exposures are Cretaceous andesite. This zone of decreased welding containing megablocks is stratigraphically above the level at which we are standing.

Continue up to the viewpoint southeast from the shoulder (10 min.), following the eroded **trail** that **first switchbacks upward** and **then contours counterclockwise** around south side of the hill. This trail provides access to excellent exposures of densely welded Cat Mountain Tuff, previously seen only in talus, and also some welcome afternoon shade if the day is hot.

All slopes in sight to the south and east are Cat Mountain Tuff. The subtle variations in jointing and color, though not well understood, probably reflect mainly initial variations in welding and crystallization of the thick caldera-filling tuff.

From the top of this knob (Point G) we can see for the first time the Silver Bell Mountains, 50 km to the northwest, and some of the ASARCO tailing ponds from the porphyry copper open-pit operations. This is an excellent place to discuss relations between the Silver Bell and Tucson Mountains calderas. In a nutshell, tuff erupted from the Silver Bell caldera (tuff of Confidence Peak) is present as megablocks within the younger Tucson Mountains caldera, and the welded tuff member of the Mount Lord Volcanics that caps the Silver Bell Mountains is interpreted as outflow Cat Mountain Tuff from the Tucson Mountains caldera. These correlations are confirmed by distinctions in petrography and minor-element compositions, as well as paleomagnetic-pole positions (unpubl. data, J. Hagstrum, USGS).

Also visible from here are: Brown Mountain, the Tucson Desert Museum, and the approximate location of the possible caldera boundary fault that drops the Cretaceous against Jurassic sediments in that area (Fig. 1). The hills to the northeast expose the south margin of the Amole pluton that appears to have resurgently uplifted the northwest side of the caldera, perhaps localized along this ring fault.

Major remaining field problems involve determining the total thickness of the caldera fill, including postcollapse lava flows of Late Cretaceous or early Tertiary age, the structural position of the Amole Arkose (true caldera floor, or low on the wall), and the amount of rotation and transport of the Cretaceous rocks along middle Tertiary detachment faults.

Retrace route downslope to shoulder; then **follow trail northwest to Gates Pass parking area** (Point A).

Field guide to volcanic and plutonic features of the Turkey Creek caldera, Chiricahua Mountains, southeast Arizona

John S. Pallister and Edward A. du Bray

U.S. Geological Survey, Denver, Colorado 80225

Summary—Erosion and Basin–Range faulting in the Chiricahua Mountains expose multiple levels through the ~25 Ma Turkey Creek caldera. The caldera is 20 km in diameter and its structural boundary is occupied by an annular ring of quartz monzonite and monzonite porphyry; this porphyry appears to represent the margin of a saucer-shaped (upper surface) intrusion that is also exposed centrally within the caldera. Stratigraphic and structural data indicate that emplacement of the porphyry closely followed eruption of ash-flow tuff of the Rhyolite Canyon Formation; gradational textures and compositions suggest that the tuff and the porphyry were derived from the same magma reservoir.

The Turkey Creek caldera is unusual in preserving relicts of feeder zones for ash flows. Field, petrographic, and geochemical data document a gradation between high-silica rhyolite welded tuff and monzonite porphyry. The annular ring of porphyry is interpreted as the feeder zone for basal dacite lava flows within the caldera moat; textures in the ring grade from porphyritic granophyre to glass-matrix lava. Compositions cluster at ~66% SiO_2 and 77% SiO_2, but a few samples have intermediate silica abundances. The high-silica porphyry overlaps compositionally with the Rhyolite Canyon Formation tuff. Rocks that are mineralogically and texturally transitional between monzonite porphyry and ash-flow tuff occur within the ring body, as well as along fault-controlled feeder zones within the caldera. The latter suggest local brittle failure of the caldera-floor rocks (mainly preaccumulated intracaldera tuff) during the waning stages of ash-flow eruption, resulting in central, as well as ring-fracture, eruption of ash-flow tuff and rhyolite to dacite lava. These features indicate that ash-flow tuff was erupted from vents which were intruded and then clogged by less fractionated magma (the monzonite porphyry).

An unusual roof breccia occurs at the contact between the central monzonite intrusion and overlying intracaldera tuff. Regionally, the roof breccia is a complex zone that contains fragmental rocks with both tectonic and

pyroclastic or magmatic/hydrothermal origins. Monolithologic granophyre roof breccias are considered tectonic, but lack clear evidence of megascopic shear. Instead, they show characteristics of low-pressure shock metamorphism. Working models to explain the brecciation of these rocks include: (1) the combined effects of intrusion, cooling, and inflation of a laccolithic body of monzonite within the caldera, (2) magmatic explosions with foci within an underlying magma reservoir and focusing of compression or rarefaction waves at the porphyry—welded tuff contact, (3) hydrothermal brecciation produced during fluid migration and degassing of the underlying monzonite intrusion.

Thick sedimentary breccias and volcaniclastic sandstones in the southern part of the caldera unconformably overlie, and contain clasts of, Rhyolite Canyon Formation tuff and monzonite porphyry. The sedimentary rocks are overlain in turn by aphyric high-silica rhyolite moat lavas. The temporal progression from high-silica rhyolite ash-flow tuff to dacite moat lava and monzonite porphyry to aphyric rhyolite moat lavas and dikes defines a chemical trend from >75% SiO_2 to <65% SiO_2, and then (after an erosional interval) back to >75% SiO_2.

The features described above are consistent with a magma chamber and eruptive model in which the less-evolved lower parts of a stratified magmatic reservoir were drawn up into, and locally erupted effusively from, the same conduits and vents that initially fed large-volume ash-flow eruptions of high-silica rhyolite. The near-absence of precaldera rocks within the Turkey Creek caldera (caldera-floor rocks) is difficult to reconcile with the classical caldera paradigm. If the central monzonite intrusion represents the in-situ lower part of the source magma chamber for the ash-flow tuff, a very shallow magma chamber (with a thin and ephemeral roof) is required. However, the central intrusion may also represent a thick (>1 km) sill or laccolith that was intruded into the intracaldera tuff during the waning stages of caldera collapse. Interpretation of the roof breccia is pivotal to distinguishing between in-situ magma chamber and syn- or post-collapse laccolith-intrusion models.

Introduction

In the Chiricahua Mountains, faulting and erosion have combined to expose a three-dimensional view of an ash-flow caldera, its host rocks, and its comagmatic intrusive rocks. Here, we can directly observe both the volcanic and hypabyssal to plutonic levels of a single mid-Tertiary magmatic system.

Darwin Marjaniemi (1969) first recognized the Turkey Creek caldera and produced an excellent reconnaissance-scale (1:125,000) geologic map of the Chiricahua Mountains (Fig. 1). The caldera is a collapse structure 20 km in diameter that developed in basement composed mainly of Lower Cretaceous Bisbee Group sedimentary rocks and mid-Tertiary rhyolites, but regionally also containing a thick and tectonically complex sequence of Paleozoic carbonates and Precambrian crystalline rocks. Caldera collapse (at 25–26 Ma) and eruption of ash-flow tuffs of the Rhyolite Canyon Formation was preceded by development of a field of high-silica rhyolite lavas and domes (~28–26 Ma) and by collapse of the adjacent Portal caldera in the eastern Chiricahua Mountains (Bryan, this volume). Intrusive rocks related to the Turkey Creek caldera crop out in a broad ring dike and central intrusion composed of monzonite to quartz monzonite porphyry. These rocks are feldspar porphyries with granophyre (quartz–alkali feldspar) groundmasses; they overlap the monzonite–quartz monzonite model boundary (IUGS nomenclature). For the sake of brevity, we refer to these intrusive rocks as "monzonite," although we acknowledge both the hypabyssal porphyritic texture and the range in modal composition from monzonite to quartz monzonite (and locally to more quartz-rich compositions).

Early workers (Raydon, 1952; Epis, 1956; Sabens, 1957; Cooper, 1959; Fernandez and Enlows, 1966) recognized and mapped Tertiary rhyolite lavas and ash flows in the region. Enlows (1955) defined the Rhyolite Canyon Formation on the basis of stratigraphic sections in the outflow sequence at Chiricahua National Monument, but Marjaniemi (1969) alone defined the volcanic framework for this and other "process-oriented" studies. Marjaniemi estimated the volume of ash flows within the Rhyolite Canyon Formation to be about 500 km^3. His K–Ar mineral ages (recalculated using IUGS constants—Steiger and Jager, 1977) show that the Rhyolite Canyon Formation tuff (25.5 ± 0.6 Ma) is distinctly younger than underlying rhyolites of the Faraway Ranch Formation (28.6 ± 2.0 Ma; 28.3 ± 0.8 Ma) but overlaps with ages (25.1 ± 1.2 Ma; 26.3 ± 0.8 Ma) of stratigraphically older ash-flow tuffs in the eastern Chiricahua Mountains. Ash-flow tuff eruption, caldera formation, and porphyry intrusion at Turkey Creek are constrained to a period of less than 1 million years by a biotite K–Ar age of 25.4 ± 0.7 Ma on a rhyolite dike that intrudes the porphyry.

Drewes and Williams (1973) produced a 1:62,500 scale map of the east-central part of the caldera as part of their study of the Chiricahua Wilderness, and the outflow stratigraphy of the Rhyolite Canyon Formation has been revised and mapped at 1:24,000 scale by Drewes (1982) and Latta (1983). In addition, Latta (1983) mapped a transect from the outflow sequence in the National Monument through the moat of the caldera and into the central intrusion. He noted an up-section decrease in the dips of moat rhyolites and suggested that resurgent doming began before and continued after eruption of these rocks. Latta also defined informal members of the Rhyolite Canyon Formation, correlated the uppermost ash-flow member of the formation outside the caldera with the intracaldera tuff, and argued that 60–70% of the main eruptive sequence was ponded in the caldera. Latta noted that the thickest outflow-tuff sections derived from the Turkey Creek caldera (Fig. 3, Monument member) are about 430 m, but the intracaldera tuff is 1.2 to 1.5 km thick in the northern part of the caldera, prima fascia evidence for collapse. On the basis of reconnaissance geochemistry, he described compositional zoning similar to that in the Bishop Tuff and interpreted the main eruptive sequence as the product of a single compositionally zoned magma chamber.

This guide is a preliminary account of the geology of the Turkey Creek caldera. It is based on our first two seasons of geologic mapping and on our initial interpretations of petrographic and geochemical data. Because this is an ongoing project, we expect our interpretations to evolve as we continue mapping and as we apply new analytical, geochronologic, and geophysical techniques to the Turkey Creek rocks. Accordingly, we advise the reader that we intend to explore working models during the field trip in addition to reviewing models proposed by earlier workers; we anticipate that some of our ideas will be controversial and that alternative interpretations will develop during the trip.

Day 1,
Part 1. Willcox to Chiricahua National Monument: Outflow tuff and "basement" rocks

The largest erosional remnant of the outflow tuff from Turkey Creek caldera is exposed north of the caldera in Chiricahua National Monument. This area probably represents a paleobasin where outflow tuff ponded adjacent to highlands to the north and east (Marjaniemi, 1969). Three different stratigraphic divisions have been proposed for the ash-flow tuffs and associated rocks of the Rhyolite Canyon Formation exposed outside the caldera in the National Monument (Enlows, 1955; Drewes, 1982; Latta, 1983). The type

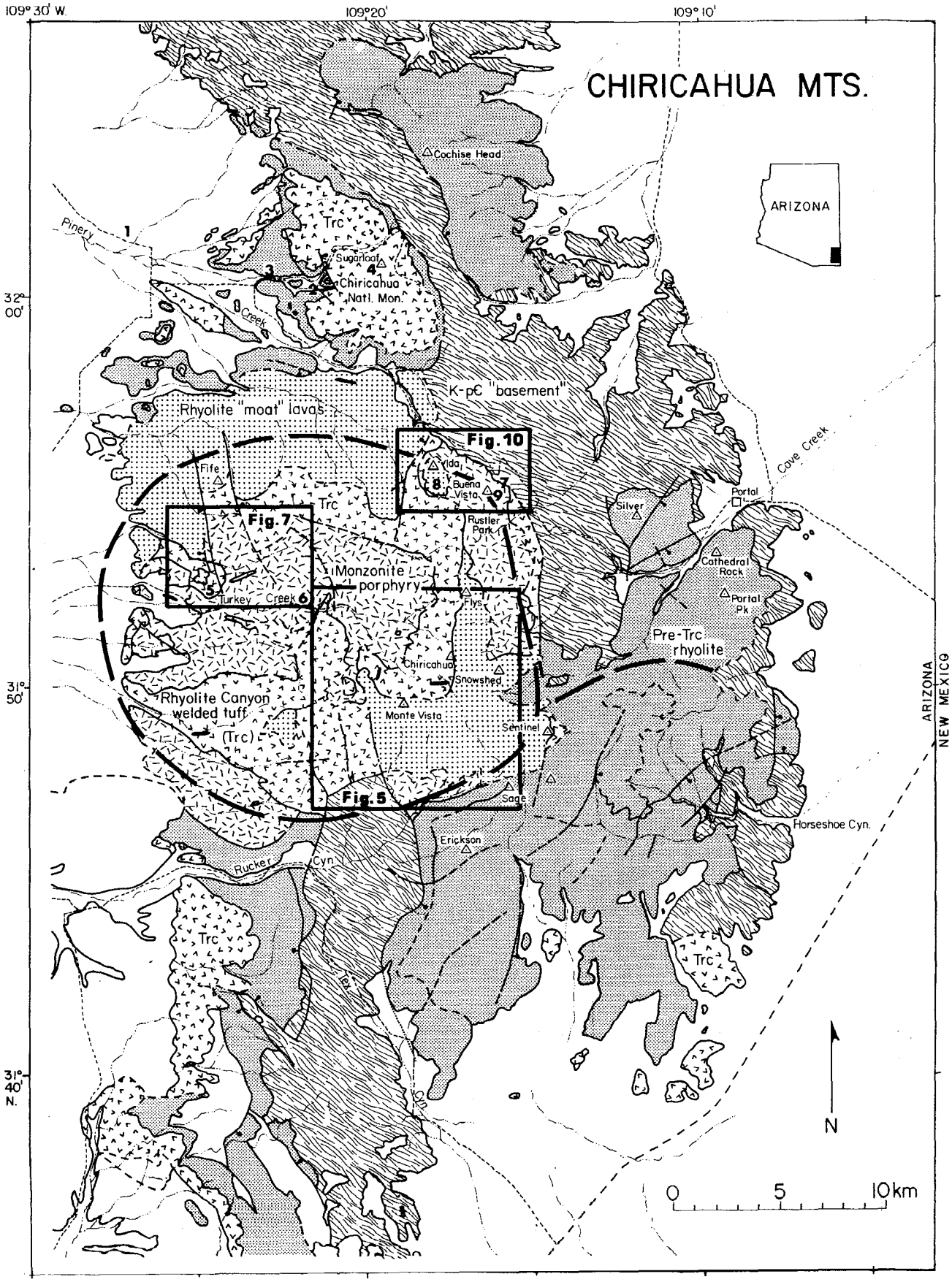

FIGURE 1 Geologic index map of the Chiricahua Mountains (after Marjaniemi, 1969), showing field-trip localities (by number) and areas of more detailed map figures. Trc = welded tuff of Rhyolite Canyon Formation; K–pC = Cretaceous to Precambrian rocks. Approximate structural boundary of the Turkey Creek caldera and northwest boundary of the Portal caldera indicated by heavy lines.

section of Enlows (1955) is between Rhyolite and Bonita Canyons (east-northeast of the visitor center) where the greatest thickness (≥400 m) of the formation is exposed (see Fig. 2 and map by Drewes, 1982). Here, Enlows defined eight informal rhyolitic tuff members, capped by a dacite lava member (an erosional remnant recognized only atop Sugarloaf Mountain). Drewes (1982) mapped seven pyroclastic map units below the capping lava; he discriminated these units mainly on the basis of variation in welding and crystal content.

In contrast, Latta (1983) considered the Rhyolite Canyon Formation outflow to contain a lower Jesse James Canyon ash-flow member that is petrographically and chemically distinct from the overlying informal Monument member. He defined the Monument member as the outflow sequence of the Turkey Creek caldera, a composite ash-flow sheet with only three principal cooling units; the source caldera for the Jesse James Canyon member is uncertain. A comparison of the stratigraphic nomenclature is shown in Fig. 3. For the purposes of this guide, we prefer the genetic divisions of Latta, and we use his "units I, II, and III" for the lower, middle, and upper cooling units of the Monument member. The three units correspond approximately to Drewes' units Trls, Trus, and Trat+Truw, respectively (Fig. 3 and Drewes, 1982).

Latta recognized a cooling break within the intracaldera tuff, and, on the basis of major-element chemistry, he correlated the *lower* cooling unit of the intracaldera sequence with his *upper* cooling unit of the outflow tuff (Monument member, unit III) (Figs. 3, 4), leaving correlation of the upper unit of the intracaldera tuff and the two lower cooling units of the outflow tuff in question. He suggested that the later part of the main eruptive sequence (upper cooling unit of intracaldera tuff) ponded in the caldera and that the outflow sequence includes units erupted before and after caldera collapse. The lower cooling units of the outflow tuff may have erupted during the initial stages of caldera formation, prior to significant collapse, and accordingly are not preserved inside the caldera; alternatively, they may exist in the subsurface, below a central monzonite porphyry intrusion (see discussion).

We also note the chemical similarity of the upper cooling unit of the outflow sequence with the intracaldera tuff. Although there is considerable variation in the alkalis and rubidium, the more immobile elements show good agreement between the two units (Table 1).

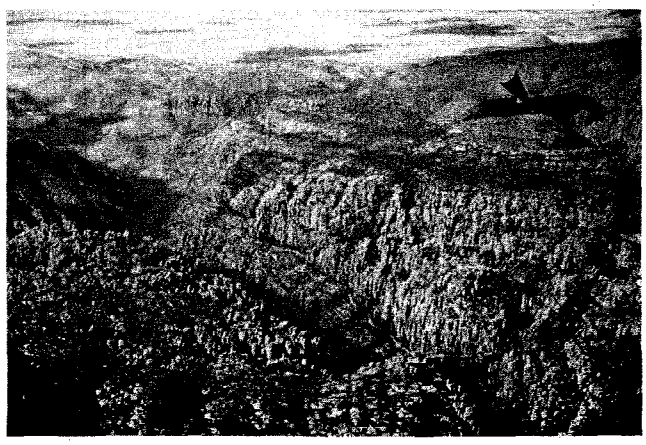

FIGURE 2—Oblique aerial photograph of Rhyolite Canyon Formation in Chiricahua National Monument. View is to northwest down Rhyolite Canyon drainage. Sugarloaf Mountain (at arrowhead) is dacite lava that caps outflow welded tuff from Turkey Creek caldera.

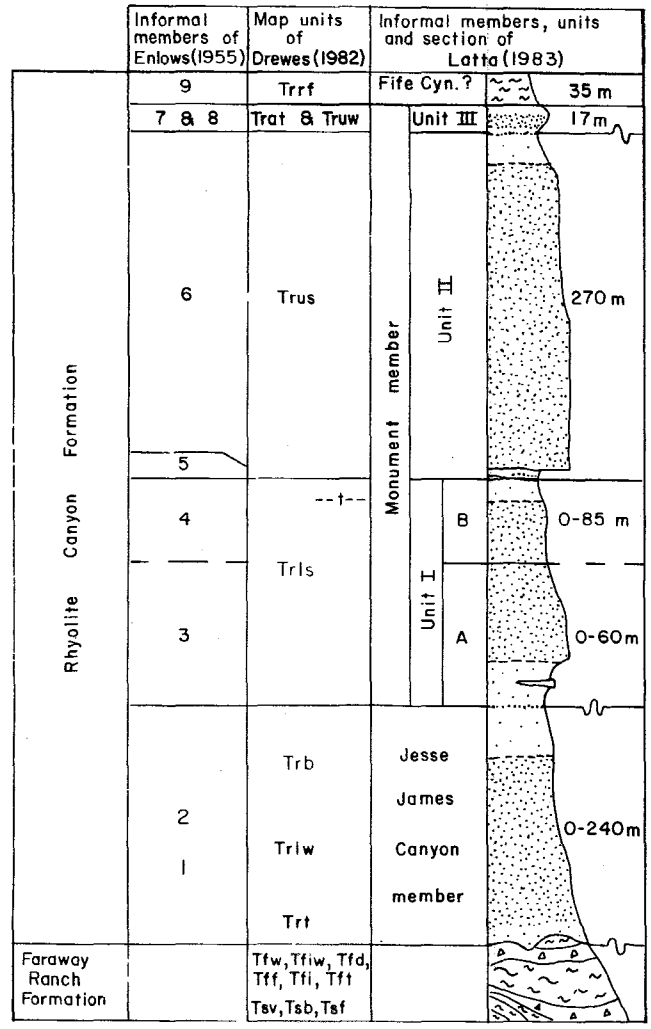

FIGURE 3—Correlation chart for stratigraphic units of the Rhyolite Canyon Formation. Colored map by Drewes (1982), provided with field-trip material, is also available at National Monument Visitor Center.

Dacite lava overlying the ash-flow sequence in the National Monument (dacite of Sugarloaf Mountain) is chemically and petrographically similar to porphyry of the ring intrusion and to the earliest lavas erupted from the ring intrusion of the caldera at Barfoot Peak (Table 1; locality is near Ida Peak in Fig. 1). Because of the lack of vent structures closer to Sugarloaf Mountain and the similarity in chemistry and petrography, a ring-dike source, about 8 km south, is suggested.

Mileage

0.0 **Begin road log: Downtown Willcox,** Arizona, corner of Haskell (Business I-10) and Maley (AZ-186) streets. **Drive east on Maley** (AZ-186) for 31.5 mi to AZ-181, then **east** on AZ-181 for an additional 3.1 mi to Chiricahua National Monument. **29.8**

29.8 **STOP 1. Overview of outflow tuff of the Rhyolite Canyon Formation and northern margin of Turkey Creek caldera.** Brief "arm-waving" stop (best with late-afternoon light). Cone-shaped hilltop (Sugarloaf Mountain) on horizon at 11:00 is dacite lava

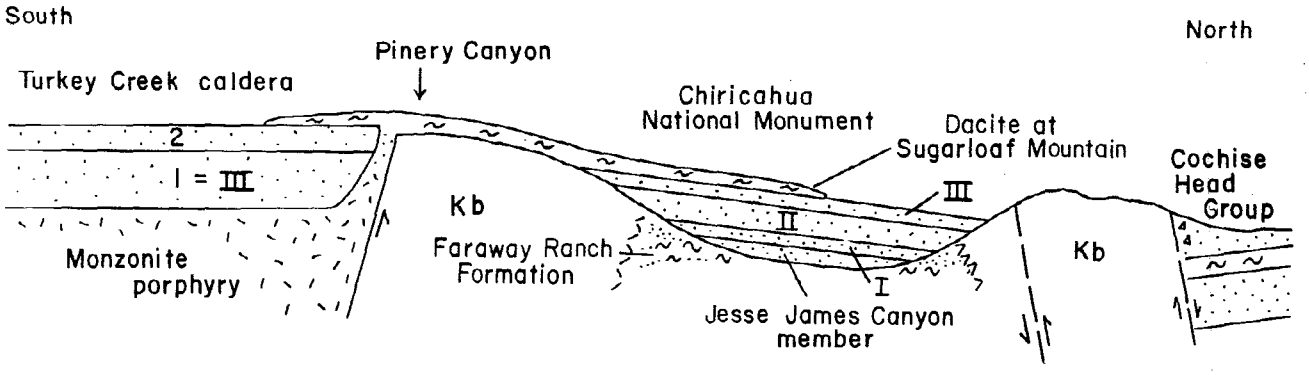

FIGURE 4—Cartoon showing correlation of lower part of the intracaldera tuff of Rhyolite Canyon Formation (1) with upper cooling unit of outflow sequence (III) (as suggested by Latta, 1983). Topography now partly inverted; uplifted Bisbee Group (Kb) now underlies valleys (e.g., Pinery Canyon). The Jesse James Canyon member and units I, II, and III are informal divisions of the Rhyolite Canyon Formation (see Fig. 3). The informal Cochise Head Group of Latta (1983) includes welded tuffs mapped as part of the rhyolite of Rough Mountain by Drewes (1982).

capping outflow Rhyolite Canyon Formation tuff. Low-angle outflow tuff sheet dips to south away from high ground to north, flattens below Sugarloaf Mountain, and climbs to south toward the caldera margin. Outflow tuff overlies rhyolite lavas and pyroclastic flows of Faraway Ranch Formation (low hills in foreground). Topographic margin of the caldera follows Pinery Canyon at 1:00; high terrain on horizon to southeast follows eastern ring intrusion of the caldera. **1.7**

31.5 Intersect AZ-181. **Turn left** (east) on AZ-181. **3.0**

34.5 Junction with Pinery Canyon Road. **Curve left** (stay on **pavement and enter Chiricahua National Monument**). Note flow-banded rhyolite flow-dome of Faraway Ranch Formation in hill immediately ahead. **1.7**

TABLE 1—Major-element analyses (normalized to 100% by weight, volatile-free), CIPW norms and trace-element abundances (in ppm) for igneous rocks of the Chiricahua Mountains, southeast Arizona. Averages and standard deviations given for "n" analyses of each map unit. LOI = loss on ignition. Molar FeO/FeO + Fe_2O_3 set to 0.8 prior to calculation of norms. Trc = Rhyolite Canyon Formation; Tmp = monzonite porphyry. [1]An informal unit.

				Trc (outflow)				
Unit:	Faraway Ranch Fm. lavas	Jesse James Cyn. tuff[1]	Trc intracaldera	I	II	III	Transitional Tmp-Trc	Transitional Tmp-lava
n	2	5	15	6	12	3	10	4
SiO_2	73.39±0.05	77.60±0.22	76.45±1.08	77.38±0.23	77.58±0.21	75.99±0.26	75.60±2.49	65.95±0.84
Al_2O_3	14.95±0.10	12.36±0.19	12.38±0.60	12.06±0.08	12.09±0.11	12.47±0.03	12.66±0.85	15.55±0.16
Fe_2O_3	0.25±0.01	0.20±0.02	0.40±0.04	0.32±0.01	0.30±0.02	0.41±0.01	0.40±0.15	0.93±0.06
FeO	0.89±0.01	0.73±0.08	1.44±0.16	1.16±0.03	1.09±0.08	1.47±0.02	1.44±0.54	3.36±0.20
MgO	0.26±0.01	0.32±0.08	0.19±0.09	0.08±0.09	0.06±0.09	0.30±0.25	0.31±0.20	1.64±0.31
CaO	1.22±0.05	0.39±0.12	0.24±0.12	0.24±0.19	0.25±0.07	0.30±0.01	0.40±0.40	3.48±0.34
Na_2O	3.92±0.09	3.31±0.18	2.84±0.97	3.67±0.15	3.47±0.14	3.48±0.42	2.65±1.30	3.83±0.53
K_2O	4.89±0.14	4.88±0.08	5.79±1.05	4.91±0.04	4.96±0.08	5.30±0.15	6.19±1.55	4.10±0.70
TiO_2	0.18±0.01	0.14±0.01	0.23±0.03	0.11±0.00	0.12±0.02	0.21±0.01	0.27±0.17	0.78±0.07
P_2O_5	<0.05	<0.05	<0.05	<0.05	<0.05	0.05±0.0	0.05±0.08	0.30±0.02
MnO	0.05±0.0	0.05±0.01	0.03±0.02	0.07±0.01	0.06±0.02	0.07±0.01	0.04±0.03	0.09±0.01
LOI	3.41±0.30	1.56±0.38	1.20±0.6	0.59±0.30	0.69±0.28	0.98±0.92	1.40±1.35	1.89±1.14
Q	28.31	37.86	36.07	35.77	37.01	33.40	34.44	17.43
C	0.98	0.92	1.01	0.26	0.56	0.45	0.99	0.0
or	28.87	28.84	34.23	29.02	29.32	31.29	36.55	24.23
ab	33.18	28.04	24.05	31.08	29.38	29.47	22.44	32.43
an	6.07	1.94	1.14	1.21	1.24	1.50	1.66	13.10
di	0.00	0.00	0.00	0.00	0.00	0.00	0.00	1.84
hy	1.88	1.84	2.47	1.99	1.83	2.88	2.71	7.45
mt	0.36	0.30	0.58	0.47	0.44	0.59	0.58	1.35
il	0.35	0.27	0.44	0.21	0.23	0.41	0.51	1.48
ap	0.00	0.00	0.00	0.00	0.00	0.00	0.12	0.70
n	4	5	22	14	15	4	10	8
Rb	175±11	304±10	336±115	425±14	381±34	294± 3	406±116	221±91
Sr	250±22	28± 6	34± 11	20± 5	23± 7	36± 6	62± 44	306±64
Y	25± 3	43± 4	60± 8	72±21	74±20	66± 1	61± 12	46± 5
Zr	162± 4	166± 4	407± 72	291±11	279± 9	381±43	324± 78	442±88
Nb	15± 3	35± 4	43± 5	63± 3	57± 5	46± 1	48± 13	25± 3
Ba	841± 29	21± 9	70± 25	17± 9	28±18	68± 9	192±195	806±64
La	51± 3	40± 6	110± 26	58±16	61±20	106±10	68± 17	75±13
Ce	91± 6	79±10	204± 43	131±20	136±17	206±25	133± 20	139±23
Nd	40± 7	29± 4	83± 16	50±12	56±18	77± 8	60± 11	68± 9

(Table 1, continued)

	Monzonite porphyry		Moat rhyolite							
Unit	East ring	Core	Upper	Lower	Other	Moat tuffs	201533 Sugarloaf	86P-31 Barfoot	86P-71 Ida Pk.	86P-73 Ida Pk.
n	9	5	8	7	4	3	dacite	dacite	aphy. rhy.	qz. rhy.
SiO_2	64.86±0.92	65.78±3.42	77.44±0.62	76.79±1.18	74.70±2.15	77.70±0.42	65.21	66.29	76.06	76.41
Al_2O_3	15.68±0.26	15.29±0.57	12.66±0.35	12.76±0.52	13.59±1.12	12.24±0.31	15.72	15.45	13.37	12.98
Fe_2O_3	0.96±0.05	0.97±0.27	0.21±0.01	0.27±0.01	0.38±0.02	0.22±0.01	0.98	0.93	0.22	0.28
FeO	3.47±0.17	3.48±0.98	0.77±0.04	0.96±0.05	1.36±0.07	0.79±0.04	3.53	3.35	0.81	0.99
MgO	1.53±0.17	1.48±0.58	0.08±0.06	0.15±0.07	0.48±0.11	0.15±0.02	1.90	1.57	0.0	0.16
CaO	3.12±0.49	2.81±1.08	0.23±0.22	0.64±0.19	1.42±0.33	0.25±0.06	3.76	3.52	0.11	0.64
Na_2O	3.87±0.28	3.68±0.22	3.75±0.48	3.73±0.54	2.92±0.83	3.44±0.02	3.37	4.54	3.76	3.83
K_2O	5.14±0.45	5.14±0.71	4.67±0.89	4.47±0.62	4.79±0.77	5.01±0.09	4.40	3.06	5.46	4.48
TiO_2	0.93±0.05	0.96±0.28	0.15±0.03	0.18±0.01	0.27±0.02	0.15±0.01	0.77	0.88	0.16	0.18
P_2O_5	0.35±0.03	0.32±0.12	<0.05	<0.05	0.06±0.04	<0.05	0.30	0.31	<0.05	<0.05
MnO	0.10±0.02	0.10±0.03	0.06±0.02	0.05±0.01	0.03±0.02	0.04±0.02	0.08	0.10	0.04	0.05
LOI	2.17±0.62	1.67±0.11	1.74±2.28	4.07±1.39	2.80±1.40	0.51±0.10	1.74	3.34	0.50	5.02
Q	13.43	15.89	36.68	35.74	34.98	37.23	17.09	17.88	32.56	34.74
C	0.00	0.00	1.03	0.61	1.16	0.70	0.00	0.00	1.08	0.67
or	30.36	30.37	27.59	26.43	28.33	29.63	25.99	18.07	32.27	26.47
ab	32.73	31.10	31.70	31.59	24.67	29.12	28.49	38.42	31.79	32.42
an	10.26	10.05	1.12	3.20	6.65	1.24	14.77	12.74	0.56	3.17
di	2.46	1.47	0.00	0.00	0.00	0.00	1.59	2.21	0.00	0.00
hy	6.81	7.16	1.30	1.71	3.01	1.47	8.51	6.93	1.11	1.79
mt	1.40	1.40	0.31	0.39	0.55	0.32	1.42	1.35	0.33	0.40
il	1.76	1.81	0.28	0.34	0.51	0.29	1.45	1.67	0.31	0.34
ap	0.82	0.76	0.00	0.00	0.15	0.00	0.70	0.74	0.00	0.00
n	22	9	12	11	5	8	1	1	1	1
Rb	203±49	211±58	455±114	404±98	248±30	352±47	174	189	403	422
Sr	227±28	222±56	25± 23	39±19	174±51	25± 7	381	382	15	91
Y	48± 5	48± 5	49± 15	56±14	38± 6	52±10	39	45	43	68
Zr	526±57	481±20	193± 8	211±22	171±14	206±22	335	514	201	228
Nb	26± 2	26± 2	53± 10	41±10	13± 4	48± 7	21	25	49	40
Ba	709±66	712±90	10± 4	77±10	691±83	52±31	856	727	6	82
La	83± 7	89±13	33± 9	72±11	52± 5	50±13	60	86	38	79
Ce	150±11	164±18	84± 15	136±30	105±14	107±24	114	168	78	160
Nd	73± 5	73± 7	30± 9	60±15	53± 7	43± 9	57	77	29	68

36.2 Pass pullout on left. We will return here for Stop 3. **1.3**

37.5 **STOP 2. National Monument Visitor Center** (restrooms). Backtrack 0.55 mi down canyon to west for Stop 3. **0.5**

38.0 **STOP 3. Faraway Ranch Formation**—"Basement rhyolites." Pull off on right (north) just before boulders. This is a **blind curve,** so **watch out for traffic! Climb to top of hill north of road.** This stop is in the eroded upper carapace breccia of a rhyolite (72% SiO_2, Table 1) lava within the Faraway Ranch Formation (shown as Tff on the geologic map by Drewes, 1982). Much of the outcrop is devitrified, but glassy zones are preserved near the cliff at the north edge of the outcrop. Note the presence of biotite and sphene; these minerals (and hornblende) are common in the rhyolites and dacites that predate the Turkey Creek caldera, but they are rare in the ash-flow tuffs that were derived from the caldera (the Monument member of the Rhyolite Canyon Formation). Biotite from similar rhyolite on Erickson Ridge (S30W, ~1/2 mi) was dated at 28.2±0.8 Ma by Marjaniemi (1969).

An unfaulted section through the overlying Rhyolite Canyon Formation is visible at Riggs Mountain (N40E, ~1/2 mi). The base of the prominent nose extending south from Riggs Mountain is underlain by Faraway Ranch Formation rhyolite carapace breccia similar to that exposed here (shown as Tsv by Drewes, 1982). The carapace breccia is overlain by a pyroclastic flow and airfall tuff (Trt), then by a salmon-colored, biotite-bearing, welded tuff (Trb). These tuffs (Trt and Trb) are mapped as the informal Jesse James Canyon member of the Rhyolite Canyon Formation by Latta (1983), who considers it to be a single cooling unit, distinct from overlying ash flows derived from the Turkey Creek caldera (Latta's informal Monument member). The Jesse James Canyon member is overlain by unit I of the Monument member (Trls), then by the prominent cliff-forming unit II of the Monument member (Trus).

We found that each of the map units below unit I of the Monument member (Trt, Trlw, Trb) is characterized by relatively low Rb and Zr (~300 and ~170 ppm, respectively) compared to higher Rb and Zr (~400 and ~290 ppm) in units I and II of the Monument member (Table 1). We believe that this geochemical and cooling break may be the most genetically significant contact in the section, possibly separating ash flows derived from two separate calderas; however, additional work is needed before suggesting stratigraphic revision.

Continue west (down canyon) 0.5 mi to Faraway Ranch entrance. **Turn around** here and **proceed back up canyon to east. 1.7**

39.7 **Curve left** (north) at Visitor Center and **drive up Bonita Canyon.** Road climbs from Faraway Ranch Formation through unit I of the Monument member

(within 1 mi) and remains in unit II for most of way to Stop 4. Hoodoos are in unit II. **0.6**

40.3 Pass campground entrance on left. **1.8**

42.1 35 cm thick welded tuff (on right). This thin ash flow occurs at the base of unit II and preserves a complete welding profile through a thickness of only 35 cm. If time permits, we will stop for a closer inspection after lunch. **1.3**

43.4 "Ancient lake beds." Oligocene(?) shales and sandstones underlying Rhyolite Canyon Formation along the east side of the paleobasin in which the outflow sequence accumulated. **1.7**

45.1 Sugarloaf/Echo Canyon Road intersection. **Turn right** (west). **0.1**

45.2 **Pass Echo Canyon parking lot. 0.5**

45.7 **STOP 4. Rhyolite Canyon Formation**—Outflow sequence. **Hike up Sugarloaf trail to lookout** (~2 hours, round trip). **Bring lunch** and camera. Localities given relative to parking lot elevation of 6820 ft, see map by Drewes (1982). Trail begins in uppermost part of unit II of the Monument member (Fig. 3).

6830 ft. Map contact between Drewes' Trus (densely welded tuff) and Trat (air-fall tuff) map units. Latta includes both in his unit II. Outcrops above and below the mapped contact contain abundant large pumices, a characteristic of unit II in this area, and have similar trace-element chemistry (Table 1). We locate the contact between units II and III at the welding break farther up-section (near 6960 ft elevation on trail—see below), on the basis of an abrupt decrease in abundance of pumice and lithic fragments, a decrease in welding, and a change to less evolved chemistry.

6960–7000 ft. Weakly indurated, moderately to weakly welded tuff with surge beds. Undercut exposure at base of densely welded zone of unit III of the Monument member (Fig. 3). Exposure at far (west) end of undercut reveals 0–20 cm thick cross-laminated (dune-form) surge bed. Laminated bed is apparent source region for Liesegang bands that crosscut laminations and extend upward into the overlying tuff. Directly above is a fines-depleted pipe that may represent a fossil fumarole. Similar fines-depleted pipes and irregular veins are exposed throughout this area in both the poorly indurated basal zone of unit III and extending into the overlying densely welded zone.

7120 ft. Contact between unit III of the Monument member tuff and overlying dacite lava flow, Sugarloaf dacite (Trrf), exposed from here to top. As noted previously, the chemical composition of the lava is similar to dacite and monzonite porphyry from the caldera ring intrusion near Barfoot Peak (Table 1). Note that the dacite contains large (to 0.5 cm) feldspar phenocrysts and fine-grained mafic xenoliths. Remember these features for comparison with the ring intrusion and related lavas (to be seen tomorrow).

7310 ft. **Lunch!** Lookout post at top of Sugarloaf Mountain. Building is constructed from glassy dacite prophyry lava. The lookout provides an excellent view of Cochise Head (to the northeast), part of a thick accumulation of rhyolitic welded tuff and tuff breccia east of the Apache Pass fault that apparently overlaps in age with the Faraway Ranch Formation.

The high terrain forming the skyline to the southeast is supported by the eastern ring intrusion that defines the structural margin of the Turkey Creek caldera. Ida and Barfoot Peaks (Figs. 1, 10a) are visible in the middle ground. Ida Peak is capped by rhyolite moat lavas that overlie the most northwesterly exposures of the ring intrusion. Barfoot Peak is capped by dacite lava very similar to that underfoot and preserves rocks that are transitional into the ring-intrusion porphyry.

Pinery Canyon, the principal east–west-trending drainage to the south, follows the former northern topographic margin of the caldera. The morphology of the caldera is partly inverted due to erosion of the less resistant Bisbee Group sedimentary rocks outside the structural margin. We will drive up Pinery Canyon and across the pass at its head tomorrow morning, en-route to exposures of the ring intrusion on the south side of Barfoot and Ida Peaks.

Return to cars and **backtrack out of National Monument** to intersection of AZ-186 and AZ-181 (12 mi). **ROAD-LOG MILEAGE STARTS OVER AT THIS INTERSECTION.** If time permits, we will **stop briefly** at the 35 cm thick welded tuff **on our way out of the Monument** (at **mileage 49.3,** 3.6 mi from here). For future users of this guide who wish to spend additional time in the National Monument, Massai Point (1.5 km southeast of Sugarloaf Mountain) provides spectacular views of eroded columns in welded tuff of the Rhyolite Canyon Formation.

Part 2. AZ-181/AZ-186 intersection to Turkey Creek: Central intrusion, intracaldera tuff, and moat rhyolites

From the AZ-181/AZ-186 intersection we drive south on AZ-181 for 10.5 mi, then east on a gravel road into the core of the Turkey Creek caldera (Fig. 1). The core of the caldera is deeply eroded ($\geq$2 km), exposing hypabyssal levels of a monzonite to quartz monzonite porphyry intrusion over an area of about 40 km^2. Outcrop pattern, as well as similarity in petrography and chemistry, suggest that the intrusion is continuous in the subsurface with a monzonite to dacite ring intrusion that is discontinuously exposed around more than 180° of the caldera circumference. Note that ring and central phases of the monzonite are separated by a segment of intracaldera tuff only about 1 km wide in the southwest (Fig. 1).

Marjaniemi (1969) referred to the central phase of the monzonite porphyry as the "dome monzonite." Both Marjaniemi and Latta (1983) related resurgence of the caldera to intrusion of the porphyry, and Marjaniemi pointed out that intrusion is bracketed closely in time by eruption of the overlying Rhyolite Canyon Formation tuff (25.5 ± 0.6 Ma) and by a K–Ar biotite age of 25.4 ± 0.7 Ma on a rhyolite dike that intrudes the porphyry. Latta noted angular discordance between radial dips away from the center of the caldera of about 25° for the intracaldera Rhyolite Canyon Formation tuff and about 15° for lower moat rhyolites, as well as a further decrease in dip of units higher in the moat sequence. On this basis, he proposed that resurgence began

shortly after caldera collapse, but continued during moat lava eruption. However, sedimentary rocks in the caldera record a significant erosional/depositional hiatus prior to eruption of the high-silica rhyolite moat lavas.

Thick sections of volcaniclastic breccias (mainly lahars) and tuffaceous sandstones in the southeastern part of the caldera (Fig. 5) contain clasts of Rhyolite Canyon Formation tuff and monzonite porphyry. These sedimentary rocks were deposited on an erosional surface that cuts through the tuff and into the porphyry, and they are overlain by rhyolite moat lavas. We believe that porphyry in the core of the caldera was uplifted; but, we are not convinced that resurgent *intrusion* of the porphyry magma was the cause of uplift; later intrusion of moat rhyolite magma may also have caused uplift (see discussion and Fig. 12a). Because of the presence of monzonite clasts in moat sediments, the por-

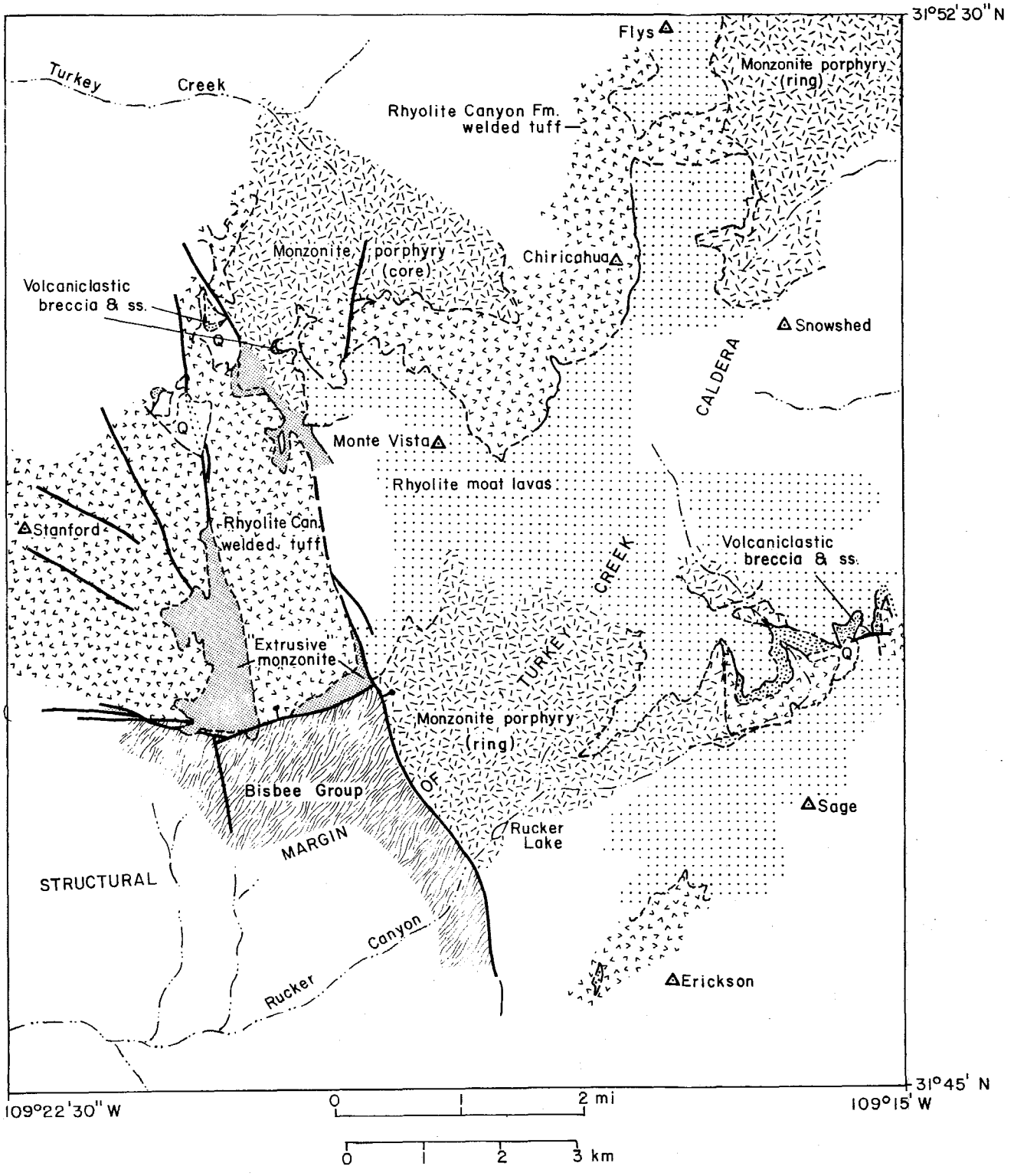

FIGURE 5—Preliminary geologic map of the southeastern part of the Turkey Creek caldera showing thick sequence of volcaniclastic and sedimentary rocks deposited unconformably on Rhyolite Canyon Formation tuff and on both the central and ring phases of the monzonite porphyry. Extrusive equivalents of the monzonite occur within the caldera along fault zones (see text). Q = Quaternary deposits.

phyry was probably already emplaced at its present stratigraphic level during at least the latest stages of uplift. As explained below, it is locally gradational with the Rhyolite Canyon Formation tuff and probably represents either the in-situ or reintruded residue of the source magma chamber for the tuff.

The monzonite intrusion (central and ring phases) is exposed at a hypabyssal level; it is porphyritic, with large (0.5 to several cm) andesine phenocrysts in a granophyric groundmass. Fresh samples from relatively deep exposures are magnetite–clinopyroxene–hornblende–biotite-bearing monzonite to quartz monzonite. Small (1–2 cm) mafic hornfels inclusions are a sparse but characteristic feature of both the central and the ring intrusions.

Although most of the monzonite is non-foliated porphyritic granophyre, abrupt transitions in texture, petrography, and chemistry occur within both the central and ring intrusions. We will visit a locality tomorrow atop the ring intrusion where quartz monzonite porphyry grades into and feeds porphyritic dacite lava flows. Similar relations are also observed along faults in the southern part of the central intrusion, where transitions from homogeneous quartz monzonite porphyry, through miarolitic porphyry, to vesicular, quartz-bearing, porphyritic lava occur over a few meters. The lavas are flow-folded but appear gradational with densely welded intracaldera tuff of the Rhyolite Canyon formation. These zones of extrusive porphyry (Fig. 5) bound fault blocks in the intracaldera tuff, indicating eruption from vents that formed as the floor of the caldera (roof of the magma chamber) was broken up during late stages of caldera collapse.

Chemical data for the Rhyolite Canyon Formation tuff and for the hypabyssal quartz monzonite porphyry (Table 1, Fig. 6) document the change to a less siliceous (monzonitic) magma. Central and ring vents for the ash-flow tuff were intruded and then clogged by this viscous magma. The abrupt transition from high-silica ash-flow tuff to quartz-bearing dacite lava and then to quartz monzonite and monzonite porphyry suggests that high-silica rhyolite was evacuated from a source chamber in which a distinct compositional interface existed between high-silica rhyolite and underlying low-silica monzonitic magma.

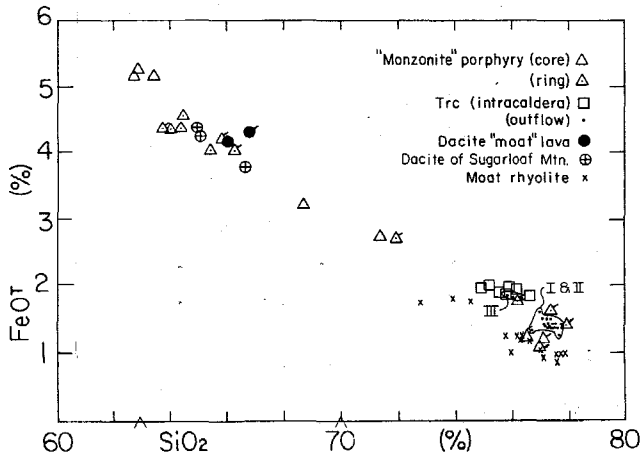

FIGURE 6—SiO_2–FeO^T variation diagram comparing monzonite porphyry and transitional intrusive–extrusive rocks of core and ring intrusions to dacite and rhyolite moat lavas and Rhyolite Canyon Formation tuff (Trc). Symbols with tick-marks are texturally transitional between intrusion and lava flow.

In lower Turkey Creek canyon (Fig. 7; Stop 5) we will investigate the contact between the central intrusion and the overlying intracaldera Rhyolite Canyon Formation tuff. In this area, the upper contact of the central intrusion is a monolithologic roof breccia composed of disaggregated monzonite porphyry and quartz-phyric granophyre. Brecciation could have been produced by magmatic inflation and/or caldera collapse, perhaps coupled with intrusion of the central phase of the porphyry as a laccolith within, or at the base of, the intracaldera tuff. But, the lack of megascopic shear fabric is difficult to reconcile with a purely tectonic interpretation.

The breccia is strongly altered and hematized or sericitized. Brecciation may have been hydrothermal, produced by hydrofracturing during devolatilization of the porphyry intrusion. Another possibility is that the roof breccia is analogous to the crush zone in nuclear blast craters (e.g., Derlich, 1970), or to breccias which occur at the borders of bolide impact craters (e.g., Pohl et al., 1977; Stöffler et al., 1979). Our preliminary investigations suggest low-pressure shock metamorphism. A possible interpretation is that magmatic explosion(s) with foci in the underlying core intrusion created shock waves that brecciated the chilled border of the intrusion. Eruption of Rhyolite Canyon Formation tuff may have evacuated the upper siliceous part of the magma chamber during caldera collapse, such that monzonite from low in the chamber was drawn up into contact with the quartz-bearing (siliceous) breccia. Alternatively, brecciation may be related to magmatic inflation and/or caldera collapse; perhaps coupled with intrusion of the central monzonite as a laccolith within the intracaldera tuff.

Merits of the various explanations will be discussed at the outcrop. Recent mapping of the Rhyolite Canyon/porphyry contact to the northeast has revealed complex field relations. Dikes and sills of rhyolite and granite occur near the contact and intrude both the overlying tuff and the underlying monzonite. Monzonite porphyry dikes also locally intrude the overlying tuff. The concentration of rhyolite and granite dikes and sills near the contact suggests a possible origin by melting of intracaldera tuff by the porphyry. Some breccia outcrops contain pyroclastic-matrix breccias with clasts of precaldera(?) dacite; other breccias contain plastically deformed clasts. However, brecciated joint-blocks of porphyry are observed near Turkey Creek. These relations indicate that although some of the porphyry (deeper levels?) was probably still at super-solidus temperatures during formation of the roof breccia, other regions were cooled and jointed prior to fragmentation. Our recent field work favors an intrusive contact between the porphyry and the tuff, but the process(es) that led to brecciation have yet to be established.

Mileage

0.0 Intersection of AZ-181 and AZ-186, west of Chiricahua National Monument. **Turn left** and drive south on AZ-181. **10.5**

10.5 Right-angle curve in road at **intersection with Turkey Creek Road. Turn left** (east) onto gravel Turkey Creek Road. **2.7**

13.2 Contact between intracaldera tuff and central monzonite intrusion trends up valley between two low hills at 3:00. **2.5**

15.7 **STOP 5. Roof breccia of core intrusion, intracaldera Rhyolite Canyon Formation tuff, moat**

rhyolites. Park on left where road widens. Assemble on exfoliation surface on right (south) side of road. This is a typical porphyritic monzonite of the core intrusion. We will climb fence on north side of road, hike across field, and climb ridge to north. Duration: ~2 hrs.

FUTURE GUIDEBOOK USERS: DO NOT CLIMB FENCE WITHOUT PERMISSION OF RANCHER (THIS LAND IS POSTED—NO TRESPASSING).

A simplified geologic map and cross section of the traverse we will make is given in Fig. 7. We climb through a section, within a graben block, that takes us from monzonite porphyry of the central intrusion through roof breccia and into intracaldera Rhyolite Canyon Formation tuff. The tuff is overlain by bedded volcaniclastic breccia and sandstone, then by moat rhyolite. It is possible to see all these units in a relatively short distance because the intracaldera tuff is anomalously thin (400–500 m), at least in part due to erosion. Magmatic excavation of the basal intracaldera tuff provides an alternative means to thin the section; however, we have not observed inclusions of the tuff in the porphyry, and a similar roof breccia is exposed below a much greater thickness (~1 km) of intracaldera tuff to the northeast (Fig. 7).

The porphyry is locally fractured and a few quartz veins can be found in outcrops along Turkey Creek (we cross the creek en-route to the base of the section). A zone of monzonite to quartz-phyric granophyre breccia is exposed at the base of the section. This is a monolithologic, cataclastic, autobreccia that is composed of decimeter-to-millimeter-scale clasts of monzonite and granite granophyre porphyry in a granulated matrix (mainly clast-supported). Veins of hematitic, matrix-supported breccia are locally exposed and indicate limited fluidization. Thin sections reveal that clasts are cut by thin (<1 mm) mylonite bands and microfaults and that quartz phenocrysts are shattered (Fig. 8).

The lower "crush" zone of the breccia contains clasts of granophyric monzonite porphyry; clasts in the upper "fracture" zone are quartz-phyric gran-

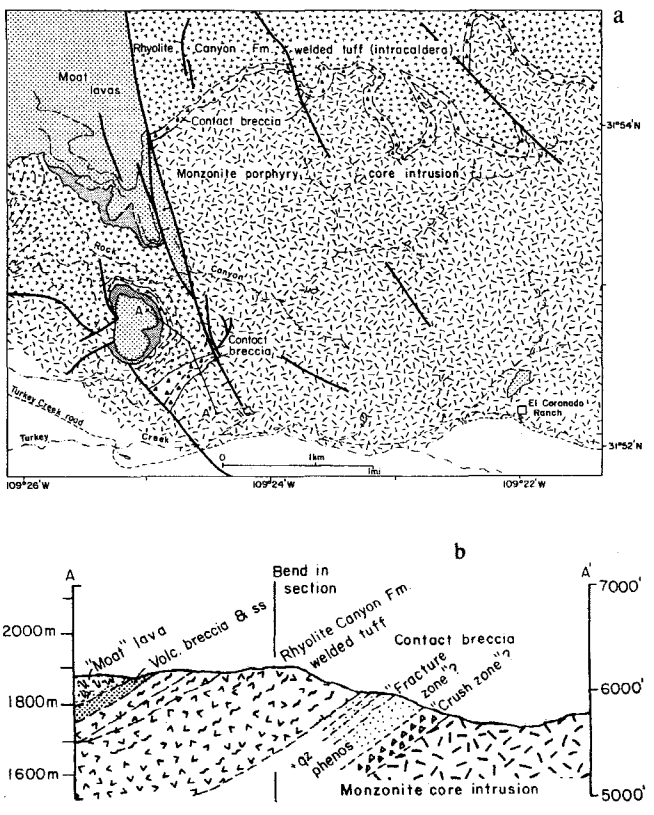

FIGURE 7—Simplified geologic map (**a**) and cross section (**b**) of area north of lower Turkey Creek. Scale bar and latitude–longitude grid approximate; base from aerial photograph. Horizontal = vertical scale in section.

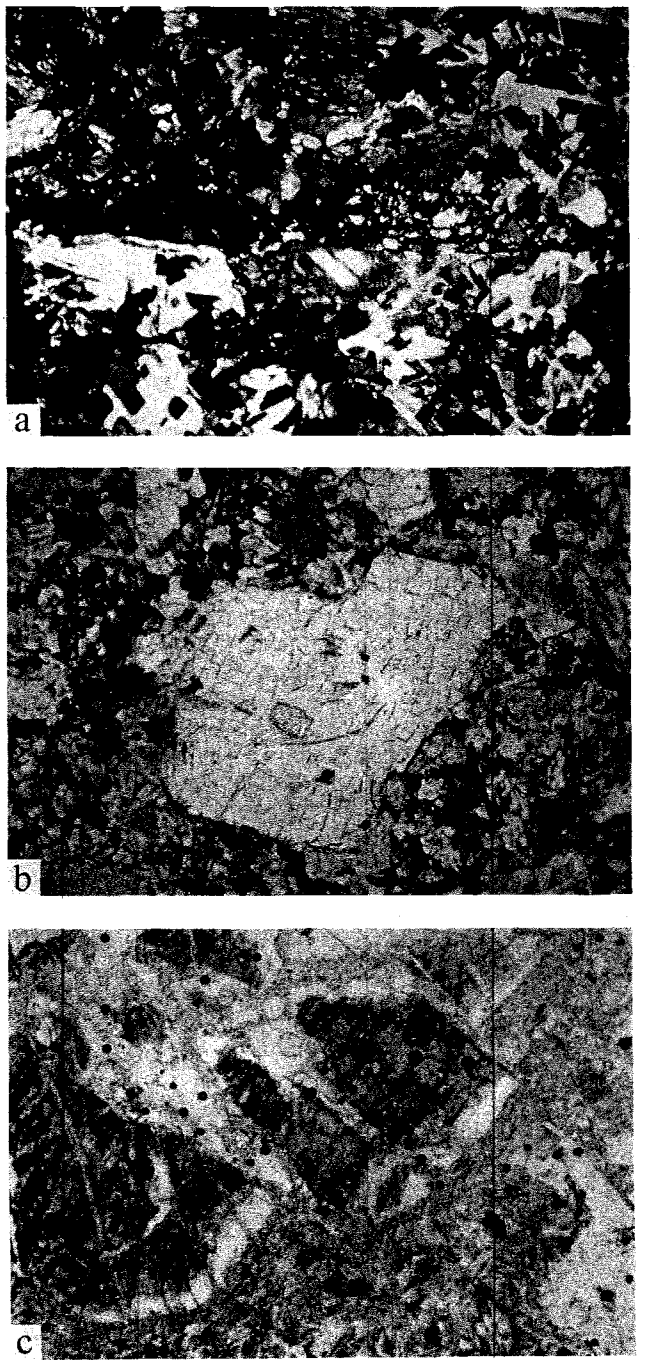

FIGURE 8—Photomicrographs of granophyre clasts in monzonite roof breccia, showing: **a**, mylonite band; **b**, micro-fractured quartz phenocryst; **c**, micro-faulted feldspar phenocryst. Image widths = 3.6 mm.

ophyre. We interpreted the upper zone rocks as highly fractured and altered, and/or melted, Rhyolite Canyon Formation tuff because of the presence of rounded quartz phenocrysts and low-angle foliation. Marjaniemi (1969) also recognized an increase in degree of alteration and fracturing of the tuff over a distance of up to several hundred meters from the monzonite contact. He regarded granophric textures in the tuff close to the contact as indistinguishable from those in the monzonite, and relied on the presence of quartz phenocrysts to identify the tuff. Marjaniemi attributed these effects to contact metamorphism of the tuff by the monzonite. This is the simplest and likely correct explanation, but, having seen quartz-phyric magmatic phases of the monzonite elsewhere (some with surficial lava features, such as flow folds), we believe that the presence of relict quartz phenocrysts does not uniquely identify the tuff. Therefore, we have also entertained an alternative working hypothesis: that the quartz-phyric granophyre might represent a quenched upper border zone of the intrusion. However, this explanation would require unconventional ideas about roof rocks to the intrusion (or lack thereof), as explained in the discussion.

The welded tuff exposed above the cataclastic breccia interval contains several cooling breaks and may be divided into two or three ash-flow deposits. Compaction foliation attitudes are variable in the lower part of the exposed welded tuff, suggesting large-scale rheomorphic folding.

The welded tuff is locally overlain by several tens of meters of brown-to-tan-weathering, bedded, tuffaceous clastic breccia and ash-rich sandstone. This sedimentary unit contains clasts of Rhyolite Canyon Formation welded tuff and rhyolite lava. Similar clastic breccias occur in equivalent stratigraphic positions in several areas of the caldera (e.g., upper Rucker Canyon, Fig. 9). Clast populations elsewhere are dominated by Rhyolite Canyon Formation tuff and monzonite porphyry; exposures here in Turkey Creek are unusual by virtue of also containing rhyolite lava clasts; the source of these clasts is unknown.

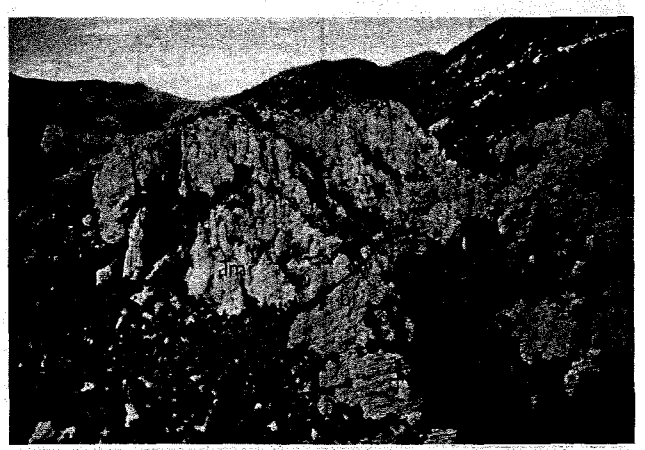

FIGURE 9—Photograph showing thick section of crossbedded clastic breccias and sandstones (br) that unconformably overlie Rhyolite Canyon Formation tuff and are conformably overlain by rhyolite moat lavas (Tmr). The breccias contain abundant Rhyolite Canyon Formation welded-tuff clasts. In the floor of upper Rucker Canyon (off-frame to left), the breccias unconformably overlie monzonite porphyry and contain porphyry clasts.

The dominance of Rhyolite Canyon clasts and the stratigraphic position of the sedimentary unit below the moat lavas indicate that an erosion–deposition cycle took place after caldera collapse and Rhyolite Canyon eruption, but prior to eruption of most (if not all) moat rhyolite. The presence of monzonite porphyry clasts in breccias of upper Rucker Canyon indicates that sufficient time passed for local erosional unroofing of the porphyry prior to eruption of dacite and high-silica rhyolite moat lavas.

The section north of Turkey Creek is capped by an erosional remnant of biotite–sanidine rhyolite of the moat-lava sequence. The lava has a basal carapace breccia that is in depositional contact with the underlying sedimentary unit. From the crest of this knob, a thick section of moat lavas overlying Rhyolite Canyon Formation tuff is visible to the north. To the northeast, the smooth-weathering outcrops of the central porphyry intrusion are easily distinguished.

Backtrack to cars and continue east 2.6 mi to Coronado Ranch (University of Arizona Field Camp).

18.3 **STOP 6. Coronado Ranch** (overnight). If time and light permit, outcrops of monzonite porphyry of the core intrusion may be examined in the bed of Turkey Creek near the gate to Coronado Ranch.

Day 2, Part 3. Intrusive–extrusive transitions in the ring intrusion

From Coronado Ranch we return to AZ-181 and drive to the intersection with Pinery Canyon road (0.1 mi west of entrance to Chiricahua National Monument). Road-log mileage begins at this intersection. We drive east, up Pinery Canyon and parallel to the northern topographic margin of Turkey Creek caldera. Near the head of Pinery canyon, we climb through Bisbee Group sedimentary rocks to Onion Saddle, just outside the structural margin of the caldera. Turning south, we cross into the ring intrusion of the caldera (Fig. 10a) and investigate field relations atop the ring intrusion at Barfoot and Ida Peaks.

The structural margin of the Turkey Creek caldera is intruded by a wide (2–4 km) ring dike of monzonite porphyry (Fig. 1). Where the ring dike is not present at the surface, the structural margin of the caldera is buried by rhyolites and dacites of the moat-lava sequence. We have identified only one feeder for the moat rhyolites, a subvertical dike exposed in the south wall of Pinery Canyon northeast of Ida peak (Fig. 10). This dike cuts the outer margin of the ring intrusion, as well as Bisbee Group sedimentary rocks immediately outside the caldera.

We believe that Rhyolite Canyon tuff eruption and caldera collapse were followed immediately by intrusion of monzonite porphyry into the Rhyolite Canyon feeder zones (both ring dike and faults in the caldera floor). These shallow intrusions erupted dacite lavas to form the stratigraphically lowest lavas now exposed atop the ring dike, as well as local accumulations that overlie Rhyolite Canyon tuff along linear zones within the caldera (Fig. 5). The latter may represent porphyry that was extruded from fault-controlled

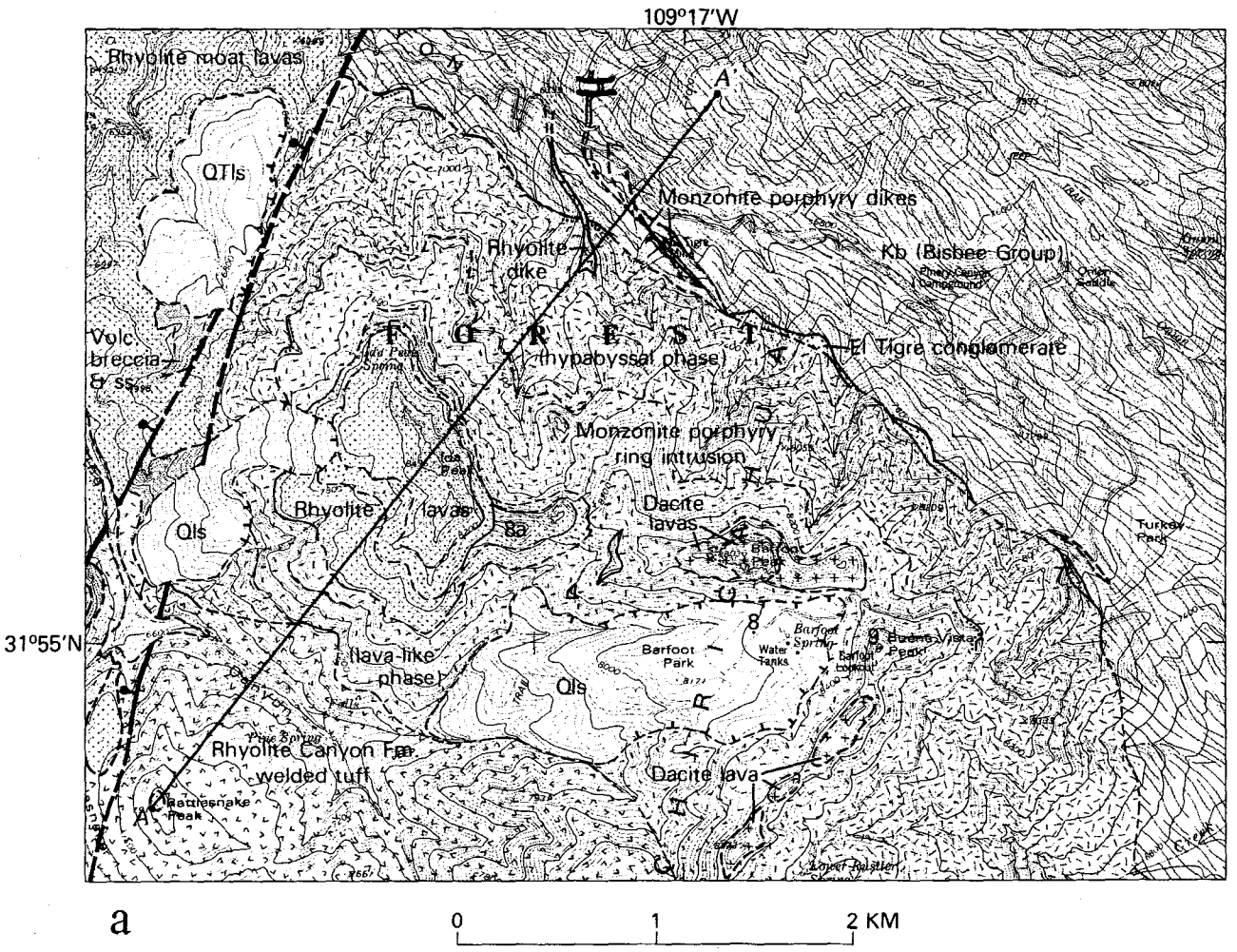

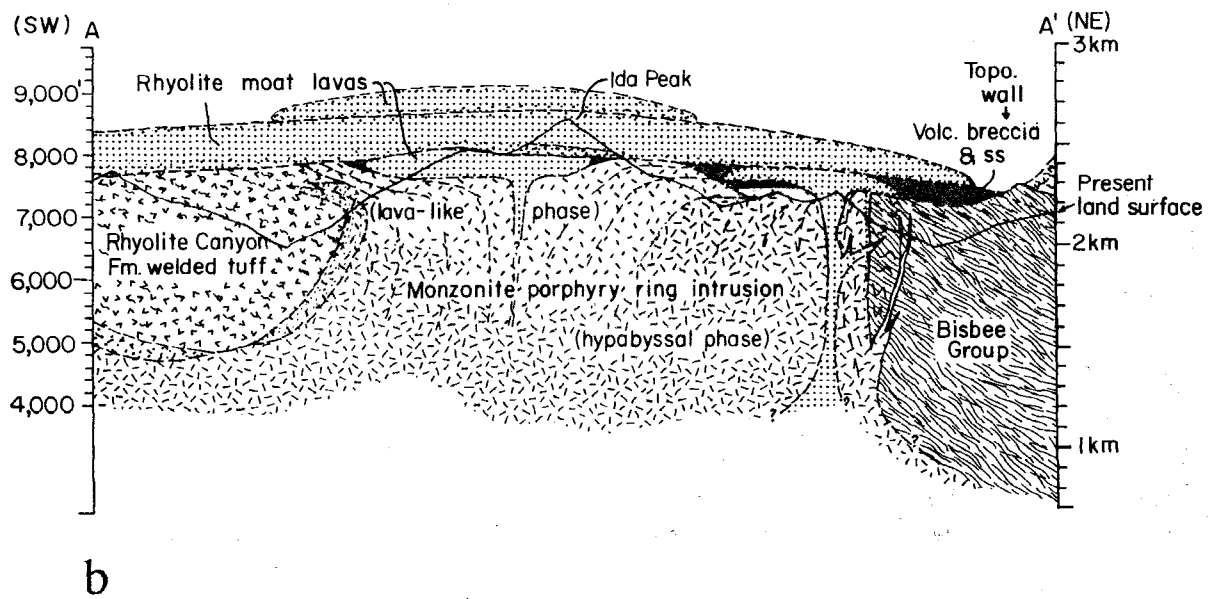

FIGURE 10—Geologic map **(a)** and interpretative cross section **(b)** of the northeastern segment of the ring intrusion, Turkey Creek caldera. Field-trip localities are indicated by stop number. Profile line shows present topography. Stippled areas represent carapace breccia. Qls = Quaternary landslide deposits, QTls = Quaternary or Tertiary landslide deposit.

dikes formed as the roof of the magma chamber broke up during caldera collapse. Transitional intrusive–extrusive textures and morphologic features (described below) are seen atop the ring intrusion and in the central outcrops of extrusive porphyry.

Results of drilling into rhyolite feeder dikes at the Inyo domes, California, has led to the suggestion that significant degasing of rhyolite magma may take place at shallow levels within the intrusive environment; that rhyolite magma may vesiculate, degas, and weld itself back together in the conduit (Eichelberger et al., 1986). Scandone and Malone (1985) argue for an interplay between magma supply rate and disruption level within the Mount St. Helens conduit to explain transitions between sustained and pulse eruptions during the 1980 plinian eruptions. Although there are questions regarding the primary volatile contents of rhyolites and mechanisms of degasing in a vent (Friedman, 1988), it is apparent that given a zoned or layered magma reservoir, pyroclastic eruption would be succeeded by effusive eruption as more volatile-poor parts of the reservoir are vented. We believe that transitions between pyroclastic and effusive rocks observed in the near-surface vent environment of the Turkey Creek caldera record such a process.

Mileage

0.0 Intersection of AZ-181 and Pinery Canyon Road. **Turn right** (south) on Pinery Canyon Road. **1.0**

1.0 View to north of local pyroclastic flows in Faraway Ranch Formation. **6.4**

7.4 Methodist Camp Road junction. **Continue straight** on Pinery Canyon/Onion Saddle Road. **FUTURE USERS:** If time permits, good exposures of moat rhyolite lavas and pyroclastic flows are available in the roadcuts of Methodist Camp Road near Downing Pass (~1 mi). **1.8**

9.2 El Tigre mine road junction, continue straight to Onion Saddle. The El Tigre is a small silver and silica-flux mine located on quartz veins developed subparallel to the outer contact of the ring intrusion. **3.0**

12.2 Onion Saddle and junction with Rustler Park Road (FS-42D). **Veer right (south) on Rustler Park Road. 1.2**

13.4 **STOP 7. Structural margin of Turkey Creek caldera.** Pull off on right. This is the contact between the ring intrusion and precaldera sedimentary and volcanic rocks (Fig. 10). A southwesterly dipping section of sandstone, siltstone, conglomerate, and minor limestone beds make up the precaldera rocks near the contact here. These rocks are part of a dominantly clastic Tertiary(?) unit that overlies Lower Cretaceous Bisbee Group sandstone and limestone. The clastic unit is mapped as the informal El Tigre conglomerate by Tsugii (1984) and may correlate with the Cretaceous or Tertiary Nipper Formation of Sabins (1957), as noted by Drewes and Williams (1973). Breccia clasts of limestone from the underlying Cretaceous or Paleozoic rocks, as well as dacitic and rhyolitic volcanic rocks are common in exposures of the unit between here and the El Tigre mine.

Examine the roadcuts between the quartz-vein zone (exposed behind the cars) and the monzonite porphyry ahead (~100 m southwest). The quartz veins are a continuation of the El Tigre vein system that trends northwesterly, subparallel to, but locally branching away from, the margin of the ring intrusion where they intrude Bisbee and Nipper rocks.

An important question to consider here is the nature of the contact. Although the porphyry regionally intrudes Bisbee and Nipper rocks, sediments that overlie the Nipper here appear to have ponded against the eroded porphyry (and are therefore correlative with moat sediments exposed elsewhere in the caldera). Examine the altered breccia beds immediately adjacent to the porphyry, which contain highly altered porphyry clasts (some quartz-phyric).

Note that the porphyry has a fine-grained (but not glassy) groundmass near the contact. Miarolitic cavities containing terminated quartz crystals are well exposed in outcrops about 30 m from the contact. A thin air-fall tuff bed(?) *within* the porphyry (exposed in a roadcut 0.4 mi to the southwest) indicates that the porphyry was partly extrusive. Thicker pyroclastic intervals form benches within the porphyry cliffs to the south and east. These occurrences suggest that we are within an eroded ring-vent complex, where exposures of porphyry proximal to (and deeper within) the locus of ring intrusion show intrusive features; more distal exposures have characteristics of thick lava flows.

Continue southwest on the Rustler Park Road. **0.9**

14.3 Junction with Barfoot Park (Scout Camp) Road (FS 357). **Turn right** (toward Barfoot Park). **0.8**

15.1 **STOP 8. Barfoot Park. Hike to Barfoot–Ida Peak saddle** (~3 hrs. round trip). Extrusive phase of monzonite porphyry and moat rhyolite flows. **Walk down the valley to the west; intercept and hike northwest (right turn) on the Ida Peak Forest Service trail.** The Ida Peak trail contours along the southwest flank of Barfoot Peak to a saddle between Barfoot and Ida Peaks. We walk through a large landslide deposit for the first 0.4 mi, then climb up to the saddle. Look for outcrops of glassy-matrix porphyry and erosional remnants of moat breccia (with Rhyolite Canyon Formation welded-tuff clasts) as the trail rounds the western spur of Barfoot Peak and climbs to the saddle (Fig. 10).

This is an area that we mapped in moderate detail, building on the thesis work of Karl Tsugii (1984). Tsugii recognized several andesitic to rhyolitic lava flows overlying the ring intrusion here. We agree with this interpretation, but we regard the lower (mainly dacitic) lavas as intrusive–extrusive features. We believe that the dacitic lavas, which form prominent benches on the low flanks of Ida Peak and cap Barfoot Peak, represent the extrusive equivalents of the monzonite porphyry. Transitional textures and compositions of the lavas and underlying porphyry intrusion (Figs. 6, 11, Table 1) indicate that we are seeing various levels through a caldera ring-intrusion and vent complex, as shown by the cross section in Fig. 10b. These relations suggest that the transitional intrusive–extrusive rocks of the Turkey Creek caldera preserve an abrupt compositional gradient that may have formerly been a layer

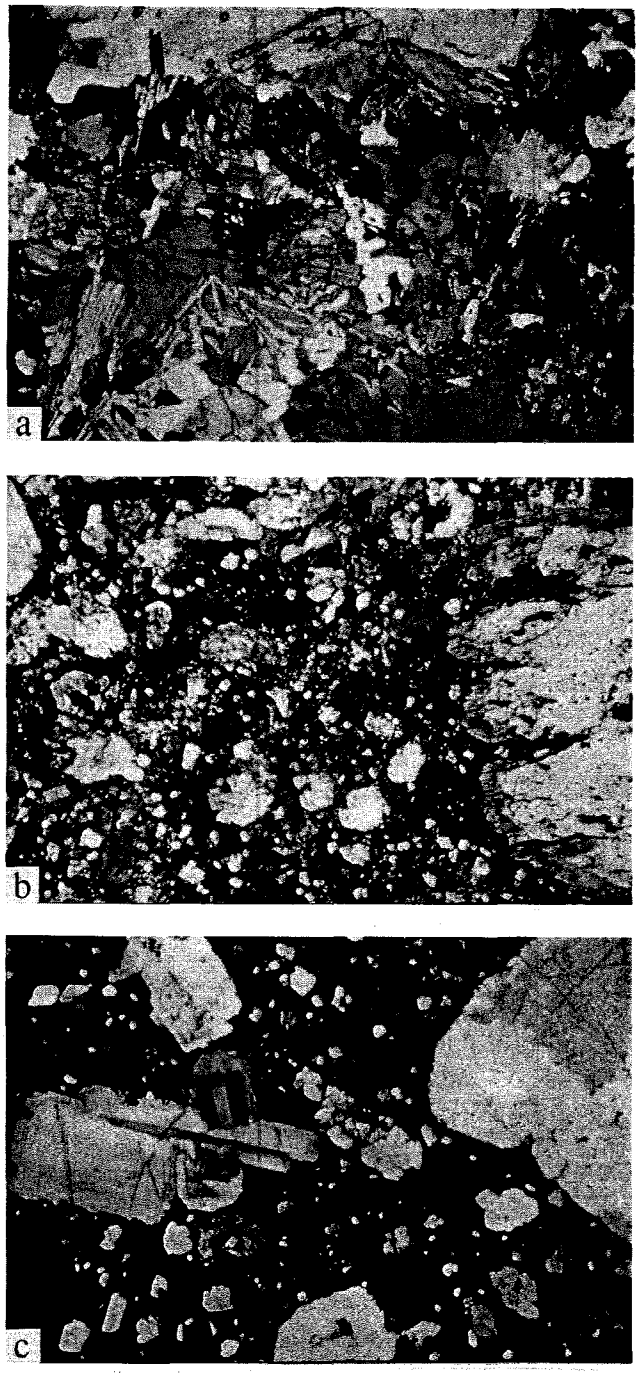

FIGURE 11—Photomicrographs (frame width 3.6 mm) showing a transition from granophyre-matrix (a) biotite–clinopyroxene–hornblende–two-feldspar monzonite porphyry to microcrystalline (b) and glass-matrix (c) porphyry lava. Note the presence of quartz phenocrysts in the glass-matrix lava. Samples from the flanks of Barfoot Peak.

interface within the source magma chamber. This hypothesis is further developed in the discussion.

STOP 8a. Barfoot–Ida Peak saddle (elevation 8140 ft). The saddle is within the lower of two rhyolite lava flows of the moat sequence that caps Ida Peak. **Hike up the ridge to the east** (toward Barfoot Peak). This traverse takes us down-section through flow-folded rhyolite lava and lower carapace breccia of the lower moat rhyolite, then into platy-jointed dacite/monzonite porphyry with local remnants of moat breccia on its erosional(?) surface, and finally into glass-matrix dacite lavas that cap Barfoot Peak. **Please keep together;** we will not climb to the top of Barfoot Peak; instead congregate on the western spur-ridge, then "peel off" to the south to intercept the Ida Peak trail back to the cars. We then drive back toward Onion Saddle. **0.7**

15.8 **STOP 9. Barfoot Lookout** (Buena Vista Peak). **Pull off on left near cattleguard. Take lunch** and climb trail to Barfoot Lookout (30 min. up). The Barfoot Lookout provides good views of the ring intrusion and overlying lavas (Stop 8) as well as an overview of the northern edge of the Portal caldera and underlying rhyolites at Silver Peak to the southeast and east.

Discussion: "Working models" for the Turkey Creek caldera

Mid-Tertiary magmatism in the Chiricahua Mountains began at about 30 Ma, with eruption of voluminous rhyolite lavas and pyroclastic flows to form the Faraway Ranch Formation and coeval deposits that predate both the Portal and Turkey Creek calderas. Older mafic magmatism is recorded by basaltic to andesitic lavas interbedded with clastic rocks (Nipper Formation?) that overlie the Bisbee Group, and by gabbro intrusions in the upper part of the Bisbee Group; both of these rock types are seen in sections east of Onion Saddle. A 31.8 ± 0.7 Ma whole-rock K–Ar age on an andesite lava interbedded with the Nipper Formation(?) along the road east of Onion Saddle is reported by Shafiqullah et al. (1978).

Hypothetical structural models for the Turkey Creek caldera are outlined in Fig. 12a, b. Model 12a begins (stage 1) with the formation of a high-silica rhyolitic cupola atop a monzonitic magma chamber. We have shown a free-air surface and granophyre chilled margin on the cupola in Fig. 12a. We realize this is a departure from traditional caldera models, but, given the lack of precaldera floor (magma-chamber roof) rocks in the eroded core of the caldera, we have adopted this simple geometric solution as one of two working models. Intrusion of monzonite magma as a sill or laccolith during late stages of caldera formation provides a more traditional explanation for the apparent lack of caldera floor rocks (Fig. 12b). We present both models here in the hope that they will foster lively discussion during the field trip. The character of the quartz-phyric granophyre border zone of the monzonite (Stop 5) may provide the answer. If the zone represents quenched Rhyolite Canyon magma, the free-air surface model would be preferred; if the border is a contact metamorphic zone, the laccolith model gains credence.

Circumstantial support for the free-air surface model is provided by the character of rhyolitic magmatism preceding the Turkey Creek caldera. A large volume of rhyolite was erupted effusively in the Chiricahua Mountains prior to development of the Portal and Turkey Creek calderas. It is apparent that large reservoirs of high-silica magma were developing at shallow crustal levels, and that these magmas were relatively volatile-poor; only at Portal, Turkey Creek, and Cochise Head (the latter in the northeast Chiricahua Mountains) did large-scale Plinian eruptions and caldera collapse occur. If ash-flow tuff eruption is viewed as magmatic "boiling" rather than explosive ballistic ejection, the need for a confinement vessel (and magma-chamber roof) is obviated. In this context, the development of a cupola of

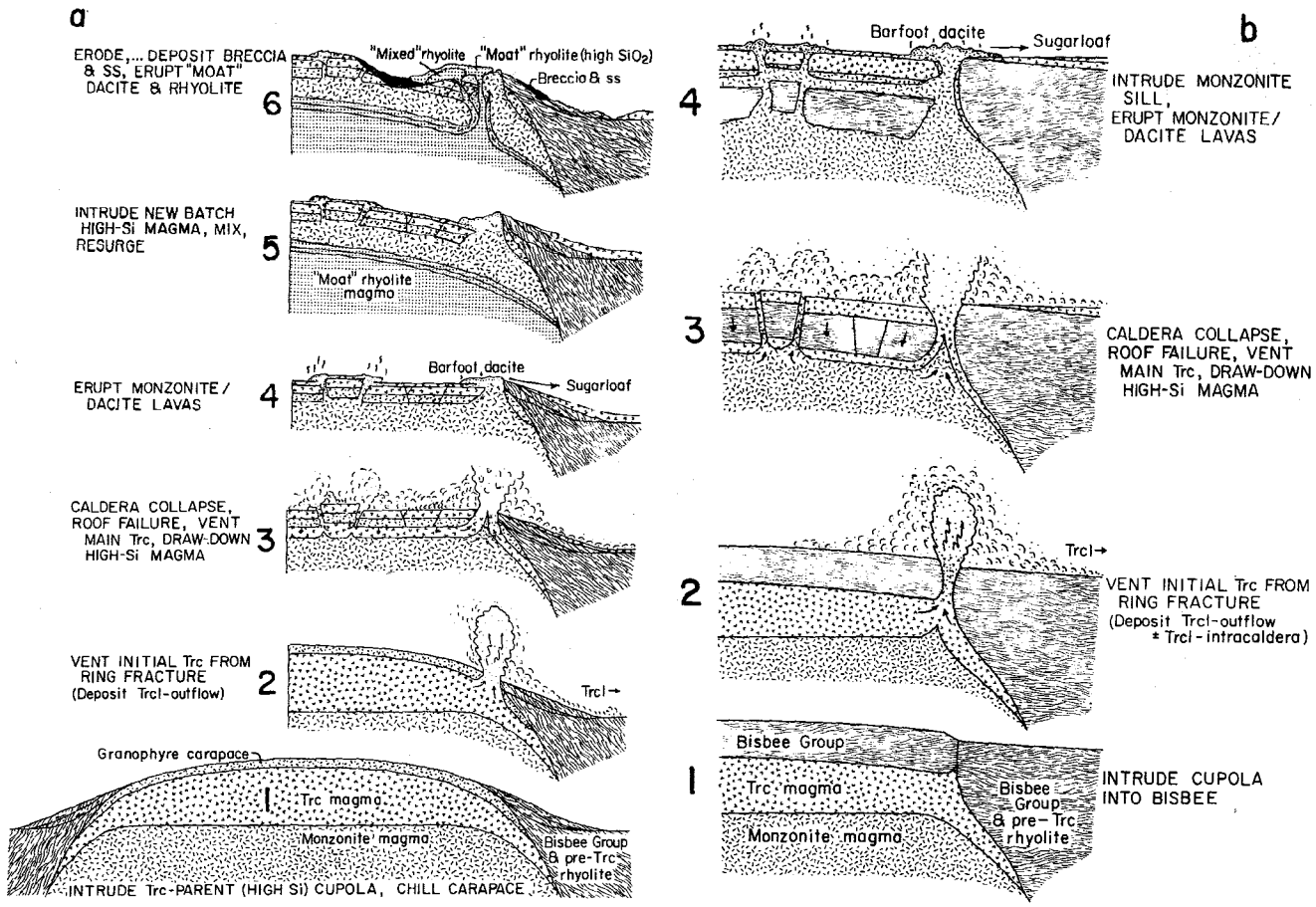

FIGURE 12—Working models for structural stages in the evolution of the Turkey Creek caldera. **a**, free-air surface model; **b**, laccolith model. Trc = tuff of Rhyolite Canyon Formation; Trcl = lower members (units I and II of Latta, 1983) of outflow tuff of Rhyolite Canyon Formation.

relatively volatile-poor, high-silica magma, that was progressively unroofed prior to eruption, is easier to envision. This concept is not new, batholiths with free air were proposed 20 years ago (Hamilton and Myers, 1967).

During stage 2 (Fig. 12a, b), initial eruption of Rhyolite Canyon Formation tuff took place and resulted in deposition of units I and II of the Monument member in the National Monument. The apparent lack of intracaldera equivalents of these lower units may be explained by the lack of a topographic depression at this early stage of caldera formation. Alternatively, intracaldera equivalents of the lower units could have accumulated, only to have become sole rocks to a monzonite laccolith intruded into the caldera fill at a later stage (Fig. 12b, stage 4). Intrusion, metamorphism, and melting of the intracaldera tuff by the underlying porphyry is observed at some localities along the roof-breccia contact, relations that favor the laccolith model. In the Portal caldera, a dacite porphyry sill intruded and mingled with intracaldera tuff (Bryan, this volume), providing a nearby analogue for sill or laccolith intrusion into intracaldera tuff. In the general context, withdrawal of magma from deep reservoirs may favor foundering of intracaldera tuff and redistribution of magma as sills and laccoliths within a thick intracaldera sequence. Only where extensive sections and very deep levels of intracaldera rocks are exposed can such hypabyssal intrusive relations be observed. Even at Turkey Creek, where erosion penetrates several kilometers into the caldera, the distinction between source pluton and laccolith is not readily made.

Stage 3 shows Plinian activity, with caldera collapse accompanying eruption of unit III of the Rhyolite Canyon Formation tuff, and accumulation of most of the unit III ash-flow deposits within the caldera. The interface with underlying monzonitic magma was drawn up into both ring and central vents as high-silica rhyolite was evacuated from the chamber by eruption.

Stage 4 models the eruption of monzonitic magma to form transitional intrusive–extrusive rocks, now preserved within the upper levels and margins of the ring intrusion and along fault zones within the caldera; the latter record the disruption of the caldera floor (magma-chamber roof) during collapse. Monzonitic magma erupted at this stage may have fed a dacite lava flow that reached the National Monument (dacite of Sugarloaf Mountain, Stop 4). This is the stage of the laccolith model at which monzonite magma must have been intruded into the intracaldera tuff, or at the Bisbee–Rhyolite Canyon tuff contact (Fig. 12b).

Stage 5 records resurgence, brought about by the arrival of a new batch of high-silica magma into the shallow magmatic system. A period of erosion and deposition ensued between the close of stage 4 and the onset of stage 6. Breccias containing clasts of Rhyolite Canyon tuff and monzonite porphyry were deposited in the developing caldera moat during this hiatus in magmatism.

Finally, during stage 6, high-silica rhyolite lavas were erupted and filled the caldera moat (locally to overflowing). The lower rhyolite moat lavas are less evolved, and may represent mixed magma derived from the interface between monzonite magma remaining from the Turkey Creek cycle and new high-silica magma.

Mid-Tertiary volcanism in the eastern Chiricahuas: The Portal caldera

Charles R. Bryan

Department of Geology, University of New Mexico, Albuquerque, New Mexico 87131

Introduction

The central Chiricahua Mountains are dominated by a thick section of mid-Tertiary silicic volcanic rocks, which are associated with at least two well-exposed ash-flow tuff calderas: the Portal caldera, source of the tuff of Horseshoe Canyon, and the Turkey Creek caldera, source of the Rhyolite Canyon Formation tuff (Marjaniemi, 1969). These two calderas are closely linked both chemically and temporally; collapse of the Turkey Creek caldera occurred shortly after formation of the Portal caldera, and resurgence of both occurred simultaneously.

The Portal caldera is exposed in the eastern half of the Chiricahua Mountains (Fig. 1). It is a relatively shallow trap-door caldera hinged at the north in the vicinity of Portal Peak and deepening to the south. Its fill, the tuff of Horseshoe Canyon, reaches a maximum thickness of at least 500 m near the mouth of Horseshoe Canyon. The resurgent dome is cut by a north-northeast-trending graben, in which the outflow sheet from the adjacent Turkey Creek caldera (Rhyolite Canyon tuff) is preserved. The western boundary is obscured by the younger Turkey Creek caldera, and the eastern half is buried beneath the San Simon Valley.

Geologic overview

The oldest rocks exposed in the eastern Chiricahuas are folded and thrust-faulted units of Paleozoic and Mesozoic age. They are unconformably overlain by Late Cretaceous–early Tertiary(?) andesitic and dacitic lava flows, ash flows,

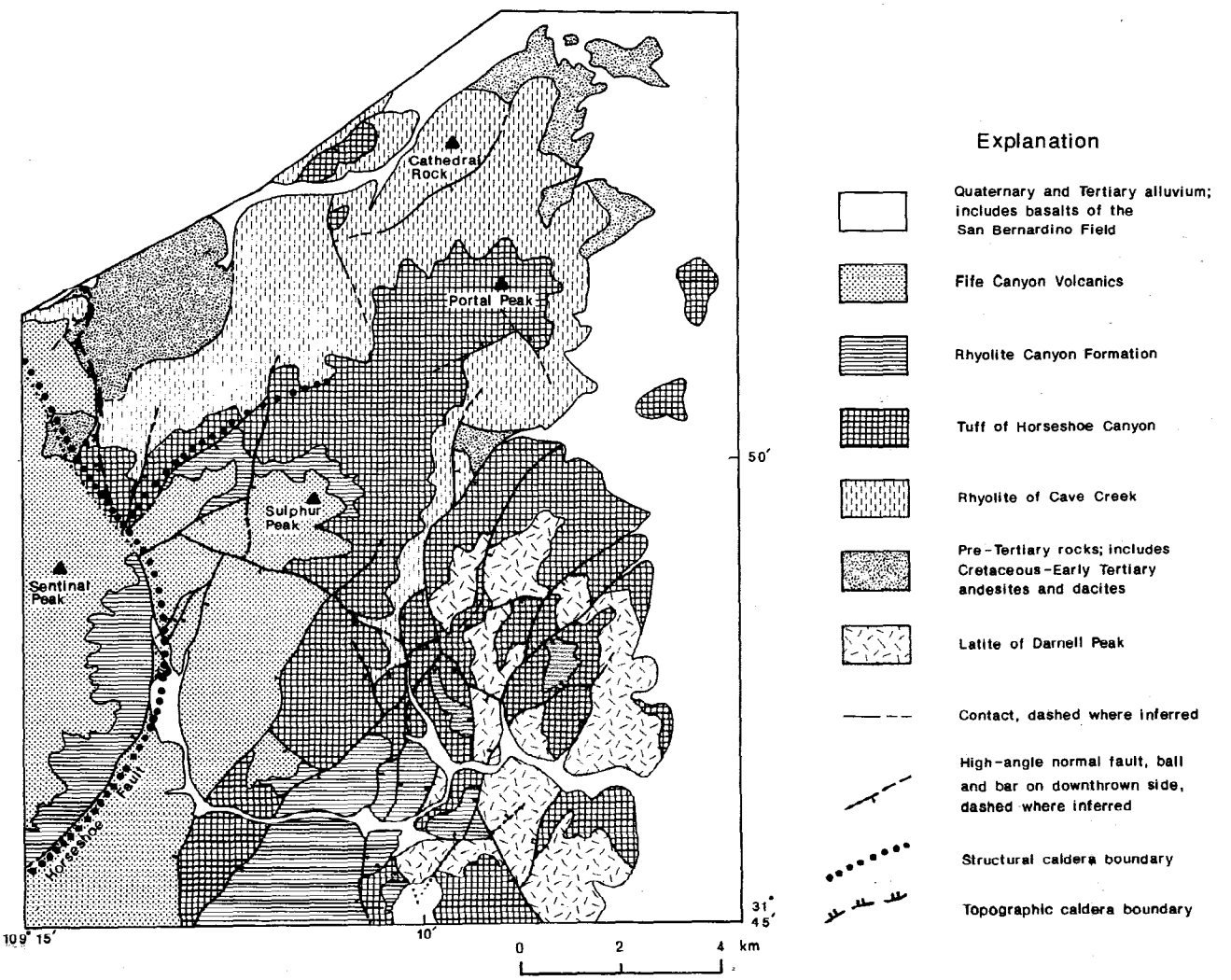

FIGURE 1—Simplified geologic map of the eastern Chiricahua Mountains, showing rock units and major structural features associated with the Portal and Turkey Creek calderas.

and volcanic sediments, which in turn are unconformably overlain by the mid-Tertiary silicic volcanic rocks shown in Fig. 1. The lowermost of the late Oligocene volcanic rocks is the rhyolite of Cave Creek. This unit is composed of crystal-poor, commonly highly altered and brightly colored high-silica rhyolite lava flows and related tuffs, breccias, and volcaniclastic sediments. North of Portal Peak, three large lava flows, each up to 250 m thick, dominate the unit. The rhyolite of Cave Creek is overlain by the tuff of Horseshoe Canyon: the ash-flow tuff that was derived from, and fills, the Portal caldera.

The tuff of Horseshoe Canyon consists of two members; the lower member is a densely welded single cooling unit, zoned from quartz, sanidine, high-silica rhyolite at the base to two-feldspar latite at the top (Fig. 2). South of Horseshoe Canyon, the central and upper parts of the lower member contain abundant mafic and felsic fiamme, each up to 30 cm long. Cognate(?) angular inclusions are also present. The uppermost part of the member has been rheomorphically mobilized; fiamme have been extremely flattened and even isoclinally folded. Rheomorphism may have been caused by intrusion of the latite of Darnell Peak, which occurs as a 300 m thick sill between the lower and upper members of the tuff in this area. The upper member is rhyolitic, much subordinate in volume, and occurs only in the southern part of the area. The tuff of Horseshoe Canyon is 350–500 m thick in most areas, and is interpreted as caldera fill; two 100–150 m thick fault-bounded blocks in Cave Creek Canyon have been tentatively identified as outflow facies.

The tuff of Horseshoe Canyon has been radiometrically dated several times. Marjaniemi (1969) obtained ages of 26.4 ± 0.7 Ma (K–Ar, biotite) and 25.1 ± 1.2 Ma (K–Ar, sanidine, upper member). Bryan (1988) obtained a K–Ar biotite age of 27.6 ± 0.7 Ma, and a Rb–Sr isochron age, on a suite of 10 samples from the lower member, of 25.3 ± 0.5 Ma (2 sigma). The Rb–Sr age is preferred; field relations are consistent with the tuff of Horseshoe Canyon having been erupted immediately prior to the Rhyolite Canyon Formation (average age 25.2 Ma; Latta, 1983).

The lower member of the tuff of Horseshoe Canyon is strongly zoned from 77 to 65% SiO_2; chemical variation in the tuff is given in Table 1. Major- and trace-element trends are broadly linear with respect to silica. Compatible vs. incompatible trace-element trends are hyperbolic, suggesting that the variation represents fractional crystallization; however, the abundance of mafic and felsic fiamme in the tuff shows that mixing of several different layers or levels in the magma chamber occurred during eruption. Strontium 87/86 initial ratios for the tuff are slightly scattered (Table 1); there is no consistent change with silica content. The scatter may be due to wall-rock contamination during eruption; possible contaminants are Precambrian granite and Tertiary(?) granite; xenoliths of both are present in the tuff of Horseshoe Canyon.

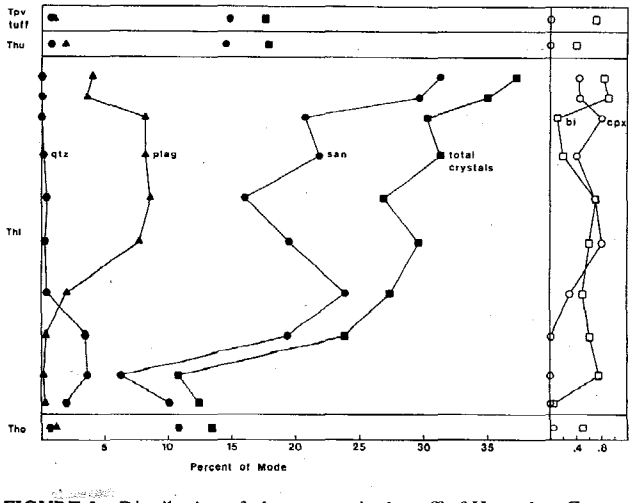

FIGURE 2—Distribution of phenocrysts in the tuff of Horseshoe Canyon. Tho = outflow sheet; Thl = lower member; Thu = upper member; Tpv = thin tuff in unit of Pothole Canyon.

A thin, heterogeneous section of rocks occurs locally between the tuff of Horseshoe Canyon and the Rhyolite Canyon Formation tuff in the area of the Portal caldera. These rocks are referred to as the unit of Pothole Canyon, but extent is not sufficient to show in Fig. 1. The unit includes volcaniclastic sediments, a thin rhyolite ash-flow tuff, a porphyritic latite lava flow, and a basaltic andesite lava flow—the most mafic mid-Tertiary unit in the area.

The Rhyolite Canyon high-silica welded tuff occurs in the mapped area as both thick (650 m) caldera fill, within its source Turkey Creek caldera west of the Horseshoe fault, and as outflow east of the fault. As in Chiricahua National Monument, the outflow sheet has two major cooling units, although the lower one is only locally present. Unlike in the Monument, however, Rhyolite Canyon outflow sheet in the Portal caldera is pervasively altered, with a chalky-gray matrix and characteristic white, clayey sanidines.

Moat deposits of the Turkey Creek caldera, the Fife Canyon volcanics (Latta, 1983), are present along the structural boundary of the Turkey Creek caldera and extend into the Portal caldera (Fig. 1). The lowermost member of the Fife Canyon volcanics is a thick (several hundred meters) sequence of porphyritic latite lava flows, which are the extrusive equivalent of the monzonitic stock that intrudes the resurgent dome of the Turkey Creek caldera. Several local members, including epiclastic breccias, rhyolite lava flows, air-fall tuffs, and quartz latite ash-flow tuff and lava flows, occur on top of this unit, and the entire section is capped by a group of voluminous, aphyric, flow-banded, high-silica rhyolite lava flows.

The latite of Darnell Peak occurs primarily as a large sill, up to 300 m thick, which intrudes the tuff of Horseshoe Canyon, typically between the lower and upper members, in the vicinity of Horseshoe Canyon. It contains about 40% phenocrysts, mostly sanidine and plagioclase as euhedral phenocrysts to 1.2 cm, and minor clinopyroxene, biotite, and opaque minerals. Its contact with the lower member is locally diffuse over a distance of a few meters, suggesting that the sill intruded while the tuff of Horseshoe Canyon was still hot.

Structure and caldera evolution

Stages in the development of the Portal and Turkey Creek calderas are summarized in the east–west schematic cross sections of Fig. 3. The Portal caldera is a trap-door collapse feature in north–south profile and has a hinge zone in the north, near Portal Peak. The structural margin is exposed in South Fork Canyon; tuff and wall rocks are intensely altered, lithic fragments are abundant near the base of the caldera-fill tuff, and a ring-fracture fault and ring-fracture intrusions are present.

Only a small part of the Portal caldera is exposed; esti-

TABLE 1—Analyses of mid-Tertiary volcanic units in the central Chiricahua Mountains. *Below detection limits. 1 = rhyolite of Cave Creek; 2–5 = tuff of Horseshoe Canyon, lower member, bottom to top; 6 = tuff of Horseshoe Canyon, upper member; 7 = basaltic andesite flow, unit of Pothole Canyon; 8 = Rhyolite Canyon Tuff, vitrophyric base of outflow sheet; 9 = Rhyolite Canyon Tuff, caldera fill; 10 = Fife Canyon Volcanics, porphyritic latite member; 11 = Fife Canyon Volcanics, upper rhyolite member.

Sample #	1	2	3	4	5	6	7	8	9	10	11
SiO_2	75.20	77.06	73.81	70.52	63.82	71.25	53.20	73.71	76.77	64.08	77.15
TiO_2	0.10	0.16	0.26	0.45	0.82	0.39	1.59	0.14	0.16	0.81	0.10
Al_2O_3	13.18	11.90	13.29	15.17	16.88	14.43	17.15	11.47	11.24	15.05	12.67
Fe_2O_3	0.58	0.76	1.18	1.69	2.33	1.51	6.61	0.96	0.84	2.64	1.10
FeO	0.40	0.12	0.07	0.19	0.67	0.02	1.41	0.58	0.11	1.50	0.07
MnO	0.07	0.06	0.08	0.07	0.09	0.08	0.11	0.09	0.04	0.10	0.09
MgO	0.02	0.07	0.15	0.28	0.66	0.10	4.52	0.10	0.03	1.06	0.03
CaO	0.48	0.17	0.27	0.62	1.76	0.26	7.25	0.78	0.11	3.28	0.56
Na_2O	3.41	3.07	3.31	4.21	4.00	1.57	3.56	4.27	0.84	3.45	3.82
K_2O	5.15	5.66	6.33	6.22	6.32	9.08	2.27	2.92	8.60	5.18	4.58
P_2O_5	*	*	*	0.04	0.15	*	0.36	*	*	0.24	*
H_2O^+	0.55	0.28	0.35	0.43	.0.58	0.62	2.11	4.29	0.29	2.63	0.37
H_2O^-	0.06	0.00	0.00	0.00	0.02	0.00	0.68	0.18	0.04	0.06	0.04
Total	99.20	99.31	99.10	99.89	98.10	99.31	100.82	99.49	99.07	100.09	100.58
Sc	1.39	2.21	3.08	4.93	6.69	3.96	23.40	2.13	2.27	9.00	1.50
Zn	49	61	66	62	69	54	103	96	54	81	54
Rb	681	404	371	249	162	539	67	624	670	208	636
Sr	11.10	9.76	23.0	65.9	284	22.8	550	85.5	11.2	184	4.07
Y	170	88	90	76	55	154	46	191	127	71	181
Zr	142	152	230	393	847	353	345	271	159	497	146
Nb	67	32	30	26	19	30	17	55	29	27	66
Cs	7.40	5.08	5.40	7.30	2.68	9.50	0.61	56.70	12.20	6.60	7.60
Ba	*	*	182	648	4300	310	835	*	55	859	*
La	32.7	36.3	51.1	88.0	62.3	90.9	52.6	114	36.1	96.0	45.6
Ce	92	83	104	179	135	206	123	167	89	209	114
Nd	43	64	50	66	51	88	74	97	36	96	42
Sm	6.2	4.09	7.1	12.2	8.7	19.7	9.8	20.6	5.13	13.4	9.7
Eu	0.106	0.19	0.72	2.10	3.32	1.15	2.35	0.28	0.21	1.86	<0.07
Tb	1.69	0.72	1.30	1.35	1.04	3.19	1.34	3.47	0.52	0.93	2.43
Dy	9.5	5.5	6.5	8.3	6.1	16.9	6.9	19.0	5.7	7.0	14.4
Yb	12.70	4.97	5.60	4.90	3.49	8.30	3.76	11.40	5.22	5.60	14.10
Lu	1.98	0.75	0.80	0.86	0.576	1.09	0.597	1.69	0.74	0.76	2.12
Hf	9.3	7.46	10.50	15.4	21.2	13.6	8.93	13.7	8.20	14.5	9.2
Ta	9.9	4.58	2.75	2.99	2.65	4.07	1.38	7.24	4.36	2.89	10.5
Th	66.9	31.8	28.9	26.2	13.0	25.1	9.8	56.9	33.7	27.2	59.6
U	12.00	6.27	4.27	4.44	2.25	4.06	1.137	13.90	7.12	5.21	8.89
$Sr(87/86)_o$	0.7140	0.7140	0.7134	0.7137	0.7135	0.7151	0.7085	0.7103	0.7129	0.7097	0.7134

mating the size of the caldera is difficult. A minimum diameter is 12–15 km; a minimum volume for the tuff of Horseshoe Canyon is about 70 km^3. The abundance of large mafic and felsic fiamme and Precambrian and Tertiary(?) granitic inclusions in the tuff of Horseshoe Canyon, just south of the mouth of Horseshoe Canyon, indicates that a source vent for the tuff may have been in this area.

Eruption of the Rhyolite Canyon Formation at about 25.2 Ma caused collapse of the Turkey Creek caldera (Marjamiemi, 1969; Fig. 3c). About 500 km^3 of ash was erupted, forming a caldera about 21 km in diameter. The eastern edge of the caldera is well exposed in the western part of the mapped area (Fig. 1); it truncates the older Portal caldera. Within the zone of overlap, the structural and topographic margins of the Turkey Creek caldera coincide, and the outflow sheet of Rhyolite Canyon Formation tuff extends right up to the ring fracture, the Horseshoe fault of Marjaniemi (1969); apparently, the thick, densely welded tuff of Horseshoe Canyon supported the caldera wall and prevented slumping during formation of the wall of the Turkey Creek caldera. The structural and topographic rims diverge northeast of Sentinal Peak, where the less resistant rhyolite of Cave Creek forms the caldera wall.

Resurgence of the Turkey Creek caldera began before eruption of the porphyritic latite lava flows at the base of the Fife Canyon volcanics (Latta, 1983). The ring fracture of the Portal caldera was an important structure within the younger caldera; the latite lavas are several hundred meters thick north of Sentinal Peak, but are absent within the zone of overlap of the two cauldrons. The latite apparently formed a sill in this area, lifting the intracaldera facies of the Rhyolite Canyon Formation tuff, west of the Horseshoe fault, above the outflow sheet to the east (Fig. 3d).

Continued resurgence of the Turkey Creek caldera triggered resurgence of the Portal caldera, causing doming of the tuff of Horseshoe Canyon and the formation of a northeast-trending graben in which the outflow sheet of Rhyolite Canyon tuff has been preserved. The intracaldera facies of the Rhyolite Canyon tuff in the zone of overlap was also tilted; it dips ~10° away from the dome of the Portal caldera toward the center of the Turkey Creek caldera (Fig. 3e). The high-silica rhyolite lava flows which are the uppermost unit of the Fife Canyon volcanics were then emplaced, forming an angular unconformity on the flanks of the somewhat eroded resurgent dome of the Portal caldera.

Road log

This log is a continuation of the Turkey Creek field trip; the first stop is equivalent to Stop 9 of Pallister and du Bray (this volume).

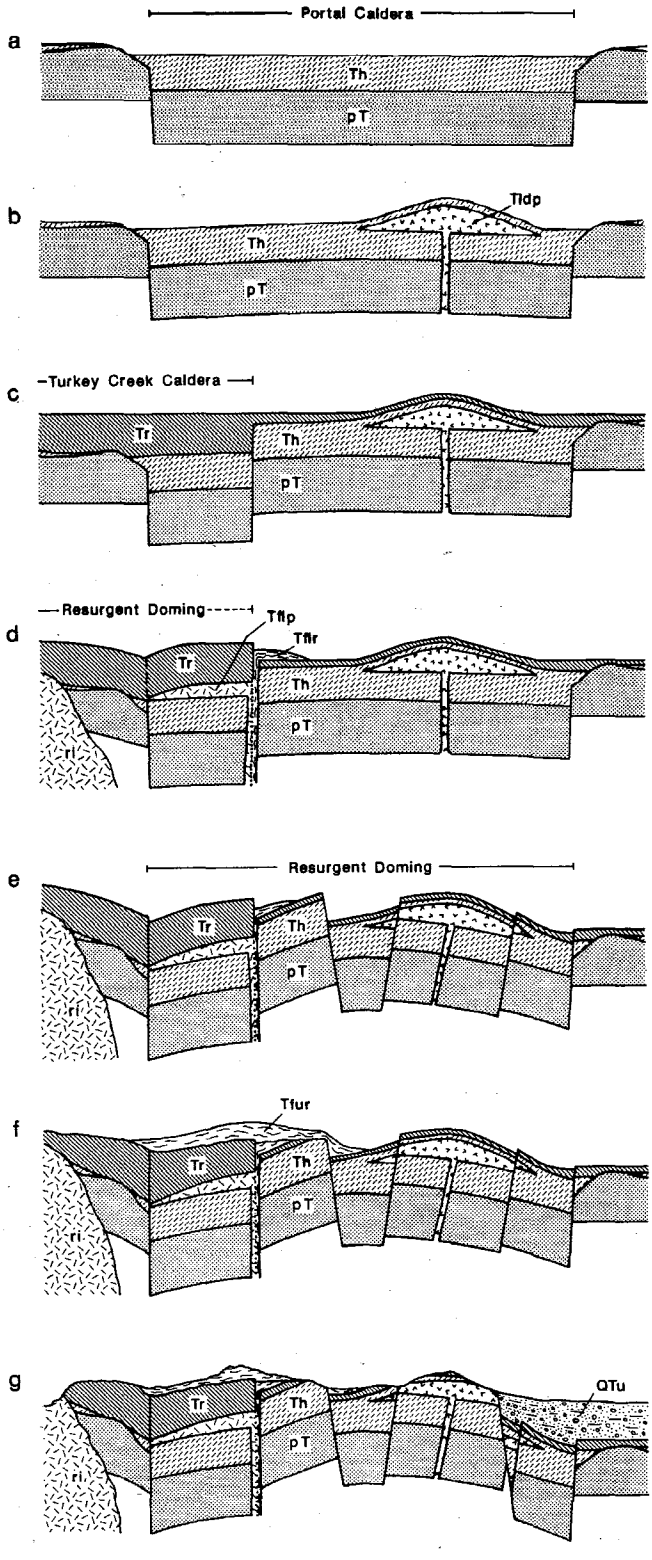

FIGURE 3—Schematic cross sections, showing structural development of the eastern Chiricahuas: **a,** formation of the Portal caldera; **b,** intrusion of the latite of Darnell Peak; **c,** formation of the Turkey Creek caldera; **d,** beginning of resurgence of the Turkey Creek caldera and intrusion of latite porphyry in the zone of overlap that lifts caldera-fill above outflow sheet of Rhyolite Canyon Formation; **e,** resurgent doming of the Portal caldera; **f,** eruption of the upper rhyolite member of the Fife Canyon volcanics; **g,** Basin and Range faulting and erosion produces present-day topography. pT = pre-Tertiary rocks; Th = tuff of Horseshoe Canyon; Tldp = latite of Darnell Peak; Tr = Rhyolite Canyon Formation; Tflp = porphyritic latite member, Fife Canyon volcanics; Tflr = lower rhyolite member, Fife Canyon volcanics; ri = resurgent intrusion; Tfur = upper rhyolite member, Fife Canyon volcanics; QTu = Quaternary deposits, undifferentiated.

Day 1

Mileage

0.0 **STOP 1. Barfoot Lookout** (Buena Vista Peak). Overview of the northern sector of the Portal caldera and precaldera rhyolites of Cave Creek. Backtrack to Onion Saddle. **0.1**

0.1 **Turn left** onto FS-42D. **2.0**

2.1 Onion Saddle. **Turn right** (east) and descend into the Cave Creek drainage. **3.3**

5.4 Paradise Road fork. **Veer right** (uphill) toward Portal, Arizona. **4.1**

9.5 Southwestern Research Station (SWRS) and Herb Martyr road intersection. **Continue straight** (on pavement). **1.2**

10.7 **STOP 2. Outflow sheet of tuff of Horseshoe Canyon.** Pull off on right. Cross meadow on left side of road and examine cliffs on north side of Cave Creek. This is outflow tuff of Horseshoe Canyon, preserved in a downfaulted block along Cave Creek. Equivalent Horseshoe Canyon tuff is exposed high on Portal Peak, and a possible erosional remnant occurs atop Silver Peak to the north (Pallister, written comm. 1988). The Horseshoe Canyon is characterized by sparse quartz (1 mm rounded grains), chalky sanidine (1–2 mm laths), and very sparse biotite. Here, the tuff is densely welded (eutaxitic) and relatively lithic-poor; except for the few biotite grains, it is very similar in outcrop appearance to Rhyolite Canyon tuff. However, the tuff of Horseshoe Canyon is generally more alkaline than the Rhyolite Canyon (compare analyses in Table 1 with those in table 1 of Pallister and du Bray, this volume).

Return to cars and continue down-canyon to east. **0.7**

11.4 Pass Sunny Flat campground (on left). Cliffs above Sunny Flat are rhyolite lava flows of Cave Creek, stratigraphically below the tuff of Horseshoe Canyon. **0.1**

11.5 Pass South Fork Road (FS-42E); **bear left** toward Portal. **4.1**

15.6 Paradise Road junction (FS-42B); **bear right** (continue on pavement). **0.6**

16.2 Portal, Arizona; store and gas station; **continue straight** on main road. **0.7**

16.9 Junction with dirt road to San Simon (just beyond cattleguard); **continue straight** on main road. **5.7**

22.6 Junction with State Line Road (dirt road at cattleguard, also known as Portal Road; sign indicates direction to Douglas and Apache). **Bear right** (south toward Apache) on State Line Road (if very wet, proceed on pavement to US-80; then resume mileage at intersection of US-80 and State Line Road). **4.1**

26.7 Junction with US-80 at Arizona–New Mexico state line. **Continue south** on US-80. **2.35**

29.05 **Turn right** (west) on dirt access road to Horseshoe Canyon. Road is identified by second yellow real-estate sign on right and by mailbox labeled "Zent." Cross cattleguard and old railroad grade, then **veer left at Y** (toward corral and windmill). **2.75**

31.8 Cross old track parallel to mountain front. **0.5**

32.3 **STOP 3. Tuff of Horseshoe Canyon and latite of Darnel Peak.** Corral and gate at mouth of Horse-

shoe Canyon. Park here. The outcrop on the north side of the canyon exposes a fault sliver of the tuff of Horseshoe Canyon in contact with the latite of Darnel Peak. The tuff is exposed at creek level and in the lower part of the outcrop. Eutaxitic texture is poorly developed and the tuff contains large (to 30 cm) mafic and small (3–5 cm) felsic inclusions or fiamme. Outcrops high on the ridge south of the canyon mouth show spectacular mingling between the tuff and the latite sill, suggesting that both were fluid when brought into contact. This area may be close to a feeder zone for the ash-flow tuff. Consider possible origins of the inclusions here. Are the felsic inclusions recrystallized pumices (fiamme) . . . or melt inclusions?

Walk down wash to view exposures of latite sill (latite of Darnel Peak). Latite is also exposed in upper part of outcrop, but watch for loose rocks and rattlesnakes.

Walk through gate and across canyon to south. Exposures here show mingled Horseshoe Canyon tuff with angular felsic inclusions and irregular to angular mafic inclusions in mixed(?) gray matrix.

Return to cars and backtrack to Southwest Research Station.

Day 2

We complete the Portal caldera segment of the field trip in the early morning hours, en-route to the Ash Peak–Rhyolite Peak eruptive complex (Walker and Richter, this volume). Mileage begins at Southwest Research Station. **Follow previous route** from Southwest Research Station, 13.1 mi east (through Portal), **to intersection of Portal Road with State Line Road.**

13.1 **STOP 4. Overview stop** (with low-angle morning light). Good view (to west) of maroon to tan, massive, cliff-forming tuff of Horseshoe Canyon within the Portal caldera. The tuff dips to the south above a very thick section of rhyolite lavas and pyroclastic-flow deposits (rhyolite of Cave Creek) that underlie Portal Peak. The latite of Darnel Peak forms a thick sill within the tuff of Horseshoe Canyon; it is visible along the skyline south of Sulfur Draw.

Continue east on Portal Road, **turn north** on US-80 through Rodeo, New Mexico, and continue to junction with New Mexico Route 9, where the Ash Peak–Rhyolite Peak field-trip road log begins (Walker and Richter, this volume).

Ash Peak–Rhyolite Peak eruptive complex

Robert J. Walker[1] and Don H. Richter[2]

[1]*Radiation Center, Oregon State University, Corvallis, Oregon 97331;* [2]*Box 79, Winston, New Mexico 87943*

Introduction

The early Miocene (23.1 Ma, Richter et al., 1981, 1983) Ash Peak–Rhyolite Peak eruptive complex in southeastern Arizona (Fig. 1) affords an excellent opportunity to observe volcanic features resulting from different modes of rhyolitic and andesitic eruption. The geologic setting is well suited to investigate genetic relations between andesitic and rhyolitic magmas and to speculate on the association of magmatism and mineralization.

Rhyolite magmatism at the Ash Peak eruptive center began with the eruption of moderately crystal-rich, low-silica (73.5% SiO_2) then high-silica (76.2% SiO_2) rhyolite flows and pyroclastics, was followed by nearly aphyric high-silica (76.7% SiO_2) rhyolite flows and domes, and terminated (at the Rhyolite Peak eruptive center) with low-silica (72.6% SiO_2) porphyritic rhyolite flows and domes. Following the close of rhyolitic volcanism at these two centers, extrusion of andesite and basaltic andesite blanketed the area. The basement of the eruptive complex is comprised of basaltic andesite and andesite (51.4–61.7% SiO_2), probably of late Oligocene age (Richter et al., 1983). These andesitic flows are altered, generally oxidized, and amygdaloidal. They characteristically contain anomalously high potassium (to 9% K_2O), apparently concentrated in finely crystalline groundmass K-feldspar, which suggests post-eruption alkali metasomatism. Andesites erupted after the cessation of rhyolitic volcanism are distinctly different from the basement andesitic units. They are unaltered, vesicular, and show no evidence of potassium metasomatism.

Volcanology

Perhaps the most extraordinary volcanic feature at Ash Peak is the exposed interior of a pyroclastic breccia cone and vent plug that marks one of the principal eruptive sites. The interior of the breccia cone provides classic examples of impact structures, base-surge deposits, and epiclastic beds formed by reworking of the deposits between eruptions. Construction of the breccia cone took place relatively early in the rhyolitic cycle, but followed the extrusion of biotite rhyolite and the last of the basement andesite flows. Eruptions that built the pyroclastic breccia cone are interpreted to have been principally Vulcanian (characterized by "moderate to violent ejection of solid or very viscous hot fragments of new lava," Macdonald, 1972).

The base of the cone is composed of pale-yellow, lithic-poor, moderately crystal-rich biotite tuff. The main mass of the cone consists of pale-yellow to orange, pumice-lithic-crystal pyroclastic breccias that are now mostly altered to

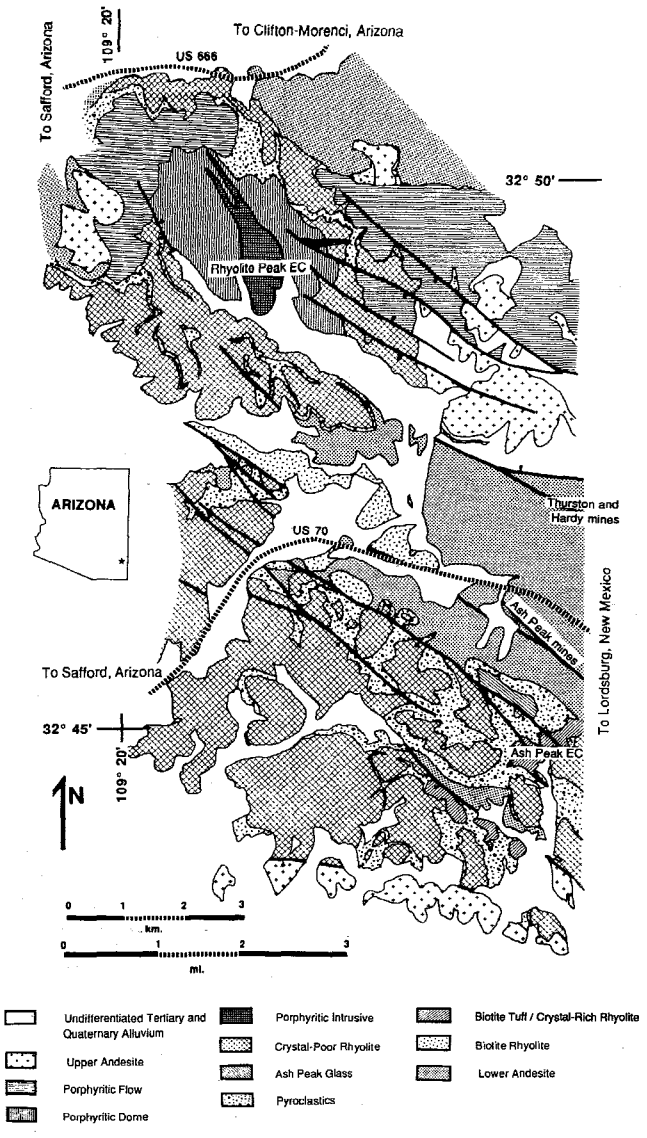

FIGURE 1—Location map and general geology of the Ash Peak–Rhyolite Peak eruptive complex (EC), southeastern Arizona (modified from Richter et al., 1981, 1983).

zeolite (chiefly clinoptilolite, Richter et al., 1981). Thin- to thick-bedded (0.5–3 m) pumice-lithic-crystal pyroclastic-breccia layers become finer-grained and pinch out over a distance of 3 km from the central vent. Intercalated with the early pyroclastic breccias and forming the vent plug are crystal-rich rhyolite flows and peripheral domes. Slope angles and the inferred basal diameter indicate that the pyroclastic-breccia cone was at least 200 m high. The upper portion of the cone preserves a pronounced angular discordance with overlying pyroclastic layers dipping inward toward the vent. This discordance has been interpreted to indicate that the principal vent varied in location during the construction of the cone (Richter et al., 1981). With the change in vent location, new eruptions blasted out pre-existing material forming a summit crater. Subsequent eruptions filled the crater with material and deposited tephra on the inward-dipping surface.

Sparse, thin, poorly welded ash-flow horizons are interlayered with the thin- to thick-bedded breccias. Ash layers, accretionary lapilli, agglutinate, and epiclastic beds are minor components of the pyroclastic-breccia cone; all are generally altered to clinoptilolite (Richter et al., 1981).

The enigmatic Ash Peak Glass covers the west side of the pyroclastic cone. It is approximately 30 m thick, with a pumiceous basal breccia and a vitric upper zone containing a central zone of large spherulites. From near the summit of Ash Peak, the unit extends 1.2 km to the west and 1.8 km to the southwest, where it is entirely vitric and 4–5 m thick. The thickness and aspect ratio of the Ash Peak Glass, its glassy character, and presence of sparse lithic clasts suggests that it was not the product of a typical flow-dome building eruption. Available evidence suggests that the Ash Peak Glass is in fact an agglutinate formed by a Strombolian-type eruption of silicic magma following the construction of the major part of the pyroclastic cone.

Petrology and geochemistry

The Ash Peak–Rhyolite Peak eruptive complex provides an ideal example of trace-element immobility, despite extensive zeolitic alteration. Rhyolitic rocks associated with the Ash Peak eruptive center have been classified into five litho-chemical groups based on distinctive petrologic and/or geochemical characteristics. The five litho-chemical groups, from earliest to latest, are: biotite rhyolite, biotite tuff/crystal-rich rhyolite (BioT/Xtal-R), pyroclastics, Ash Peak Glass, and crystal-poor rhyolite.

The biotite rhyolite is moderately crystal-rich, biotite-bearing, usually vitric rhyolite. This unit represents the earliest rhyolitic flows in the area and locally is intercalated with the basement andesite. Samples of biotite rhyolite exhibit the most primitive geochemical signatures of the rhyolites analyzed in the Ash Peak area (Fig. 2).

Biotite tuff and crystal-rich rhyolites (up to 10% phenocrysts, dominantly sanidine) are petrologically dissimilar, but geochemically identical, rock types that stratigraphically and geochemically follow biotite rhyolite (Fig. 2). Chemical evidence for their consanguinity provides the basis for classification as a single litho-chemical group.

Chemical analyses have not been obtained on the pumice of the pumice-lithic-crystal pyroclastic breccias that make up the breccia cone. However, their stratigraphic position suggests that they post-date eruption of BioT/Xtal-R and mostly pre-date eruption of the Ash Peak Glass.

The litho-chemical group classified as the Ash Peak Glass has a complicated chemistry, exemplified by data from the

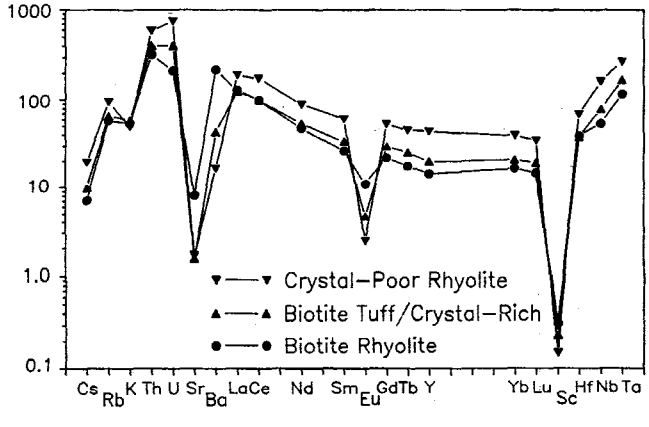

FIGURE 2—Cl chondrite-normalized geochemical patterns of principal rhyolite types associated with the Ash Peak eruptive center (Gd interpolated between Sm and Tb).

thick vitric mass forming the western shoulder of Ash Peak. Trace-element patterns are intermediate between BioT/Xtal-R rhyolite and crystal-poor rhyolite, although they are strongly depleted in light rare-earth elements (LREE) as shown in Fig. 3. Abundances of La, Ce, and Nd in the Ash Peak Glass are less than those of biotite rhyolite.

The latest and most voluminous rhyolites associated with the Ash Peak eruptive center are crystal-poor to aphyric, high-silica rhyolite flows and domes. These rocks are the most evolved geochemically; they exhibit the highest concentrations of incompatible elements (REE, U, Th, Rb, Nb, and Ta) and the lowest abundances of compatible elements (Ba, Sr, Eu, and Sc) (Fig. 2).

Despite differences in their macro- and microscopic appearance, the lower and upper andesites exhibit virtually identical trace-element patterns (Walker, 1988). With regard to trace-element abundances, the andesites are significantly higher in total REE than the early formed rhyolites (Fig. 4). Using available partition coefficients and appropriate liquidus mineralogies, it is not possible to form the Ash Peak rhyolites either by crystal fractionation or by partial melting of the last erupted basement andesites.

Assuming a parent magma of approximately biotite rhyolite composition, the other groups of rhyolite can be generated by simple incremental crystal-fractionation models. The fractionation trend from biotite rhyolite to crystal-poor rhyolite shows compatible-element depletion coupled with incompatible-element enrichment. Observed phenocryst mineralogies and modes were used to model the proportions of the liquidus constituents. Partition coefficients were taken from the available literature (Mahood and Hildreth, 1983; Nash and Crecraft, 1985). Modeled liquids, using 18 elements, match the analytical data for the various litho-chemical groups within experimental error (Walker, 1988).

Mineralization

In addition to lending its name to the eruptive complex, Ash Peak also refers to the mining district encompassing the mines, prospects, and claims to the north and east. The most important producers of the district are the shafts and declines located along the Ash Peak vein, approximately 0.8 km northeast of Ash Peak. The vein consists of silica and lesser carbonate replacement and fracture fillings in a northwest-trending fault zone that crosscuts basement andesite. Since the beginning of the century, mining has been intermittent, with silver (approximately 97,000 kg) as the most important commodity. In addition, minor amounts of gold, copper, and lead have been recovered (Lines, 1940). Today, silica is extracted for use as a flux by the various smelters servicing the large porphyry copper deposits of Arizona and New Mexico. The expense of transporting the silica is offset by recovery of the precious metals during smelting. North and east of Ash Peak, epithermal calcite–manganese-oxide veins were exploited, especially during wartime. Development is restricted to a number of shallow trenches and shafts (maximum depth 26 m) with beneficiation of the ore by hand-cobbing methods. Total production of nearly 1700 metric tons of 40% Mn ore has been reported (Wilson and Butler, 1930; Richter and Lawrence, 1983).

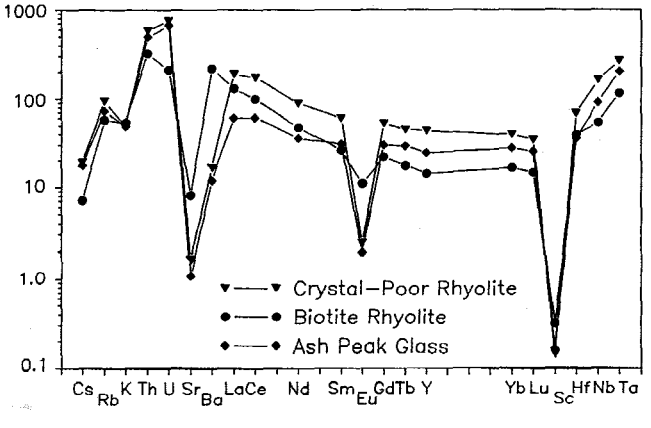

FIGURE 3—Cl chondrite-normalized geochemical pattern of the Ash Peak Glass and its relationship to other rhyolites associated with the Ash Peak eruptive center (Gd interpolated between Sm and Tb).

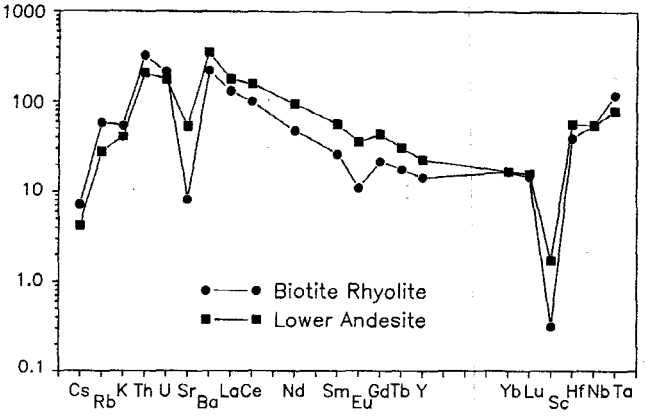

FIGURE 4—Cl chondrite-normalized geochemical patterns of the last-erupted andesite and first-erupted rhyolite (Gd interpolated between Sm and Tb).

Work in progress suggests that the manganese ore-forming solutions may have been derived in part from residual fluids concentrated during the last stages of crystallization of the rhyolite magma. Late-stage magmatic fluids, possibly in conjunction with meteoric waters, may have interacted with the nearly solidified magma before mixing with meteoric waters and migrating to the fracture zones. Elevated LREE patterns similar to those of the crystal-poor rhyolites, negative Ce anomalies, slight positive Eu anomalies, and very high concentrations of Ba, As, and Sb support this hypothesis. Although definitive chemical evidence is lacking, a similar genesis is postulated for the formation of the precious metal–silica veins at Ash Peak. The Ash Peak veins may represent a deeper level of exposure of the nearer-surface calcite–manganese-oxide system.

In addition, very thin and discontinuous veinlets of cassiterite and hematite occur in rhyolites of the Rhyolite Peak eruptive center. These occurrences of tin do not appear to be economically significant. However, their presence suggests the possibility of tin, tungsten, and/or molybdenum stockwork or porphyry-type deposits at depth.

Discussion

Local intercalations of the last erupted andesites and first-erupted rhyolites, elevated trace-element abundances in andesite relative to rhyolite, and xenoliths with anatectic textures from rhyolite associated with the Rhyolite Peak eruptive center suggest that two different magmatic systems produced the andesites and the rhyolites. These data indicate that the rhyolites formed from partial melting of preexisting (Cre-

taceous–early Tertiary?) basaltic andesites rather than from modification of the middle Tertiary basement andesites (Walker and Richter, 1987).

The changes from andesitic to rhyolitic and back to andesitic volcanism may be in part due to major changes in the local tectonic regime (Gans, 1987; Gans et al., 1987). Deep crustal extension associated with the formation of the Pinaleno Mountains metamorphic core complex may have permitted basaltic magma to rise rapidly through the crust and act as a heat source for partial melting, rather than fractionating to andesite during a slower ascent (Walker and Richter, 1987). By changing the tectonic regime, parental basalts may either fractionate to intermediate compositions or act as heat sources for partial melting. This theory allows the lower and upper andesite to have the same geochemical signature despite their separation by large volumes of rhyolite and considerable time. Alternatively, a shallow crustal reservoir of silicic magma may have provided a "shadow zone" free of more mafic volcanism during the main rhyolitic episode, as suggested for several Pleistocene volcanic centers (Bacon, 1985).

Road log

This trip focuses primarily on the Ash Peak silicic eruptive complex in the northern Peloncillo Mountains approximately 60 mi north of the Southwest Research Station (SWRS) in Portal, Arizona. During the course of the trip we will cross and then roughly parallel the east side of the Peloncillo Mountains. With the exception of a relatively small area in the central Peloncillo Mountains, the entire range is underlain by middle Tertiary (35 to 25 Ma) volcanic rocks that range in composition from basalt to high-silica rhyolite (Drewes et al., 1985). Minor late Tertiary (6–2 Ma) activity has produced a few small-volume alkali basalt flows. Most of the volcanic rocks are products of rift eruptions, composite volcanoes, and dome-flow complexes; one shallow volcanic caldera, the 34–35 Ma Steins caldera, contains a thick section of densely welded intracaldera tuff and is outlined by a series of rhyolite domes (Richter et al., 1988).

The area of the Peloncillo Mountains not underlain by middle Tertiary volcanic rocks, between Granite Gap and Stein's Pass, exposes a sequence of Precambrian granitic rocks, Paleozoic sedimentary rocks, and Mesozoic sedimentary and volcanic rocks intruded by an Oligocene granitic pluton.

Mileage

0.0 Intersection of US-80 and NM-9, 5 mi north of Rodeo, New Mexico. **Drive north on US-80. 13.4**

13.4 Granite Gap. An 8 km^2 Oligocene (~32 Ma) quartz monzonite pluton is exposed in the roadcut. Small base-metal vein and replacement deposits (Cu–Pb–Zn–Ag ores) and scheelite-bearing skarns replace Paleozoic limestones proximal to the Granite Gap pluton. Mineralization is spacially associated with quartz monzonite or dacite porphyry dikes, which are chemically similar to, and probably comagmatic with, the Granite Gap pluton (Williams, 1978). **11.2**

24.6 At the small community and truck stop of Road Forks we **turn east** on I-10 and begin to cross the broad Animas Valley. Like many of the basins in the southern Basin and Range province with interior drainage systems, the Animas Valley contains a number of alkali playa lakes. **17.5**

42.1 **Leave I-10 at exit 22 and turn north on US-70** through the city of Lordsburg, New Mexico. Lordsburg, county seat of Hidalgo County, was the main residential and support community for the mines in the Lordsburg mining district to the southwest, which has produced more than 60 million dollars, chiefly in gold, silver, and copper. The mines have been inactive since 1975. The deposits are fissure-fillings along prominent northeast- and east-trending faults that transect the contact zone of a porphyritic granodionite pluton (56–59 Ma) which intrudes a sequence of Late Cretaceous andesite flows and breccias (Richter and Lawrence, 1983). **2.8**

44.9 **Veer left a Y-intersection** and continue driving northwest on US-70. Continue on US-70, off the Lordsburg Mesa, and into Duncan, Arizona, on the modern flood plain of the Gila River. Cliffs along the highway expose the Gila Conglomerate, a 2–20 Ma sequence of moderately indurated alluvial silt, sand, gravel, and conglomerate that is locally tuffaceous. **Continue through Duncan on US-70** and climb out of Gila River valley, through excellent exposures of Gila Conglomerate, and into the foothills of the northern Peloncillo Mountains. Roadcuts 10 mi west of Duncan expose massive andesite flows that pre-date the rhyolite eruptives at Ash Peak–Rhyolite Peak. **45.4**

90.3 **STOP 1. Ash Peak Mines. Turn left (south) off US-70** onto the dirt Ash Peak mines road; **continue about 0.5 mi to mine workings** for a brief discussion of the deposit. Future guidebook users: this area is posted and blasting is possible; **obtain permission before entering. Continue about 0.5 mi** on barely visible dirt road to broad saddle on east flank of Ash Peak. From here, a 1–3 mi hike (take lunch) will take us onto the pyroclastic cone of Ash Peak where we will examine the pyroclastic deposits of the breccia cone, and contemplate eruptive mechanisms for the Ash Peak Glass.

The walk begins on amygdaloidal basement andesite that underlies the cone. We cross a wide rhyolite dike, showing vertical flow-banding, then traverse the lower pyroclastic beds of the cone. From here to the eroded crater of the cone (on the east shoulder of Ash Peak), surge beds, bomb sags, and accretionary lapilli can be seen in a variety of pyroclastic-flow and air-fall deposits. At the crater, a prominent angular unconformity between outward-dipping cone deposits and inward-dipping vent deposits is well exposed. An irregular rhyolite plug is exposed in the eroded base of the crater.

The more adventuresome may hike up through more cone deposits to the Ash Peak Glass, about 100 m above the crater.

Geology and petrology of basalts and included mafic, ultramafic, and granulitic xenoliths of the Geronimo volcanic field, southeastern Arizona

Pamela D. Kempton[1] and Mike A. Dungan[2]

[1]*Department of Earth Sciences, The Open University, Milton Keynes, England MK7 6AA;*
[2]*Department of Geological Sciences, Southern Methodist University, Dallas, Texas 75275*

Introduction

In this paper, we review the geology and petrology of a type example of alkaline (as opposed to calc-alkaline; see Sawyer and Pallister, this volume) Basin and Range volcanism, the basaltic Geronimo volcanic field (GVF). Aspects that will be discussed are: (1) a general geologic overview of the volcanic field, (2) magmatic evolution of the Geronimo basalts, (3) petrogenesis of Type II ultramafic xenoliths and relationships to their host basalts, (4) magma/mantle interactions or mantle-enrichment processes in the sub-Geronimo mantle, and (5) petrology of GVF lower crustal granulites and evolution of the lower crust. More detailed discussion of each of these topics can be found in Kempton (1984, 1987), Kempton et al. (1984, 1987), and Menzies et al. (1985).

Geologic overview of the Geronimo volcanic field

The GVF is located in a Basin and Range graben at the intersection of the San Bernardino Valley with the San Simon Valley (Fig. 1). Although the San Bernardino Valley is several hundred kilometers in length, Pleistocene and Pliocene volcanic activity is localized for the most part at the intersection of the north–south-trending Basin and Range faults with the older northwest–southwest-trending structures (Fig. 2). It has been suggested that a preferred alignment of cinder cones parallel to the north–south-oriented, graben-bounding faults indicates the presence of concealed faults having similar orientations throughout the valley (Drewes, 1981; Lynch, 1978).

Most of the southern Arizona Basin and Range is tectonically quiescent, but the San Bernardino Valley has been historically active (Herd and McMasters, 1982; Drewes, 1981). Initiation of block faulting was probably coincident with the voluminous rhyolite extrusions which form a large part of the graben-bounding mountains, but the most recent reported activity was in 1887 when an earthquake resulted in the formation of a 76 km long, high-angle fault scarp along the southern extension of the valley (Aguillera, 1888; Herd and McMasters, 1982). As a result of concurrent faulting and volcanism, GVF basalts exposed on the flanks of the valley are older (3.5–9 Ma) and less voluminous than those on the valley floor (0.26–3.6 Ma; see Fig. 2) (Kempton et al., 1987).

Two lava groups are recognized on the basis of chemical and petrographic characteristics, as well as by physiographic and age distribution. *Flank lavas* are alkali olivine basalts, hawaiites, and mugearites; they are generally more evolved (Mg values range from 0.31 to 0.63), are relatively low in alkalis, and have low normative Ne contents (0–7 wt%) (Table 1). They also contain relatively few ultramafic xen-

TABLE 1—Major-element compositions of representative GVF basalts.

	Valley basalts				Flank basalts				
	Basanites			Nepheline Hawaiite	Alkali olivine basalt	Hawaiite	Mugearite		
Sample	D2[1, 8]	pk-G-22[2, 9]	Cochise maar[3, 9]	pk-G-66[4, 8]	D3[5, 8]	pk-G-63[6, 8]	pk-G-58[7]	Avg. valley	Avg. flank
SiO_2	45.75	45.12	44.93	47.29	46.67	48.74	52.48	46.29	47.93
TiO_2	2.16	2.05	2.32	1.89	2.20	2.57	1.48	2.23	2.11
Al_2O_3	16.18	16.32	16.29	16.67	15.64	16.79	17.35	15.89	16.08
Fe_2O_3	11.10	10.60	10.83	10.90	11.71	12.19	10.07	11.35	11.58
MnO	0.19	0.22	0.19	0.20	0.18	0.22	0.21	0.18	0.18
MgO	7.83	8.88	7.59	6.16	8.73	3.42	1.99	8.07	7.18
CaO	8.86	8.56	9.11	7.55	9.11	6.98	4.88	8.97	8.43
Na_2O	4.30	4.46	4.54	4.74	3.99	4.31	4.76	3.76	3.47
K_2O	2.13	2.55	2.20	2.66	0.85	2.15	3.11	1.90	1.52
P_2O_5	0.71	0.42	0.55	0.69	0.52	1.06	0.60	0.59	0.53
H_2O	0.85	0.74	0.91	—	1.10	1.43	1.73	—	—
Total	100.06	99.92	98.75	98.74	100.70	99.86	98.66	99.22	99.04
$Mg/(Mg+0.9\ Fe^{+2})$	0.61	0.65	0.61	0.55	0.62	0.38	0.30	0.61	0.58
Normative Ne	12.3	16.8	15.7	11.8	5.6	0.98	(Hy = 2.89)	7.9	1.0

[1]Dated basanite flow from Stop 1B, this road log; NW of Krentz Ranch, 31°40′N 109°18′W.
[2]Basaltic bomb from xenolith-bearing cone 1.5 mi SE of US Hwy 80, Stop 2A, this road log, 31°31′N 109°17′W.
[3]Maar ~4.5 mi SE of US Hwy 80, 31°27′N 109°16′W.
[4]Flow ~2 mi NW of Geronimo Trail, 31°23′N 109°17′W.
[5]Flow south of Mulberry Canyon, Pedregosa Mountains, 31°37′N 109°19′W.
[6]Mesa-capping flow, east side of Skeleton Canyon, Peloncillo Mountains, 31°35′N 109°04′W.
[7]Flow ~2 mi NE of Fairchild Ranch, Peloncillo Mountains, 31°32′N 109°06′W; average of analyses by 8 and 9.
[8]Analysts J. G. Fitton and D. James, University of Edinburgh; H_2O analyses by P. Kempton, NASA-JSC.
[9]Analyst P. Kempton, NASA-JSC (XRF).
Concentrations reported in wt%.

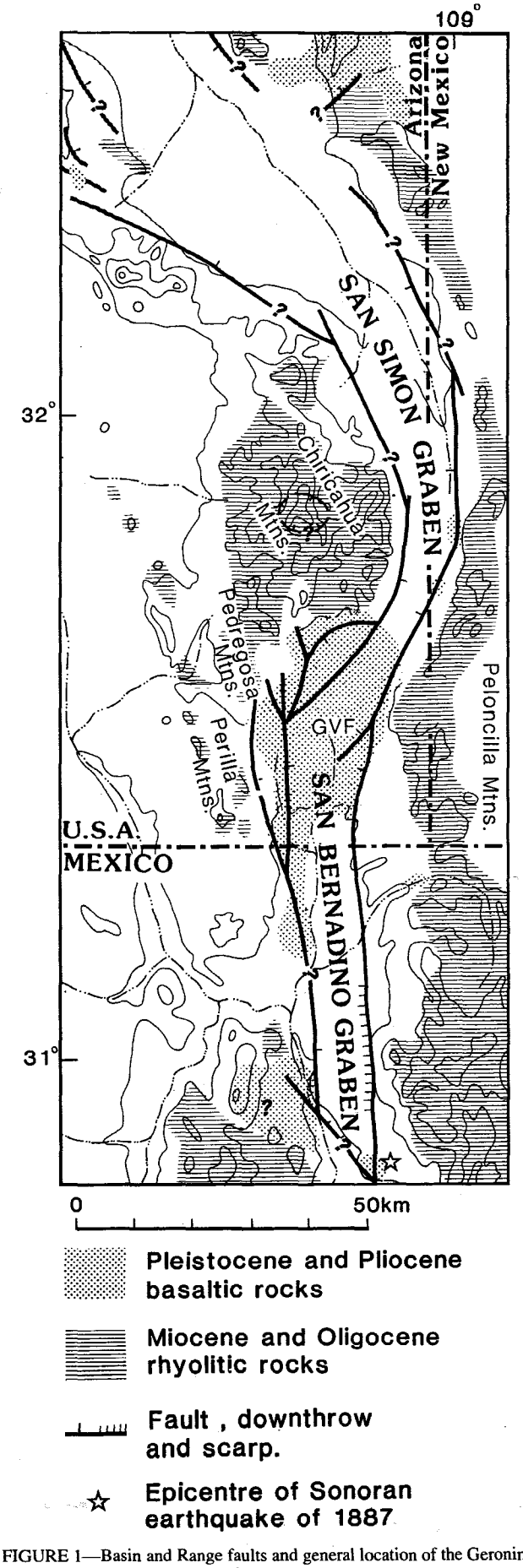

FIGURE 1—Basin and Range faults and general location of the Geronimo volcanic field. After Drewes (1981).

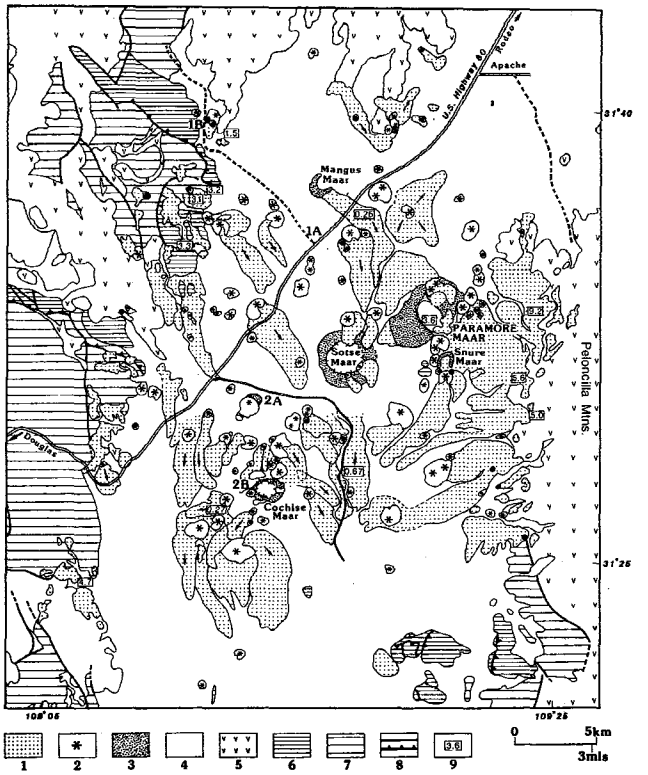

FIGURE 2—Geologic map of the Geronimo volcanic field. (1) GVF lava flows, (2) GVF cinder cones, (3) GVF pyroclastic units surrounding maars, (4) Quaternary alluvium, (5) Tertiary rhyolite and associated volcanic rocks, (6) Paleozoic sedimentary rocks, undifferentiated, (7) Mesozoic sedimentary and volcanic rocks, undifferentiated, (8) fault, (9) locations of dated GVF samples and age. Stratigraphy and distribution of rocks older than GVF volcanics generalized from Cooper (1959).

oliths, although megacrysts of plagioclase and anorthoclase and small felspathic xenoliths are common. Megacrysts of aluminous augite, spinel, olivine, orthopyroxene, and apatite occur less commonly. In contrast, the younger *valley lavas* are more strongly silica-undersaturated basanites and nepheline hawaiites; normative nepheline contents range from 5 to 18 wt% (Table 1). They exhibit a more limited range and include generally higher average Mg values (0.53–0.68), many of which are within the range for liquids calculated to be in equilibrium with mantle olivine compositions. Mafic, ultramafic and granulitic xenoliths, up to 45 cm in diameter, are common and locally abundant. Megacrysts of aluminous augite, olivine, spinel, plagioclase, and anorthoclase occur in most flows. In contrast to flank lavas where feldspar megacrysts predominate, augite and spinel are most common in valley basalts. Locally, amphibole and apatite are abundant.

In general, GVF alkali olivine basalts of the flank-lava group are fine-grained, porphyritic or microporphyritic rocks with groundmass textures ranging from intergranular to intersertal (Fig. 3a). Phenocrysts of plagioclase and olivine up to 2 mm in size are common, while clinopyroxene is generally confined to the groundmass. In contrast, the younger valley lavas are finer-grained and textures range from glassy to intersertal; less commonly, they have intergranular textures (Fig. 3b). Phenocrysts or microphenocrysts of plagioclase and olivine occur in the valley lavas, but clinopyroxene is far more abundant modally, both in the groundmass and as a phenocryst phase, than in flank lavas.

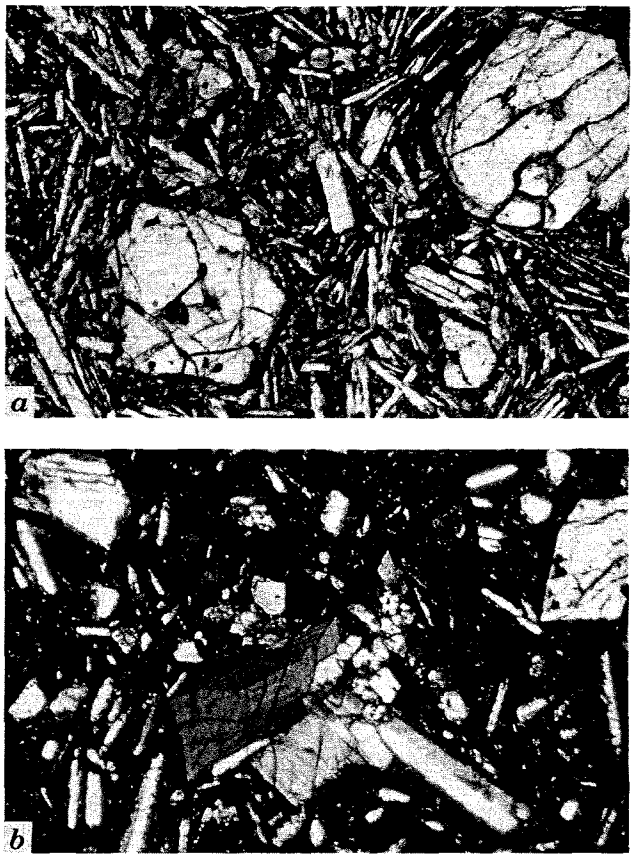

FIGURE 3—Photomicrographs of GVF flank and valley basalts. **a**, Sample pk-G-50, flank basanite; fine-grained, olivine + plagioclase microporphyry. **b**, sample 90-7, valley basanite; fine-grained, plagioclase + olivine + clinopyroxene microporphyry. Note sector zoning in clinopyroxene. Field of view 2.6 mm.

Magmatic evolution of the Geronimo volcanic field

Major-element mass-balance calculations and trace-element modeling (Kempton et al., 1987) indicate that flank basalts and some valley basalts record the effects of significant polybaric fractional crystallization that occurred as these magmas established conduits to the surface. These calculations demonstrate that low-pressure fractional crystallization alone cannot account for the compositional variations in relatively evolved lavas. Instead, fractionation of aluminous clinopyroxene + spinel ± olivine at moderate pressures, coupled with additional fractionation of kaersutite or plagioclase and Na- and Fe-rich pyroxene at lower pressure could have generated the compositional spectrum (see Table 1 and Kempton et al., 1987, for a summary of GVF basalt chemistry).

Conventional magma reservoirs did not exist within the crust beneath GVF. Instead, fractional crystallization took place by crystal plating against the walls of conduits as magmas ascended to the surface. Such interactions between alkalic basalts and conduit walls are recorded by crosscutting intrusive relations in composite xenoliths from GVF. The mineral assemblages and the relative proportions of phases subtracted in GVF mass-balance calculations are generally the same for evolved lavas from both flank and valley groups, regardless of the initial normative nepheline content (Kempton et al., 1987). These modal proportions are also similar to the relative abundance of these phases in Type II (aluminous augite group, see below) xenoliths. This suggests that these modal assemblages reflect cotectic proportions.

Although it has been generally maintained that basaltic rocks with greater than 5% normative nepheline fractionate to more silica-undersaturated compositions, away from the critical plane of silica undersaturation (Coombs and Wilkinson, 1969; Macdonald and Katsura, 1964), the cumulative effect of fractionating the described assemblages is to decrease the degree of undersaturation in the melt. This is primarily due to crystallization of spinel. At lower pressures where plagioclase crystallizes with olivine and clinopyroxene from alkalic basalt melts instead of spinel, fractionation could produce increasing silica undersaturation of the melt. However, fractionation of clinopyroxene + spinel + olivine from GVF alkali olivine basalts and basanites at moderate pressures results in decreasing silica undersaturation.

Petrogenesis of aluminous clinopyroxenites and amphibole peridotites

The majority of mantle-derived xenoliths included in alkalic basalts can be divided into two groups, the Cr-diopside series, or Type I, and the Al-augite series, or Type II (Wilshire and Shervais, 1975; Frey and Prinz, 1978). Type I xenoliths are generally regarded as the mantle source rocks to alkali basalts and their parent magmas. Type II xenoliths are thought to represent the mantle-level crystallization products of alkali basalts. The "type" terminology is adopted here, but the two groups are further subdivided to include the subgroups Type Ia, with light rare-earth elements/heavy rare-earth elements (LREE/HREE) in clinopyroxene <1, and Type Ib, with LREE/HREE in clinopyroxene >1) as defined by Kempton et al. (1984), and subgroups Type IIa and Type IIb as defined below.

In general, Type II xenoliths are more enriched in Fe, Al, Ti, and incompatible trace elements than Type I spinel lherzolites, and they exhibit a much greater spectrum of petrographic and chemical characteristics. Primary mineral phases in Type II xenoliths are aluminous augite + Al-spinel ± olivine, kaersutite, phlogopite, apatite, plagioclase, orthopyroxene, magnetite, and Fe-sulfides. Secondary glass, produced by the breakdown of clinopyroxene or amphibole, and rhönite, produced during the breakdown of amphibole or phlogopite, may also be present. Type II xenoliths present at GVF include clinopyroxenite, wehrlite, kaersutite peridotite, and rare websterite.

The spectrum of textural and chemical varieties of Type II xenoliths at GVF can be subdivided into two major groups. *Type IIa* inclusions have igneous textures in which clinopyroxene varies from irregularly shaped grains occurring with more equant olivine, to large poikilitic crystals which totally enclose olivine and spinel. Amphibole rarely occurs, except as minute patches replacing clinopyroxene, and only one spinel phase (pleonaste) is present. Exsolution of aluminous spinel from Type IIa clinopyroxene is characteristic (Fig. 4a); exsolution of orthopyroxene occurs, but is far less common. Relative to other Type II xenoliths, Type IIa peridotites have lower LREE/HREE and total Al_2O_3, but higher CaO, MgO, Sc, Cr and tetrahedral aluminum (Table 2).

Textures of anhydrous *Type IIb* mineral assemblages are essentially granoblastic (Fig. 4b). Crystals are equant in shape and grain boundaries are subplanar. Poikilitic relationships are uncommon. Clinopyroxene is characteristically free of both spinel and orthopyroxene exsolution. In addition, these xenoliths contain two spinel minerals, mag-

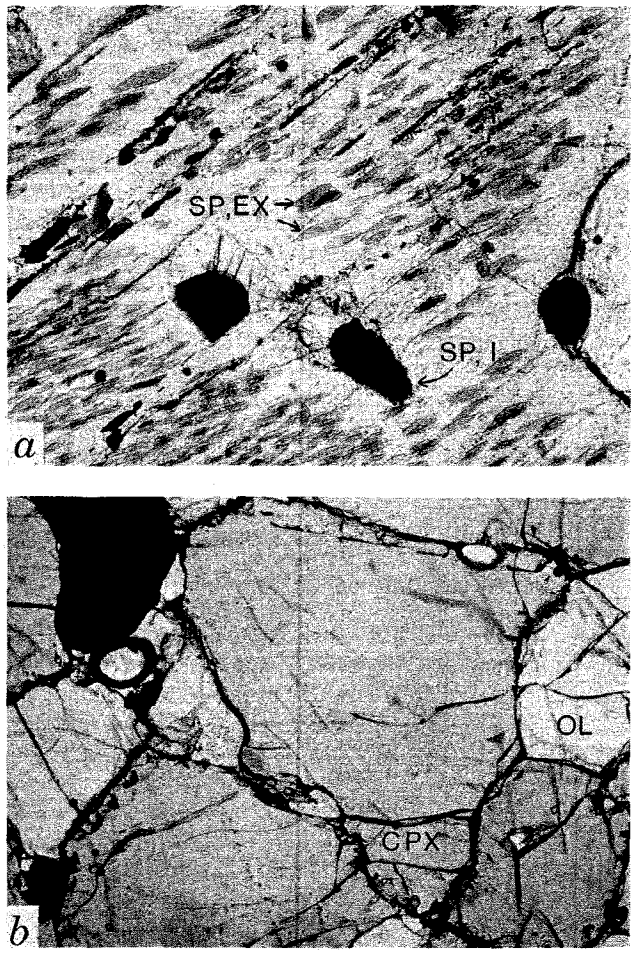

FIGURE 4—**a,** Photomicrograph of sample 20-5 from locality pk-G-20. Type IIa clinopyroxenite with abundant exsolution of spinel platelets (SP, EX) and spinel inclusions (SP, I). Uncrossed polars. Width of field 1.3 mm. **b,** Photomicrograph of sample 23B-7 from locality pk-G-23b. Type IIb olivine clinopyroxenite. Photomicrograph shows lack of exsolution in clinopyroxene phase. Uncrossed polars. CPX = clinopyroxene, OL = olivine. Width of field 2.6 mm.

TABLE 2—Major- and trace-element compositions of representative type II clinopyroxenes and amphiboles, GVF.

Sample	20-5[1]	20-8[2]	22-11[3]	23-M3[4]	22-11[5]	22-16[6]
SiO_2	49.17	47.80	47.56	47.02	40.10	42.52
TiO_2	1.38	1.98	1.88	2.02	6.11	3.44
Al_2O_3	6.38	8.93	9.04	9.46	14.54	14.78
FeO	5.68	7.86	7.21	7.46	9.29	5.79
MnO	0.16	0.17	0.16	0.20	0.15	0.10
MgO	14.23	12.84	12.88	12.88	13.28	16.44
CaO	22.54	19.26	19.43	19.75	10.97	10.33
Na_2O	0.53	1.33	1.31	1.34	2.58	3.35
K_2O	—	—	—	—	1.60	1.05
F	—	—	—	—	0.30	n.d.
H_2O	—	—	—	—	1.29	n.d.
Total	100.07	100.17	99.47	100.13	100.21	97.80
$Mg/(Mg+Fe^{+2})$	0.87	0.79	0.81	0.84	0.72	0.84
Al^{IV}/Al^{VI}	2.21	1.46	1.43	1.67	6.58	3.39
La	2.7	3.8	5.9	4.9	5.5	6.3
Ce	12	15	17	17	15	31
Nd	13	16	16	16	21	21
Sm	3.79	4.97	4.56	4.99	4.68	5.91
Eu	1.5	1.4	1.7	1.5	1.4	1.0
Tb	0.80	0.78	0.75	0.81	0.79	1.15
Yb	2.1	2.2	1.6	1.9	1.5	3.1
Lu	0.26	0.17	0.14	0.29	0.14	0.14
Cr	1800	60	100	47	90	1200
Ni	135	35	49	58	61	680
Sc	72	55	58	63	54	43
La/Yb	1.29	1.73	3.69	2.58	2.03	3.67

[1]Clinopyroxene from Type IIa anhydrous clinopyroxenite, from small spatter cone, pk-G-20, south of Cochise maar. 31°27'N 109°16'W.
[2]Clinopyroxene from Type IIb anhydrous clinopyroxenite. Same location as 1 above.
[3]Clinopyroxene from Type IIb amphibole-bearing clinopyroxenite. Sample location pk-G-22, ~1.5 mi SE of US Hwy 80. 31°31'N 109°17'W.
[4]Clinopyroxene megacryst from locality pk-G-23. Cinder cone ~1.5 mi SW of Cochise maar. 31°27'N 109°18'W.
[5]Vein amphibole attached to spinel lherzolite xenolith. Sample location pk-G-22.
[6]Amphibole from Type IIb hydrous clinopyroxenite. Same sample as 3 above.

Major elements reported in wt%. Analyst P. D. Kempton, Southern Methodist University (microprobe). Trace elements reported in ppm. Analyst P. D. Kempton, NASA-JSC (INAA).

netite, and pleonaste. Fe-sulfide globules are usually present as inclusions in all other mineral phases. Compositionally, they have higher LREE/HREE and total Al_2O_3, but lower CaO, MgO, Sc, Cr, and tetrahedral aluminum (Table 3).

Amphiboles can be found in both Type IIa and Type IIb xenoliths, but it is in xenoliths with textural and compositional characteristics of Type IIb that large poikilitic kaersutite amphibole crystals occur. These single, optically continuous crystals are commonly several centimeters in size and are observed in thin section enclosing or replacing clinopyroxenes of varying crystallographic orientations (Fig. 5a). Contacts between clinopyroxene and kaersutite may occur as distinct grain boundaries or as lobate replacement interfaces (Fig. 5b). Compositional zonation of clinopyroxene (depletion in Al_2O_3 and TiO_2 and enrichment in FeO) is observed adjacent to these contacts. Magnetite and Fe-sulfide globules are always present in Type IIb amphibole peridotites from GVF. The Fe-sulfides occur predominantly as spherical inclusions in amphibole, but may be found in clinopyroxene, olivine or spinel as well. Rhönite is present in trace amounts in most amphibole-bearing peridotites from GVF. It occurs as small prisms, in association with Ti-augite, olivine, Fe–Ti oxides, and glass, generally less than 150 μm in size, but crystals as large as 500 μm have been observed.

Amphibole and mica also occur as selvages or as discrete interstitial crystals in Type I xenoliths. Major-element compositions of amphiboles vary as a function of occurrence, such that amphibole megacrysts and Type II peridotite amphiboles are highest in FeO (9–10 wt%), while amphiboles associated with Type I xenoliths have FeO contents as low as 3.5 wt% (Table 2). Cr and Ni concentrations are generally low (less than 400 ppm Cr, 190 ppm Ni) except in amphibole associated with Type I lherzolites, where Cr_2O_3 concentrations may be as high as 1.4 wt% and Ni ranges from 650 to 700 ppm.

Some Type II xenoliths recrystallized subsequent to formation. In sample pk-G-21-4, a partially recrystallized Type IIa clinopyroxenite, the primary igneous clinopyroxene exhibits typical exsolution of spinel platelets (Fig. 6a). In recrystallized clinopyroxene, the spinel habit is more rod-like but maintains essentially the same orientation developed during exsolution of the primary clinopyroxene. Patches of amphibole replacing primary and recrystallized clinopyrox-

TABLE 3—Major- and trace-element compositions of representative GVF granulite xenoliths.

	GN21-6[1]	GN21-4[2]	GN42-2[3]	GN22-1[4]	GN22-5[5]
SiO_2	51.91	53.99	45.68	57.50	73.15
TiO_2	0.26	0.96	2.75	0.84	0.46
Al_2O_3	22.30	20.13	14.99	17.26	12.77
Fe_2O_3	4.29	7.63	11.82	6.91	2.92
MnO	0.07	0.14	0.17	0.10	0.06
MgO	5.28	3.93	8.75	4.01	0.76
CaO	11.32	7.40	11.08	6.40	1.95
Na_2O	3.69	4.68	3.02	4.15	2.77
K_2O	0.28	0.83	0.79	2.07	3.38
P_2O_5	0.03	0.30	0.17	0.22	0.10
Total	99.43	99.99	99.22	99.46	98.32
$Mg/(Mg+0.9\ Fe^{+2})$	0.74	0.55	0.63	0.58	0.38
Rb		1	7	38	196
Sr	1072	815	966	542	144
Zr	20	10	93	148	172
Nb	2	6	20	7	16
Y	7	13	24	23	29
Ba	226	635	273	663	502
La	4.5	17.6	12.0	22.5	46.8
Ce	8.2	35.8	28.0	49.9	93.4
Nd	4	23	18	30	40
Sm	1.12	3.60	5.15	5.15	9.04
Eu	0.74	1.94	1.98	1.40	1.11
Tb	0.16	0.56	0.92	0.63	1.20
Yb	0.56	1.01	2.01	2.22	2.58
Lu	0.05	0.16	0.31	0.35	0.41
Hf	0.53	0.51	2.5	4.0	5.6
Th	0.13	0.064	1.8	0.19	27
U	0.066	0.051	1.8	0.20	8

[1]One-pyroxene granulite, metacumulate, from sample locality pk-G-21 (Little Cochise crater). 31°27′N 109°16′W.

[2]Two-pyroxene granulite, metacumulate, sample locality pk-G-21.

[3]Amphibole-bearing, one-pyroxene metacumulate granulite. Sample locality large cinder cone, pk-G-42, 3 mi SW of Fairchild Ranch. 31°30′N 109°11′W.

[4]Two-pyroxene, two-feldspar metadiorite granulite from sample locality pk-G-22. 31°31′N 109°17′W.

[5]Anorthoclasite from sample locality pk-G-22.

Major elements and trace elements Rb, Sr, Zr, Nb, Y, and Ba analyzed by J. G. Fitton and D. James, University of Edinburgh (XRF). Rare-earth elements for all samples and U, Th, and Hf for samples GN22-1, GN42-2 and GN22-5 analyzed by P. Kempton, Open University (INAA). U, Th, and Hf for samples GN21-6 and GN21-4 analyzed by J. R. Budahn, U.S. Geological Survey, Denver.

ene are present along cleavage or exsolution lamellae, associated with spinel inclusions or exsolution (Fig. 6b). Thus, petrographic evidence shows that amphibole replacement was subsequent to spinel exsolution. This relationship establishes that amphibole in a given mantle xenolith need not have formed during crystallization of a single liquid. In this case, sufficient time elapsed for spinel exsolution to occur. The timing of amphibole crystallization in Type IIb amphibole peridotites is less well constrained, but the replacement textures, as well as the disequilibrium demonstrated by the compositional gradients in clinopyroxene observed adjacent to replacement interfaces (above and Kempton et al., 1982), indicate that amphibole and clinopyroxene did not crystallize together.

As a group, LREE enrichment in Type II xenoliths from GVF increases with decreasing Mg number, and with decreasing Cr and Ni contents from Type IIa to Type IIb, suggesting that Type IIb xenoliths were crystallized from slightly more evolved liquids. These and other differences in trace-element and major-element compositions of Type

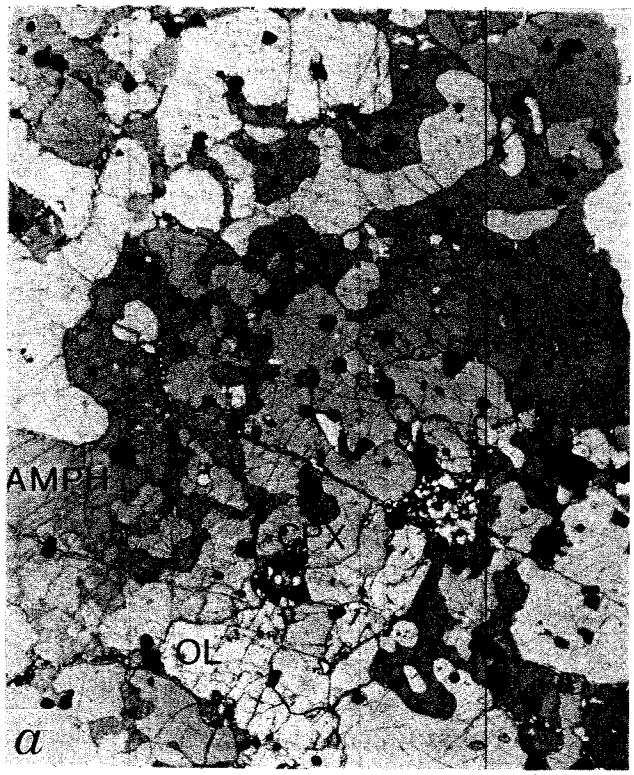

FIGURE 5—**a,** Photomicrograph of sample 90-37-2 from locality pk-G-22. Type IIb amphibole peridotite. Figure shows poikilitic amphibole that replaces clinopyroxenes of varying crystallographic orientations throughout the field of view. Uncrossed polars. Width of field 1.9 cm. **b,** Photomicrograph of sample 22-11 from locality pk-G-22. Type IIb kaersutite peridotite. Poikilitic amphibole in replacement association with clinopyroxene and amphibole. Width of field 1.9 mm. AMPH = amphibole, OL = olivine, CPX = Al-augite clinopyroxene.

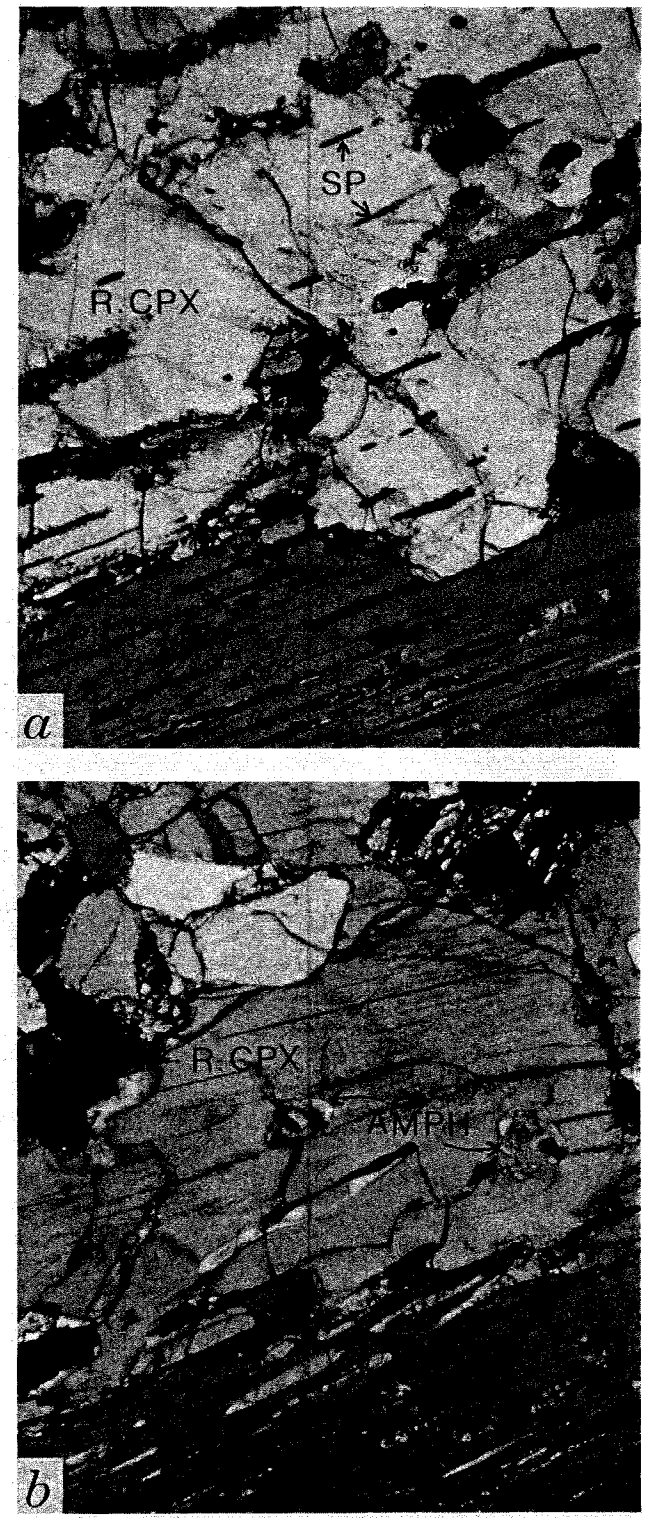

FIGURE 6—Photomicrographs of partially recrystallized Type IIa olivine clinopyroxenite 21-4 from locality pk-G-21. The primary clinopyroxene (P.CPX) contains exsolution lamellae of orthopyroxene and platelets of spinel. The recrystallized clinopyroxene (R.CPX) contains spinel inclusions which are elongate parallel to the original exsolution direction; orthopyroxene exsolution is absent. Amphibole replacement occurs in both recrystallized and unrecrystallized clinopyroxene and is frequently associated with spinel inclusions or exsolution (b). Crossed polars. Width of field 1.9 mm.

II pyroxenes can be attributed to relatively small degrees of crystal fractionation from a range of initial magma compositions like that seen in the GVF primitive lava suite (Kempton, 1984).

All Type II amphiboles, micas, and clinopyroxenes from GVF have radiogenic Nd-isotopic ratios and non-radiogenic Sr-isotopic ratios ($^{87}Sr/^{86}Sr$ = 0.70277–0.70331; $^{143}Nd/^{144}Nd$ = 0.51284–0.51311) which overlap the isotopic values for GVF basalts ($^{87}Sr/^{86}Sr$ = 0.70285–0.70379; $^{143}Nd/^{144}Nd$ = 0.51299–0.513037; Menzies et al., 1984, and Kempton, unpubl. data). The identical isotopic ratios measured in these minerals and the host magmas at Geronimo argue for a close genetic link. Just as major- and trace-element modeling of GVF basalts suggests that fractionation of Type II mineral assemblages can account for much of the compositional variation in these basalts, similar modeling for Type II assemblages suggests that, although not cognate, these xenoliths are probably cumulates from crystallization of basaltic magmas that were similar in composition to their host lavas.

Magma–mantle interactions and mantle-enrichment processes

It is currently accepted that Type I peridotites represent mantle that was variously depleted by extraction of crust, but that many Type I xenoliths have undergone varying degrees of secondary enrichment by reaction with Fe–Ti silicate melts or K-rich hydrous fluids that migrated through the upper mantle (Hawkesworth et al., 1984). Type examples of the former (i.e., mantle–silicate-melt interactions) are found at GVF in the form of composite and modally metasomatized xenoliths.

Structural relationships between Type I and Type II xenoliths at GVF can be summarized using the following four categories.

1. Type I/Type I composite xenoliths have either Cr-diopside, websterite, or clinopyroxenite veins crosscutting spinel lherzolite or harzburgite hosts. Contacts between lherzolite wall rock and pyroxene-rich vein assemblages are usually sharp and planar, and the veins are thin (1–2 cm). Grain size is generally uniform throughout the rock, but some vein pyroxenes may be significantly larger than the host phases; these often exhibit broad exsolution lamellae. In contrast, the host pyroxenes are typically free of exsolution. Type I veins are generally oriented parallel or subparallel to foliation in the host.

2. Type II/Type I composites consist of olivine-rich lherzolite hosts crosscut by more Fe-, Al-, and Ti-rich vein assemblages, usually clinopyroxenite. Contacts are sharp and the orientation of the vein is typically not parallel to foliation in the host. Pyroxene-rich layers which branch, intersect, and locally appear to have been folded or faulted are found at Kilbourne Hole and San Carlos (Irving, 1980). Veins up to 5 cm in width have been observed at GVF, but larger veins (10–15 cm) are reported from other localities (Wilshire and Shervais, 1975; Irving, 1980). Vein minerals average 1 to 2 mm larger than those in the host. Compositional gradients adjacent to the host–vein boundary are inferred from thin sections in which pale-green Cr-diopside and golden-brown Cr-spinel in the lherzolite wall rock become progressively more gray and grayish green toward the vein contact. Such changes indicate progressive substitution of Fe and Al for Cr in the two minerals.

3. Type II/Type I *hydrous* composite xenoliths at GVF consist of the assemblage kaersutite ± phlogopite ± pla-

gioclase ± spinel ± apatite ± sulfides. Amphibole veins and selvages typically transect the plane of mineral layering or foliation at a high angle, indicating that the amphibole veins postdate the anhydrous mineral layering of the peridotite. Amphibole in the host lherzolite part of some GVF Type II/Type I hydrous composites preferentially occurs as single crystals poikilitically enclosing Cr-spinel. Clinopyroxene is completely replaced by amphibole within a 1–2 mm wide zone adjacent to the amphibole selvages. The degree of cpx replacement decreases with distance from the selvage.

4. The composite relationship in which Type II lithologies crosscut a host with transitional Type I–II characteristics (Type II/Type II) consists typically of dark Al-augite clinopyroxene and spinel ± olivine veins which crosscut wehrlite hosts. Olivine is far more abundant in the host than in the vein; it is typically enclosed in sub-poikilitic to poikilitic fashion by aluminous augite in the host. Veins range from anastomosing, millimeter-size veinlets to centimeter-size dikes. Compositionally, the wall-rock phases of this composite type are intermediate between Mg-rich Type I inclusions and Fe-rich Type II xenoliths and, thus, have been interpreted as representing extensively modified Type I lherzolite wall rock (Kempton, 1984; Wilshire, 1984).

Compositional variations in mineral chemistry adjacent to veins in composite xenoliths at GVF are described in detail by Kempton (1987); similar variations for several other localities in the western U.S. are given by Wilshire et al. (1985). The major conclusion drawn from these studies is that silicate- or H_2O-rich fluids which interact with the mantle may alter the major- and trace-element composition of the original mantle and result in modal metasomatism, e.g., in xenoliths bearing secondary hydrous phases or exhibiting composite relationships. Modal metasomatism may be superimposed upon the range of mantle compositions produced by differing degrees of partial melting (Type Ia) and upon the enigmatic LREE-enriched Type Ib inclusions.

Most anhydrous veins in composite samples are attributed to crystallization of basanite magma within conduits as the magmas ascend through the mantle. These interactions may involve re-equilibration of incompatible trace elements, REE and isotopes, or more complete major-element readjustment as in Type II/Type II composite rocks. This process enriches the upper mantle in Al, Ti, Ca, Fe, and incompatible elements by modifying the compositions of primary mineral phases adjacent to veins.

Whole-rock enrichment of incompatible trace elements plus Na and K is greatest where secondary hydrous phases have crystallized in the wall rock. However, compositional variations in primary lherzolite mineral phases adjacent to amphibole selvages and veins are distinct from those adjacent to anhydrous vein types. As a result of reaction with the hydrous fluid represented by the vein minerals, clinopyroxene in the wall rock immediately adjacent to an amphibole selvage is often totally replaced by amphibole. The overall effect of crystallizing amphibole within the peridotite wall rock is to increase the concentrations of Al, Ti, and Fe; but, where present, primary clinopyroxene, orthopyroxene, and spinel show *decreasing* concentrations of Al and Ti toward the selvage. With respect to the vein minerals, concentrations of the compatible elements Mg and Cr are highest in amphibole which has crystallized within the wall rock farthest from the selvage; concentrations of incompatible elements such as Ti and K are constant in the selvage, but *decrease* away from the contact. The latter is significant because it implies that enrichment in incompatible elements may not necessarily increase farther from veins by transport of CO_2–H_2O fluids, as has been suggested by Menzies et al. (1985).

Whole-rock trace-element analyses of host and vein fractions of composite xenoliths indicate that veins typically have significantly higher concentrations of incompatible trace elements than the adjacent host (Irving, 1980; Kempton, unpubl. data). This is essentially a function of the higher modal proportion of incompatible element-rich phases such as clinopyroxene or amphibole in the veins; REE concentrations in clinopyroxene are essentially identical in both host and vein regardless of composite xenolith type (Kempton et al., 1984; Frey and Prinz, 1978). This observation contrasts markedly with the compositional gradients observed for major elements in host–vein composite pairs (Kempton, 1987; Wilshire et al., 1985).

It has been suggested that the enrichment in incompatible trace elements in Type Ib lherzolites is due to infiltration of trace-element-enriched CO_2 fluids exsolved from magmas adjacent to veins like those in composite xenoliths (Menzies et al., 1985). Yet, in addition to their elevated LREE/HREE ratios, Type Ib pyroxenes are known to have substantially lower Al_2O_3 contents and higher MgO and Cr/Al ratios than Type Ia (Kempton, 1987). Aside from the problem of exsolving a CO_2-rich fluid from a silicate melt at mantle pressures and temperatures (Pasteris, 1987), such fluids dissolve only minor quantities of major elements (Eggler, 1987) and would, therefore, be unable to produce a significant change in the Cr/Al or Mg/Fe ratio of the mantle through which they pass. In addition, variations in mineral chemistry across host–vein contacts (Fig. 7) do not result in Type Ib characteristics, clearly demonstrating that veining and modal metasomatism are not responsible for this enigmatic peridotite type. Downes (1987) has suggested a correlation of trace-element enrichment with petrographic characteristics for spinel lherzolites from the Massif Central, but this correlation is as yet undocumented in xenolith suites from the southwestern U.S.

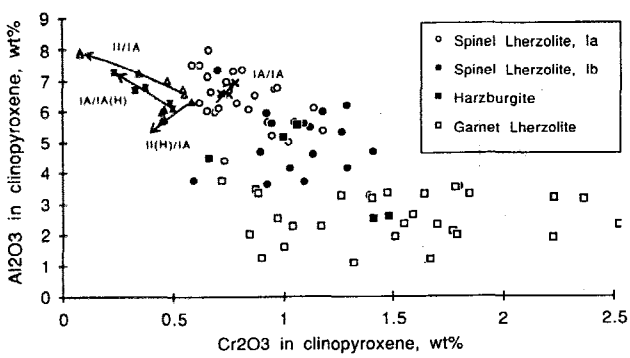

FIGURE 7—Al_2O_3 versus Cr_2O_3 concentrations in clinopyroxenes from Type Ia and Type Ib spinel lherzolites, garnet lherzolites, and harzburgites. Variations in pyroxene composition associated with vein formation are shown by arrows; arrows point from the host toward the vein. Composite samples include Type I/Type I (20-9), Type II (anhydrous)/Type I (20-10), pargasite-bearing Type I/Type I (23b-3) and Type II (hydrous)/Type I (22-16). Spinel lherzolite and harzburgite data from Frey and Green (1974), Frey and Prinz (1978), Jagoutz et al. (1979), Kempton (unpubl. data), Kurat et al. (1980), Press et al. (1986); garnet lherzolite data from MacGregor (1979) and Ehrenberg (1982).

Nature of the lower crust beneath GVF

GVF granulite xenoliths are fine- to medium-grained, foliated or banded, feldspathic, metaigneous gneisses. Mineralogically and compositionally, the xenoliths fall into four groups. The first group contains two-pyroxene granulites that are composed of plagioclase (andesine to labradorite) + clinopyroxene (Mg-augite) + orthopyroxene (hypersthene) + apatite + K-feldspar + ilmenite ± quartz. These typically contain abundant, large primary mineral/melt inclusions in which apatite, K-feldspar, and quartz are the major crystalline phases. The second group is more diverse compositionally and modally, but lacks K-feldspar. As in the first group, some xenoliths in the second group also contain two pyroxenes (Mg-augite and hypersthene), plagioclase (andesine to labradorite), magnetite, and traces of apatite. Others, however, contain only one pyroxene, an aluminous Mg-augite, plus a more calcic plagioclase (labradorite to bytownite) + an aluminous spinel ± olivine ± apatite ± magnetite. Clinopyroxene and spinel compositions in this group are remarkably similar to the Type II ultramafic peridotite minerals described previously. The third group contains members from both of the groups described above, but, in addition, secondary amphibole and rare scapolite are present. Samples in the fourth group are effectively devoid of mafic silicate phases; they consist of K-feldspar (anorthoclase or microcline) ± plagioclase ± quartz ± apatite ± magnetite.

Because none of the GVF granulites contain garnet, pressures of equilibration cannot be directly estimated, but temperature calculations based on two-pyroxene pairs yield values of 890–960°C for the Wells geothermometer and 840–940°C for the Wood–Banno geothermometer. Assuming a geothermal gradient of approximately 30°C/km (Padovani and Carter, 1977a), the Geronimo granulites would have equilibrated between 28 and 32 km depth, roughly the position of the MOHO beneath the Basin and Range.

Compositionally, the granulites are mafic to intermediate rocks (44–73 wt% SiO_2; Mg numbers, 38–79), and as a group demonstrate poor correlation of major- and trace-element concentrations with Mg number. The K-feldspar-bearing inclusions exhibit limited variation in major-element composition and differ from all other GVF granulites in being quartz normative ("Meta-Diorites" Fig. 8A), having higher SiO_2 and alkalis, and lower CaO (Table 3). In contrast, the one- and two-pyroxene, K-feldspar-free granulites range from Ne to Hy normative (Fig. 8A). The one-pyroxene granulites are further distinguished by their higher Mg numbers, similar to the Type II ultramafic cumulate xenoliths occurring at GVF (Table 3). GVF granulites are compositionally unlike their host basalts, but the K-feldspar-bearing inclusions have major- and trace-element compositions which are similar to high-K andesite or diorite. In fact, these granulites have trace-element characteristics not unlike the calc-alkaline volcanic rocks from the Sierra Madre Occidental in eastern Mexico (Gunderson et al., 1986). In trace-element discrimination diagrams (Pearce and Cann, 1973), the K-feldspar-bearing metadiorites have calc-alkaline affinities.

All GVF granulites are LREE enriched relative to HREE, but the K-feldspar-bearing metadiorites are more enriched in total REE (La = 67–74 x chondrites), and have smooth (Eu/Eu* = 0.8–0.9), moderately steep (La/Yb = 5–6) patterns (see Fig. 9a, b). One-pyroxene granulites and K-feldspar-free, two-pyroxene granulites have lower total REE (La = 8–53 x chondrites) with distinct, positive Eu anomalies (Eu/Eu* = 1–2) and more variable LREE enrichment (La/Yb = 3–11), typical of rocks in which plagioclase is a cumulus phase. These rocks are termed "metacumulates" in the figures.

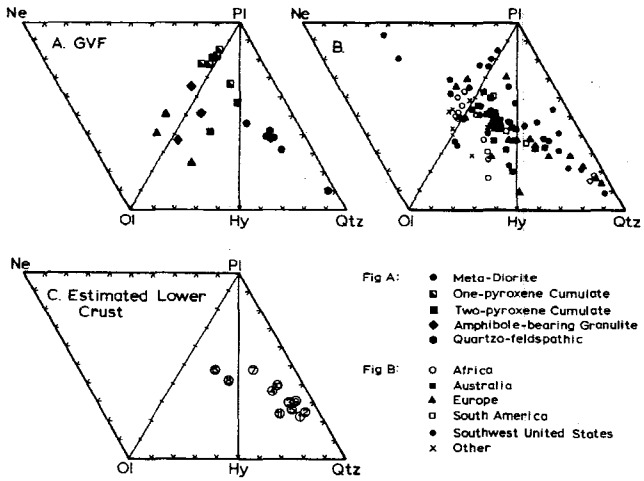

FIGURE 8—**A,** Normative compositions of GVF granulites. See text for discussion. **B,** Normative compositions of representative granulite xenoliths worldwide. Note the predominance of hypersthene-normative compositions. Data are from Padovani and Carter (1977), Selverstone and Stern (1983), Kay and Kay (1981, 1983), Stosch et al. (1986), Leyreloup et al. (1977), Rogers (1977), and Ehrenberg and Griffin (1979). **C,** Estimated crustal compositions recalculated to normative mineralogy: (1) Archean upper crust, (2) Archean middle crust, (3) Archean lower crust, (4) post-Archean mid/lower crust (Weaver and Tarney, 1984), (5) average crust (Weaver and Tarney, 1984), (6) lower crust (Poldervaart, 1955), (7) lower crust, island-arc model (Taylor, 1977), (8) whole crust, average based on crustal xenoliths in kimberlite from the Colorado Plateau (McGetchin and Silver, 1972), (9) lower crust based on Scourian gneisses, Scotland (Sheraton et al., 1973), (10) lower crust, based on mixtures of acidic and basic metamorphic rocks constrained by seismic velocities (Smithson, 1973), (11) lower crust based on metamorphic rocks in the lower 10 km of 40 km section from the Ivrea–Verbano zone (Mehnert, 1975).

All GVF granulites are, not unexpectedly, depleted in the radiogenic-heat-producing elements, Th and U, but only the metacumulate granulites have relatively low K as well (Fig. 9b, Table 3). Metacumulate granulites are enriched in relatively compatible elements such as Sr, while the metadiorites are more enriched in the highly incompatible elements Rb, Ba, REE, Zr, Nb, Hf, and alkalis (Fig. 9a, b). Trace-element concentrations in GVF metadiorites are remarkably similar to average Lewisian tonalite (Weaver and Tarney, 1984) with the notable exception that GVF metadiorites have higher K_2O and heavy REE's and essentially no depletion in Rb. All GVF granulites are distinct from the metasedimentary granulites found at Kilbourne Hole (Fig. 9b).

As a group, Sr-isotopic values for GVF granulites vary from 0.70301 to 0.81853 and $^{143}Nd/^{144}Nd$ varies from 0.513074 to 0.511987 (Kempton, unpubl. data). The two-pyroxene metadiorites, however, exhibit a much smaller overall range of values with lower $^{143}Nd/^{144}Nd$ (0.51219–0.51227) and higher $^{87}Sr/^{86}Sr$ (0.70795–0.71322) while one-pyroxene metacumulates overlap the isotopic values for GVF ultramafic Type II xenoliths and GVF basalts ($^{143}Nd/^{144}Nd$ = 0.51250–0.51282; $^{87}Sr/^{86}Sr$ = 0.70433–0.70961); two-pyroxene cumulates have an intermediate range of values ($^{143}Nd/^{144}Nd$ = 0.51222–0.51257; $^{87}Sr/^{86}Sr$ = 0.70779–0.71243). Most GVF granulites have Rb/Sr ratios which are too low to support the observed $^{87}Sr/^{86}Sr$, suggesting loss of Rb relative to Sr during the metamorphism, with the result

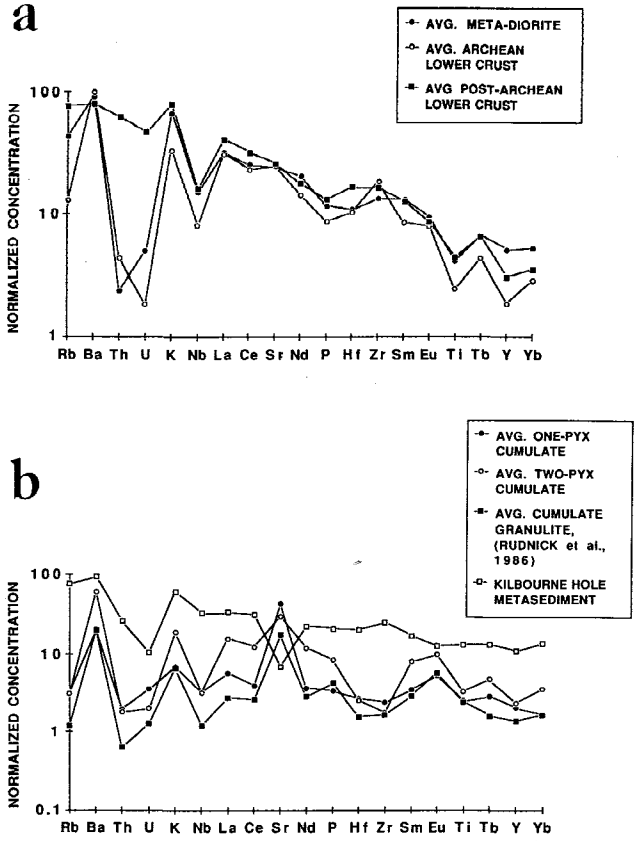

FIGURE 9—**a,** Incompatible trace-element concentrations in average GVF metadiorite compared with average Archean and post-Archean lower crust based on studies of Lewisian tonalite (Weaver and Tarney, 1984). **b,** Incompatible trace-element concentrations in average one- and two-pyroxene GVF metacumulate granulites compared with average metacumulate granulite from Queensland, Australia (Rudnick et al., 1986) and a metasedimentary granulite from Kilbourne Hole (Kempton, unpubl. data). All concentrations normalized to primordial-mantle values of Wood et al. (1981).

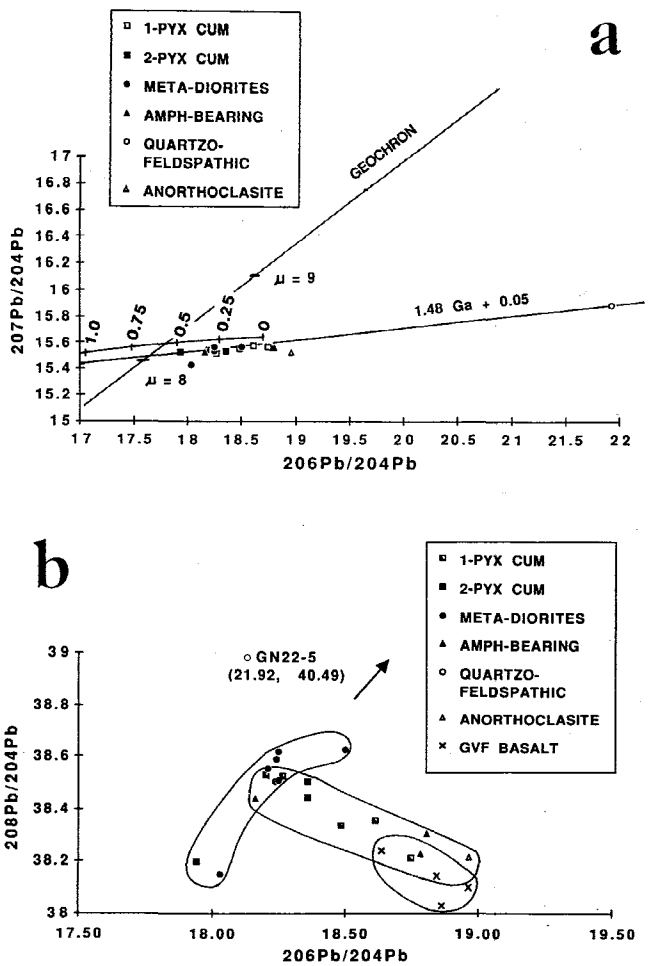

FIGURE 10—**a,** $^{207}Pb/^{204}Pb$ versus $^{206}Pb/^{204}Pb$ for GVF granulites. Regression of the data yields an age of 1.48 Ga±0.05. **b,** $^{208}Pb/^{204}Pb$ versus $^{206}Pb/^{204}Pb$. GVF basalt data are from Everson (1979) and Kempton (unpubl.).

that the Sr-isotopic relationships no longer record the age of the xenoliths. Nd and the other REE elements, on the other hand, are known to be less mobile during crustal processes. Calculated Nd model ages for metadiorites range from 1.1 to 1.4 Ga. Metacumulate granulites, however, exhibit a wide range of calculated ages and generally have low Sm/Nd ratios, inconsistent with their radiogenic $^{143}Nd/^{144}Nd$. This probably reflects relatively recent accumulation of low Sm/Nd clinopyroxene from a magma with a relatively high $^{143}Nd/^{144}Nd$, such that, again for these xenoliths, the isotopic values have no age significance.

Lead isotopes for GVF granulites exhibit the following range in values: $^{206}Pb/^{204}Pb$ = 18.198–21.921; $^{207}Pb/^{204}Pb$ = 15.522–15.887; $^{208}Pb/^{204}Pb$ = 38.152–40.488 and on a $^{207}Pb/^{204}Pb$ vs. $^{206}Pb/^{204}Pb$ diagram the GVF xenolith data exhibit a linear distribution that yields an age of approximately 1.5 Ga, i.e., similar to the range of Nd model ages for metadiorites (Fig. 10a). The GVF metacumulates, however, display a negative slope on a plot of $^{208}Pb/^{204}Pb$ vs. $^{206}Pb/^{204}Pb$ which trends away from the positive slope shown by the metadiorites (Fig. 10b). These data are interpreted as evidence that GVF metacumulate granulites are the crystallization products of Cenozoic alkalic magmas that were similar to their host basalts; isotopically, these parent magmas were contaminated by mixing with preexisting lower to middle crustal rocks such as the GVF metadiorites or early Proterozoic (1.4–1.6 Ga) granitic rocks like those exposed to the west and north. Similar mixing relationships are observed on isotopic diagrams of Pb vs. Sr and Pb vs. Nd.

In summary, chemical and isotopic analyses of granulite xenoliths from GVF indicate that the various granulite groups are not comagmtic. These data also document that the lower crust in this region is heterogeneous in composition and age. Two-pyroxene, two-feldspar granulites are intermediate-composition, mid-Proterozoic (~1.3–1.4 Ga) metadiorites that are depleted in Th, U, Rb, Nb, and Ti. K-feldspar-free granulites are younger and have more variable major- and trace-element compositions, but are distinctly more mafic and show enrichments in Sr, Ba, and Eu consistent with the accumulation of plagioclase. Similarities in mineral chemistry between metacumulus granulites and Type II ultramafic xenoliths suggest similar parent liquid compositions, although probably shallower depths of crystallization for the metacumulate granulites. The isotopic compositions of metacumulate granulites reflect mixing of Cenozoic mafic magmas with older lower crust, documenting a recent event of underplating of mafic material to the subcontinental lithosphere. As a whole, the GVF granulite suite suggests that the present lower crust is more mafic than most recent estimates of average lower crustal composition (Fig. 8).

Synthesis

The petrologic data presented in the previous sections can be summarized in a hypothetical cross section through the crust and upper mantle beneath GVF (Fig. 11). The strong enrichment in LREE relative to HREE and small range of HREE values in GVF basalts suggests that they were generated in a source where garnet was a residual phase. In addition, GVF basalts and ultramafic xenoliths show broadly OIB-like Nd- and Sr-isotopic signatures and indicate a time-integrated depletion in incompatible trace elements (Menzies et al., 1985). These data suggest that upwelling mantle material may have risen from the asthenosphere to penetrate the lithosphere. Although no petrofabric evidence for such intrusion of asthenosphere into lithosphere is observed in GVF ultramafic xenoliths, it is nonetheless consistent with the interpretation of upwelling mantle beneath the extensional regime of the Basin and Range.

Silicate melts generated in garnet lherzolite asthenosphere are not in equilibrium with overlying lithospheric mantle, and given sufficient time they must react with the mantle through which they ascend. Thus, intrusion of such silicate melts can enrich the mantle in magmaphile elements; first, and probably more importantly, by whole-scale addition of material crystallized as veins and dikes, but also by metasomatic interaction between these veins and the mantle itself. The nature and extent of this enrichment is dependent on a number of factors such as melt composition, volume of melt, magma ascent rate, etc. The variety of mafic/ultramafic layers, dikes and veins seen in the composite xenoliths attests to the complex history and multiplicity of events in the history in the sub-GVF mantle.

Unfortunately, the timing and depth relationships among the different vein assemblages cannot be established directly on the basis of GVF xenolith data alone. The lack of pressure estimates based on well-calibrated experimental data for most of the mantle xenoliths has prevented detailed evaluation of the P–T relationships among the various xenolith types, including composite relationships. However, field studies of peridotite massifs (Sinigoi et al., 1983; Wilshire and Pike, 1975) document that Type I websterite or clinopyroxenite dikes (Type I) are the earliest dikes to form and are followed by Type II mineral assemblages.

Partial melts are believed to first accumulate in horizontal layers. Then, as the critical melting threshold is exceeded, liquids are able to filter slowly toward lower-pressure zones. In so doing, these liquids fractionate, initially in-situ, via crystallization of Type I websterite or clinopyroxenite dikes. Continuous exchange with mantle wall rock over time results in decreasing SiO_2, rapid enrichments in Al_2O_3, and mild increases in FeO and CaO in the melt. Crystallization of these modified liquids produces transitional and Type II Al-augite dikes. Therefore, we suggest in Fig. 11 that Type I/Type I composite relationships occur where the melts are near their source of origin and where the volume of melt is most likely small. Here, melt compositions are probably not far from equilibrium with the surrounding peridotite and the compositions of minerals crystallized are similar to the wall-rock mineral phases. Farther from the garnet–lherzolite source in the overlying depleted, undisturbed lithosphere, however, these trace-element enriched melts are decidedly out of equilibrium and crystallization of Type II aluminous clinopyroxenite veins occurs. Metasomatic exchange may occur between the wall rock and the veins, involving modification or re-equilibration of incompatible trace elements, REE and isotopes (Type II/Type I), or more complete major-element adjustments as in Type II/Type II composites.

Composite ultramafic xenoliths record relatively small-scale intrusive events in the upper mantle, but decreasing

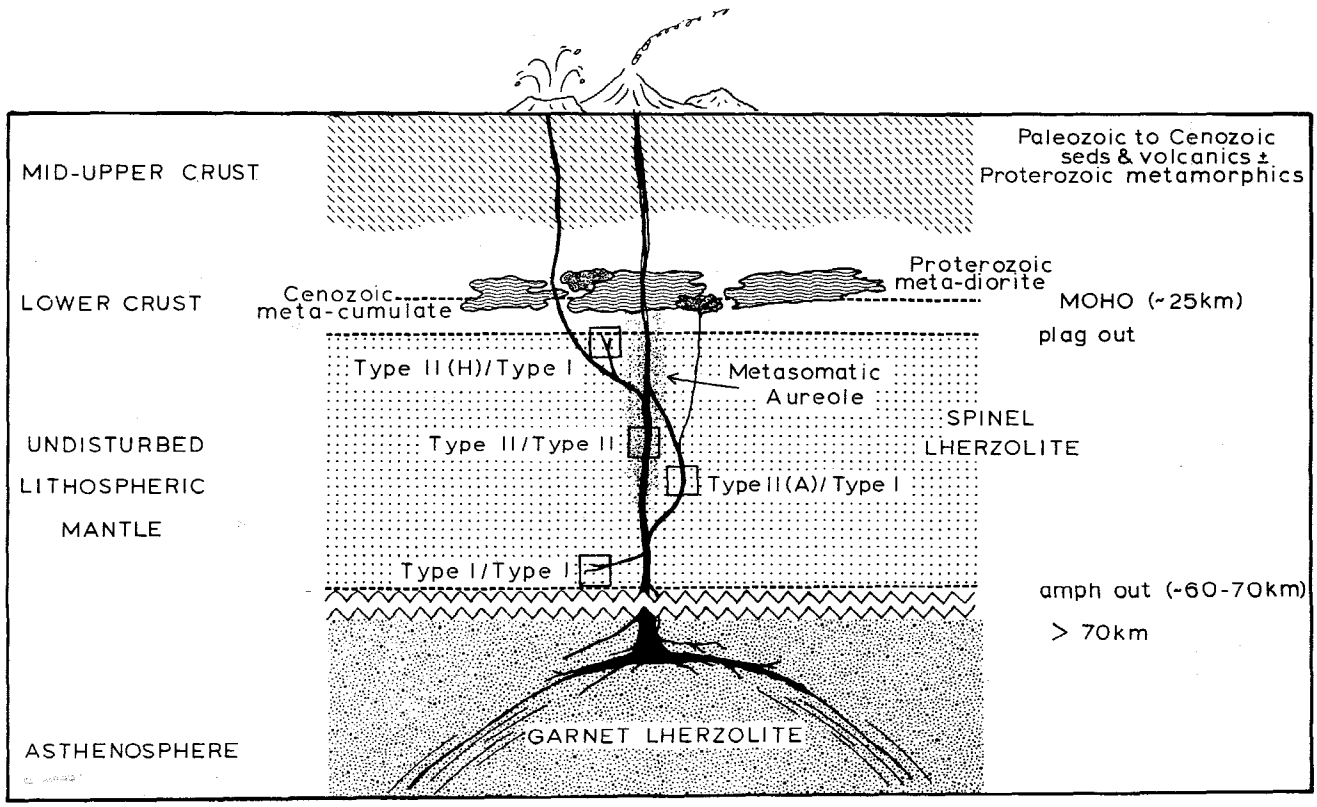

FIGURE 11—Schematic cross section of the crust and upper mantle beneath the Geronimo volcanic field. See text for discussion.

density contrasts may cause much larger volumes of basic–ultrabasic magma to stagnate in the lower crust at, or near, the crust–mantle boundary. Recent seismic-reflection studies have documented the existence of prominent, short, subhorizontal reflectors in the lower continental crust beneath the extensional regime of the Basin and Range (Klemperer et al., 1986; Caruso, oral comm. 1987). The reflectors are well developed and the boundary appears to coincide with the MOHO. Based on these geophysical data, the MOHO beneath the Basin and Range has been interpreted as a young feature, continuous beneath both stable cratonic and allochthonous areas, and is dominated by the intrusion of mafic magmas (Allmendinger et al., 1986; Klemperer et al., 1986). Geochemical data for GVF granulites are consistent with this interpretation and indicate that recent mafic magmas have crystallized in the lower crust, probably near the crust/mantle boundary, and have intruded older Proterozoic granulitic lower crust. The isotopic compositions of GVF metacumulate granulites record this intrusion and mixing of Cenozoic mafic magmas with older (1.3–1.5 Ga) lower crust, documenting a recent event of underplating of mafic material to the subcontinental lithosphere.

Road log

Mileage

0.0 Begin trip at Shell service station in Rodeo, New Mexico. Drive south on US-80 down axis of San Simon Valley. **11.4**

11.4 Apache, New Mexico. **9.2**

20.6 **STOP 1A. Geologic overview of the Geronimo volcanic field.** At intersection of US-80 and unpaved road to Rucker Canyon, turn right (northeast) and stop immediately after crossing cattleguard. The purpose of this stop is to point out some of the general structural and petrologic aspects of the Geronimo volcanic field (GVF). The San Bernardino graben, in which the GVF is located, is oriented roughly north–south and is approximately 10 km wide in its southern extension, broadening northward to about 15 km at GVF. The San Simon graben to the north is only about 5–7 km wide at its southern end and trends northeast where it intersects GVF, but continues northward in an arcuate shape, ending in a more northwesterly orientation north of the Chiricahua Mountains where it broadens to roughly 30 km (see Fig. 1).

Looking to the northwest, the high mountains (12:00 to about 2:00) are the Oligocene–Miocene rhyolitic volcanic rocks of the Chiricahua Mountains. The lower peaks of Limestone Mountain (12:00) are mostly Paleozoic and early Mesozoic sedimentary and volcanic rocks that have been thrust to the northeast over Cretaceous rocks along northwest–southeast-oriented thrust faults of Late Cretaceous–early Tertiary age (Drewes, 1981).

Physiographic distributions of lavas of different ages at GVF are largely distinct. Lavas exposed in Mulberry Canyon in the Pedregosa Mountains (11:00) have an age range of 3.0–3.2 Ma (Kempton et al., 1987), and two basalt flows about 1 mi farther south give similar ages of 3.3 Ma (Lynch, 1978). The youngest known flows in the field are from Mangus maar (3:00, due north) dated at 0.26 Ma (Kempton, 1987) and from a flow north of Cinder Hill in the southernmost portion of the GVF (0.27 Ma; Lynch, 1978). The oldest dated valley lava is 3.6 Ma from Paramore maar; the basalts we will see at Stop 1B have been dated at 1.5 Ma. Basalts exposed in the Peloncillo Mountains on the eastern side of the valley are generally older, ranging from 4.7 to 9.2 Ma (Kempton et al., 1987). These age variations are consistent with the interpretation, based on gravity data, that the western part of the basin has been faulted downward relative to eastern part along buried faults that parallel the margins of the valley (Lynch, 1978).

The basalts erupted in the valley occur as cinder cones, maars, and associated flows. More than 125 cinder cones and eruptive vents of agglutinated spatter, bombs, and ash are observed in the San Bernardino Valley at GVF; at least 25% of these are strombolian cones 1–2 km in diameter. Most rise 70–100 m above the valley floor, but some of the youngest and least eroded reach 200 m of relief. Many of the cinder cones overlie aprons of pyroclastic-surge deposits and some vents erupted only phreatomagmatic tuffs, forming extensive tuff rings and large maar craters. Lava flows generally issue from the sides of breached cones and cover areas of only a few square kilometers; a few reach lengths of 5–7 km. In contrast, the flank lavas occur as erosional remnants or plateau-capping flows. Vents for most of these flows have largely been eroded and eruptive style is unknown, but there is no reason to suspect that eruptive style for these lavas differed from that of the strombolian activity exemplified by valley basalts.

After discussion, proceed northeast toward the southern Chiricahua Mountains along Rucker Canyon Road. Cones of valley basanites are on left after 1–2 mi. The smaller, dissected cone contains abundant lherzolite xenoliths. Pass Krentz Ranch Headquarters. The Krentz cone and flow complex lies directly north of ranch buildings. Road turns due north and then crosses Tex Creek after 1 mi. Basanite lava flow overlies gravels east of road. **6.7**

27.3 **STOP 1B. The Krentz flow valley basanite.** Pass through fence and gate at National Forest boundary. Park in campsite area on left immediately past gate. Walk back through gate and cross the road to large talus blocks of Krentz basanite.

The purpose of this stop is to view a typical valley lava flow and to discuss some of the geochemical evidence for the temporal evolution of the Geronimo volcanic field. The Krentz basanite at Stop 1B is aphyric, with a very fine-grained cryptocrystalline groundmass. Xenocrysts of anorthoclase, plagioclase, augite, spinel, and sparse olivine occur along with abundant small gabbroic xenoliths. Exposures of the flow form massive, columnar-jointed cliffs; at several locations the lower contact between the flow and the underlying rubble and fanglomerate is well exposed. Several nested cinder cones cap the flow at its northern end.

Return to highway. **6.7**

34.0 Highway 80. Turn right (southwest) onto pavement. Pass milepost 390. **6.5**

40.5 Turn left onto road with locked gate. **Do not attempt to enter fenced area unless prior arrangements have been made with ranch owners.** Proceed through gate and drive east toward cones. **0.9**

41.4 Unlocked gate north of small cone. For the next mile, the road traverses the north flank of a pyroclastic deposit (tuff ring) erupted from a partly covered vent that forms a bench to the south of a pair of coalesced strombolian cones. These younger cones occupy and cover the south rim of the tuff ring. Two areas of well-exposed resistant tuff can be seen from the road. **1.2**

42.6 **STOP 2A. Physical volcanology of the Geronimo volcanic field and an introduction to the GVF xenolith suite.** Turn right on the poorly marked track leading to water tank (0.4 mi distance from road to tank is not included in mileage log). Use caution in driving vans or cars all the way to the water tank.

This locality, pk-G-22, is of interest for the variety of pyroclastic deposits and the varied xenolith/xenocryst suite. Included in the xenolith/xenocryst suite are xenocrysts of anorthoclase, augite, and olivine, typical Type I spinel lherzolite, and Type II aluminous-augite clinopyroxenites. Crustal granulites are predominantly two-pyroxene, two-feldspar metadiorites with Nd model ages of 1.1–1.4 Ga. Fragments of kaersutite crystals and kaersutite-rich xenoliths are particularly abundant (more so than at any other Geronimo locality) and several xenoliths with veins of phlogopite ± pargasite ± plagioclase have been found here (phlogopite has not been observed at any other locality).

The pyroclastic deposits seen at this locality include three distinctive units which apparently represent a progression in eruption character from phreatomagmatic to strombolian. The lower part of the north-facing slope, up to the elevation of the water tank, is underlain by weakly bedded, well-indurated tuffs rich in small angular lithic fragments. The tuffs dip gently to steeply away from the vent. These early deposits are interpreted as transitional in character between pyroclastic surge deposits and typical strombolian deposits, and are thought to have been deposited as a tuff ring during a phreatically dominated vent-clearing phase of the eruption. These deposits contain a magmatic component as well as the same xenolith/xenocryst assemblage that is found in younger phases of the eruption.

These early deposits are overlain by an inward-dipping unit which is fundamentally similar in character. Large bombs of basanite containing high concentrations of xenoliths and xenocrysts are much more abundant than below. In the western outcrop the angular discontinuity between the two units is very marked and well exposed. Overlying the deposit that forms the topographic rim of the tuff ring are spatter, bomb, and ash deposits typical of the strombolian cones of the Geronimo field. The progression from early bedded, lithic-rich deposits suggestive of a highly explosive origin (possibly surge deposits related to early phreatic activity) to strombolian activity and lava flows is typical of these cones.

Return to main dirt road.

42.6 Turn right on road. Go less than 100 m to intersection of several roads. Turn right (south) onto road paralleling dry gully. This road climbs to a broad divide on a lava flow among several cones. A series of water tanks marks the location of the road. Approximately 2.4 mi from last turnoff the road crosses another gully (proceed with caution). **3.7**

46.3 **STOP 2B. More xenoliths and evidence for mantle-enrichment processes.** Park vehicles in depression west of Cochise maar and Little Cochise crater (see Fig. 12). This locality encompasses several xenolith-bearing cones.

Cochise crater (1.3 km in diameter) is a 50 m deep volcanic depression which has had a complex history. Units exposed on the walls include flows and spatter beds that are both older and younger than the crater. Poorly bedded, lithic-rich deposits resembling the lower unit at the previous locality are well exposed in a small cliff outcrop northeast of Little Cochise crater. This highly indurated zone grades upward into a less indurated tuff with abundant large magmatic bombs. Several xenolith-bearing cones, including the prominent Little Cochise crater (west rim of Cochise crater), postdate the main tuff ring. Bombs in the tuff ring deposit contain minor xenolithic and xenocrystic material. The prominent cone west-southwest of Little Cochise crater contains abundant xenoliths and is breached on its south side by a xenolith-rich lava.

Although amphibole peridotites seen at the previous stop are far less abundant, this locality is interesting for the variety of mafic and ultramafic rocks. Type IIa and IIb aluminous augite-rich xenoliths comprise a high proportion of the population, and composite xenoliths with veins and dikes of Type II material crosscutting Type I spinel lherzolite and Type II wehrlite are relatively common. Both Type Ia and Type Ib lherzolites have been found. Granulite xenoliths are predominantly one- and two-pyroxene metacumulates, although rare metadiorites occur as well.

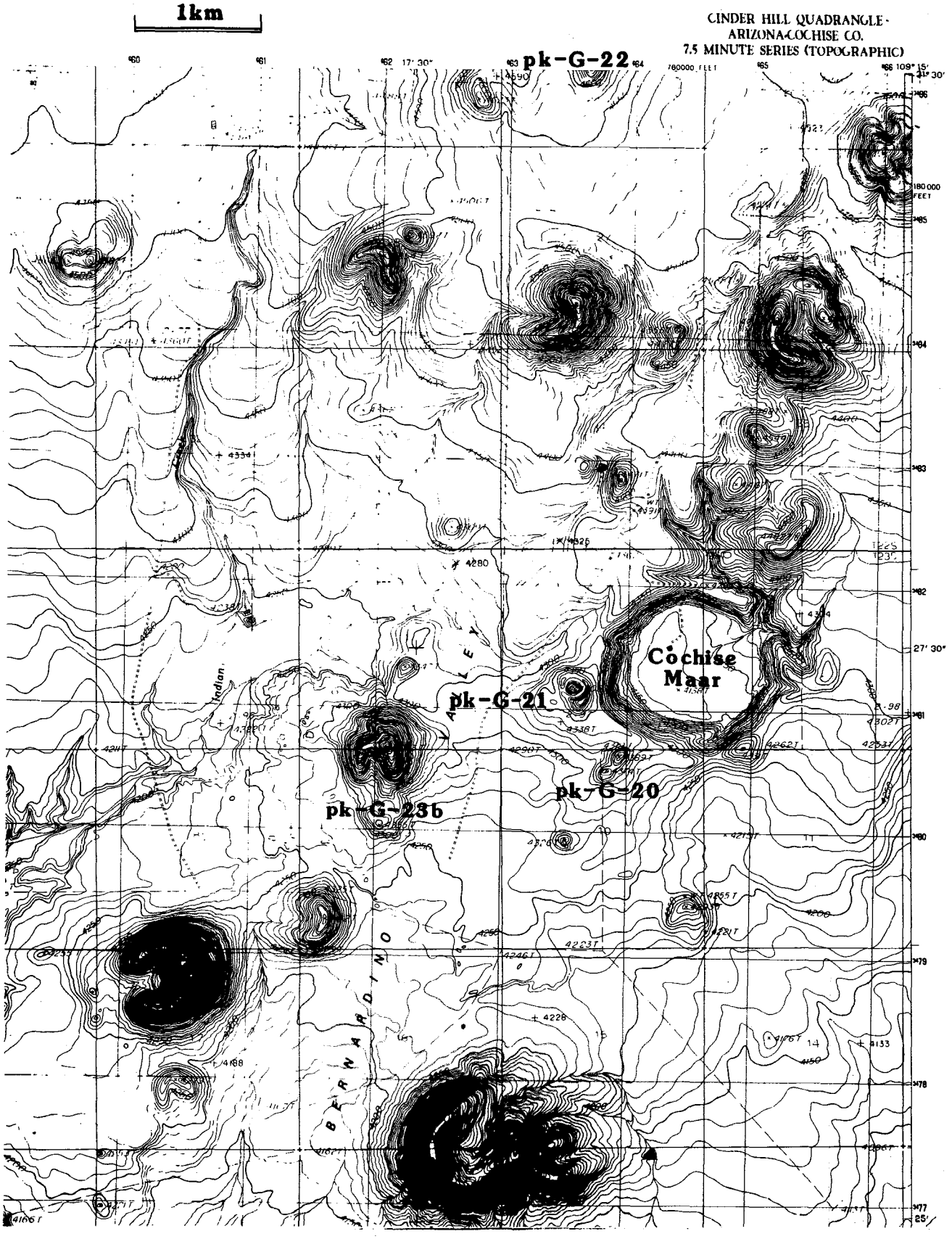

FIGURE 12—Topographic map for area surrounding Stop 2B, including sample localities pk-G-20 through pk-G-23b and Cochise maar.